AN ABSTRACT OF THE DISSERTATION OF

Ean A. Amon for the degree of Doctor of Philosophy in
Electrical and Computer Engineering presented on November 24, 2010.

Title: Development of Two-Variable Maximum Power Point Tracking Control for Ocean Wave Energy Converters Utilizing a Power Analysis and Data Acquisition System.

Abstract approved: _____
Ted K.A. Brekken

Ocean wave energy shows great potential as a developing form of renewable energy. However, challenges arise in maturing this technology to achieve cost-effective energy conversion. Development and testing of wave energy converters can be problematic due to the harsh environment in which they are operated. To promote development of this technology, a platform is needed for comprehensive testing of these devices in this harsh environment. This will allow the determination of optimal topologies and control of wave energy converters for maximum power extraction.

This work evaluates maximum power point tracking control in wave energy converters and presents two-variable maximum power point tracking control algorithms. A robust testing platform is developed for evaluating wave energy converters in the ocean environment. This testing platform is utilized in obtaining experimental data used in validating simulation results of the investigated control approaches.

Development of Two-Variable Maximum Power Point Tracking Control for Ocean Wave Energy Converters Utilizing a Power Analysis and Data Acquisition System

by
Ean A. Amon

A DISSERTATION

Submitted to

Oregon State University

in partial fulfillment of
the requirements for the
degree of

Doctor of Philosophy

Presented November 24, 2010
Commencement June 2011

Doctor of Philosophy dissertation of Ean A. Amon
presented on November 24, 2010.

APPROVED:

Major Professor, representing Electrical and Computer Engineering

---

Director of the School of Electrical Engineering and Computer Science

---

Dean of the Graduate School

I understand that my dissertation will become part of the permanent collections of Oregon State University libraries. My signature below authorizes release of my dissertation to any reader upon request.

Ean A. Amon, Author

ACKNOWLEDGEMENTS

I would like to give much thanks to my major professors, Dr. Ted Brekken and Dr. Annette von Jouanne for their guidance, support, and enthusiasm throughout my years as part of the Energy Systems Group at Oregon State University. Also, special thanks goes to my committee members: Dr. Robert Paasch, Dr. Alex Yokochi and Dr. Joe Zaworski.

To all members of the Energy Systems group, both past and present, I give very sincere thanks for their support of my research and continuing friendship. I enjoyed every minute of working with you and wish you all the best. I especially would like to thank Aaron, Al, Charles, Dave, Doug, Joe, Ken, and Pete for all of the good times, both in and out of the lab.

Thanks to the Bonneville Power Administration, US Navy, Columbia Power Technologies, and the State of Oregon for supporting this research.

Finally, my greatest thanks goes to my parents, Dan and Nancy, and my sister, Melissa, for their ongoing love and encouragement; I could not have done this without you.

TABLE OF CONTENTS

Page

1. INTRODUCTION 1
   1.1 Background 1
   1.2 Characterizing Wave Energy Devices 1
   1.3 Maximizing Power Extraction in Wave Energy Devices 2
2. POWER ANALYSIS AND DATA ACQUISITION SYSTEM 3
   2.1 Introduction 3
   2.2 Design Specification 3
      2.2.1 Electrical Loading System 3
      2.2.2 Data Acquisition System 4
   2.3 Converter Topologies 4
   2.4 System Design and Components 6
      2.4.1 Power Electronics 9
      2.4.2 Opal-RT PC/104 Rapid Prototyper 9
      2.4.3 System Protection 10
      2.4.4 System Input and Output Inductance 11
      2.4.5 Voltage and Current Transducers 11
      2.4.6 Inrush Current Limitation 12
      2.4.7 System Enclosure 12
   2.5 Ocean Testing of a Wave Energy Converter 12
      2.5.1 Passive Rectifier Operation 13
      2.5.2 Hardware Results 14
3. EXPERIMENTAL SETUP 18
   3.1 Experimental Setup Overview 18
   3.2 Wave Energy Linear Test Bed 18
   3.3 Position vs. Time Profile 20
4. SYSTEM SIMULATION 22
   4.1 Simulation Overview 22

TABLE OF CONTENTS (Continued)

Page

4.2 LTB / L10 Simulation Model....23
4.3 Power Analysis and Data Acquisition System Model....26
4.3.1 Passive Rectifier Model....26
4.3.2 Active Rectifier Average Model....28
4.4 Model Tuning and Verification....29
4.4.1 L10 Back-EMF Tuning....30
4.4.2 L10 Phase Resistance and Inductance Tuning....34
4.4.3 PADA Model Verification....34
5. SINGLE-VARIABLE MAXIMUM POWER POINT TRACKING....36
5.1 Introduction....36
5.2 Control Implementation....36
5.2.1 Degrees of Freedom....37
5.2.2 Control Implementation Objectives....38
5.3 Passive Rectifier Operation....38
5.3.1 Experimental Results....39
5.3.2 Simulation Results....40
5.3.3 Experimental and Simulation Results Comparison....41
5.4 Active Rectifier Operation....44
5.4.1 Experimental Results....44
5.4.2 Simulation Results....45
5.4.3 Experimental and Simulation Results Comparison....46
5.5 Observations....48
5.5.1 Passive vs. Active Rectifier Mode....48
5.5.2 MPPT Time Constant, τ_mppt....48
6. TWO-VARIABLE MAXIMUM POWER POINT TRACKING....51
6.1 Introduction....51
6.2 Control Implementation....51

TABLE OF CONTENTS (Continued)

Page

6.2.1 Degrees of Freedom 52
6.2.2 Control Implementation Objectives 52
6.3 Two-Variable Independent MPPT 53
6.3.1 Simulation Results 55
6.3.2 Experimental Results 59
6.4 Two-Dimensional Four-Step MPPT 60
6.4.1 Simulation Results 61
6.4.2 Experimental Results 65
6.5 Two-Dimensional Two-Step MPPT 67
6.5.1 Simulation Results 68
6.5.2 Experimental Results 71
6.6 Two-Dimensional Two-Step Radial MPPT 72
6.6.1 Simulation Results 74
6.6.2 Experimental Results 76
6.7 Observations 77
6.7.1 Comparison of Two-Variable Control Algorithms 77
6.7.2 MPPT Control Rate, *cRate* 79
7. CONCLUSION 84
7.1 Conclusions 84
7.1.1 Power Analysis and Data Acquisition System 84
7.1.2 Maximum Power Point Tracking for Wave Energy Converters 84
7.2 Recommendations for Future Work 85
BIBLIOGRAPHY 87
APPENDICES 91
A. Two-Dimensional Four-Step MPPT, Level-2 M-File S-Function Code 92

TABLE OF CONTENTS (Continued)

Page

B. Two-Dimensional Two-Step MPPT,
Level-2 M-File S-Function Code 96

C. Two-Dimensional Two-Step Radial MPPT,
Level-2 M-File S-Function Code 100

LIST OF FIGURES

Figure Page

2.1. Three-phase, four-quadrant converter. 5

2.2. Single-phase ac or dc loading with a three-phase converter. 5

2.3. Active three-phase converter with a controlled resistive load. 6

2.4. PADA system schematic. 7

2.5. PADA system with resistive load bank during ocean testing. 7

2.6. PADA system internal components. 8

2.7. PADA system internal components. 8

2.8. Screenshot from host computer; upper plot showing three-phase and dc bus voltage, middle plot showing three-phase current, and lower plot showing instantaneous and filtered input power. 10

2.9. Recorded waveforms with a fixed duty ratio of 0.4. 15

2.10. Recorded waveforms with a 10 amp current reference. 16

2.11. Recorded power waveform with a 6 amp current reference. 17

3.1. L10 active components mounted in the Wave Energy Linear Test Bed at Oregon State University. 19

3.2. Fifteen-minute buoy position profile. 20

3.3. Short-duration example of buoy position profile. 21

4.1. Full system simulation model in MATLAB Simulink. 22

4.2. Contents of PMLTG_Coils block. 24

4.3. Contents of one coil block in PMLTG_Coils. 25

4.4. Contents of the phase blocks. 25

4.5. Passive rectifier PADA model. 27

4.6. Passive rectifier simplified diode model. 27

4.7. Active rectifier PADA model. 29

4.8. Phase voltage waveform mismatch. 31

4.9. Commanded LTB position and commanded force scaled by the LTB carriage spring constant. 32

LIST OF FIGURES (Continued)

Figure Page

4.10. Compensated position for simulation shown with original position for experimental testing recorded by both the PADA and LTB. 33

4.11. Experimental and simulation phase voltage waveforms using the compensated position profile in simulation. 33

4.12. Phase voltage and current comparison for experimental and simulation passive rectifier results. 35

4.13. Phase voltage and current comparison for experimental and simulation active rectifier results. 35

5.1. MATLAB Simulink model of the single-variable MPPT algorithm. 37

5.2. Average power produced for fixed duty ratio sweep for experimental and simulation. 39

5.3. Experimental passive rectifier results: normalized average power as a function of τ_mppt and *cStep*. 40

5.4. Simulated passive rectifier results: normalized average power as a function of τ_mppt and *cStep*. 41

5.5. Experimental and simulation normalized average power as a function of τ_mppt and *cStep* with a buck converter duty ratio step size of 0.1. 42

5.6. Experimental and simulation normalized average power as a function of τ_mppt and *cStep* with a buck converter duty ratio step size of 0.5. 42

5.7. Experimental and simulation normalized average power as a function of τ_mppt and *cStep* with a buck converter duty ratio step size of 0.01. 43

5.8. Experimental and simulation normalized average power as a function of τ_mppt and *cStep* with a buck converter duty ratio step size of 0.001. 43

5.9. Decision differences in experimental and simulation results; *cStep* of 0.1 and τ_mppt of 10 seconds. 44

5.10. Experimental active rectifier results: normalized average power as a function of τ_mppt and *cStep*. 45

5.11. Simulated active rectifier results: normalized average power as a function of τ_mppt and *cStep*. 46

5.12. Experimental and simulation normalized average power as a function of τ_mppt and *cStep* with 1 ohm step size. 47

LIST OF FIGURES (Continued)

Figure Page

5.13. Experimental and simulation normalized average power as a function of τ_mppt and *cStep* with 0.1 ohm step size. 47

5.14. Excessive dithering of the buck converter duty ratio. 50

6.1. MATLAB Simulink model of two-variable independent control. 54

6.2. Implementation of complex load impedance command. 54

6.3. Control signals showing timing offset in MPPT loops. 55

6.4. Two-variable independent MPPT simulation results: normalized average power as a function of τ_mppt and *cStep*. 56

6.5. Two-variable independent MPPT simulation results: normalized average power as a function *cRate*. 57

6.6. Two-variable independent MPPT simulation results: normalized average power as a function *cRate* with Butterworth least-squares fit. 58

6.7. Two-variable independent MPPT experimental results: normalized average power as a function of *cRate* with simulation Butterworth least-squares fit. 60

6.8. Operation of the two-dimensional four-step MPPT algorithm. 61

6.9. Two-dimensional four-step MPPT simulation results: normalized average power as a function of τ_mppt and *cStep*. 63

6.10. Control signals for two-dimensional four-step MPPT; *cStep* of 0.01 and τ_mppt of 0.01. 63

6.11. Two-dimensional four-step MPPT simulation results: normalized average power as a function *cRate* with Butterworth least-squares fit. 65

6.12. Two-dimensional four-step MPPT experimental results: normalized average power as a function of *cRate* with simulation Butterworth least-squares fit. 66

6.13. Two-dimensional four-step MPPT experimental and simulation results for *cStep* of 0.1: normalized average power as a function of *cRate* with simulation Butterworth least-squares fit. 66

6.14. Operation of the two-dimensional two-step MPPT algorithm. 68

6.15. Two-dimensional two-step MPPT simulation results: normalized average power as a function of τ_mppt and *cStep*. 69

6.16. Two-dimensional two-step MPPT simulation results: normalized average power as a function *cRate* with Butterworth least-squares fit. 70

LIST OF FIGURES (Continued)

Figure Page

6.17. Two-dimensional two-step MPPT experimental results: normalized average power as a function of *cRate* with simulation Butterworth least-squares fit. 71

6.18. Two-dimensional two-step MPPT experimental and simulation results for *cStep* of 0.01: normalized average power as a function of *cRate* with simulation Butterworth least-squares fit. 72

6.19. Operation of the two-dimensional two-step MPPT algorithm. 73

6.20. Two-dimensional two-step radial MPPT simulation results: normalized average power as a function of τ_mppt and *cStep*. 74

6.21. Two-dimensional two-step radial MPPT simulation results: normalized average power as a function *cRate* with Butterworth least-squares fit. 75

6.22. Two-dimensional two-step radial MPPT experimental results: normalized average power as a function of *cRate* with simulation Butterworth least-squares fit. 76

6.23. Two-dimensional two-step radial MPPT experimental and simulation results for *cStep* of 0.01: normalized average power as a function of *cRate* with simulation Butterworth least-squares fit. 77

6.24. Comparison of the least-squares Butterworth fit from simulation for each control algorithm with corner frequencies indicated. 79

6.25. Two-variable independent MPPT simulation results with non-optimal initial conditions. 80

6.26. Two-dimensional four-step MPPT simulation results with non-optimal initial conditions. 81

6.27. Two-dimensional two-step MPPT simulation results with non-optimal initial conditions. 81

6.28. Two-dimensional two-step radial MPPT simulation results with non-optimal initial conditions. 82

6.29. Comparison of the least-squares Butterworth fit from simulation for each control algorithm, plotted by τ_mppt for *cStep* of 0.1. 83

Development of Two-Variable Maximum Power Point Tracking Control for Ocean Wave Energy Converters Utilizing a Power Analysis and Data Acquisition System

1. INTRODUCTION

1.1 Background

Wave energy converters (WECs) are a relatively new form of renewable energy device, which bring with them challenges in harnessing this vast source of energy. Due to the stochastic nature of ocean waves, controlling these devices for maximum energy extraction is a challenging endeavor. Further complicating design and testing of these WECs, is the extreme environment in which these devices are operated. Development of this energy source requires specialized test equipment which can withstand this harsh environment and evaluation of control topologies to determine optimum solutions.

1.2 Characterizing Wave Energy Devices

The many variations in WEC topologies add unique constraints on the testing equipment. Wave energy devices may be single- or three-phase configurations with outputs of dc, ac, or variable frequency ac, and may also have variations in amplitude. The variable frequency and amplitude scenario, for example, is the result of a rotary or linear synchronous generator on a WEC oscillating back and forth with the wave input [1, 2, 3]. The Power Analysis and Data Acquisition system (PADA) developed in this work allows for testing of these devices in the ocean environment; providing an electrical load to the device under test while performing data acquisition on its output electrical characteristics.

1.3 Maximizing Power Extraction in Wave Energy Devices

Optimal energy extraction control for a WEC is well defined for simplifying assumptions, such as linear hydrodynamics and monochromatic waves [4, 5]. However, due to the stochastic nature of ocean waves, controlling these devices for maximum energy extraction in a real wave environment is a challenging endeavor. One method of overcoming these obstacles is with an adaptive control strategy such as maximum power point tracking (MPPT).

MPPT is a common control strategy used in other renewable energy industries, primarily solar [6, 7]. There has been some research in the use of MPPT for tidal turbines; however there have been few publications in the application of MPPT to ocean wave energy [8, 9, 10, 11]. MPPT was demonstrated in oscillating generator applications where the time constant dynamically changed to include one full stroke of the generator [12]. This specific example applied to energy harvesting backpacks, but the methods could be applied to wave energy.

This work investigates MPPT control of wave energy devices. A simple "perturb and observe" MPPT algorithm is applied to a WEC using both passive and active rectification of the generator's output. Both modes of operation were tested, as while some WEC designs require active control, the simplicity of using passive rectification may be desired in some cases [13, 14, 15, 16].

A literature search did not reveal previous implementation of a two-variable MPPT, and so following this validation, two-variable MPPT is investigated. This could serve in multiple applications such as controlling independent loading of two generators on a single WEC or the damping of multiple position, velocity, or acceleration dependent terms.

2. POWER ANALYSIS AND DATA ACQUISITION SYSTEM

2.1 Introduction

In this work, a portable Power Analysis and Data Acquisition system (PADA) was developed for use in the testing of WECs in a marine environment. Comprehensive testing and characterization of these WECs in the ocean is crucial for the development and selection of optimum WEC topologies. Requirements of this system include the ability to provide an electrical load to the WEC while simultaneously acquiring data on its output electrical characteristics. Systems are currently available in laboratory environments which meet these needs: adjustable resistive load banks, four-quadrant converters for regenerative loading, and standard measurement equipment such as multimeters, oscilloscopes, and power analyzers. With the desire to perform extended-duration testing in the marine environment, it became necessary to develop a system specifically suited for this task.

2.2 Design Specification

The PADA system was specified to be a fully inclusive and portable system for use in testing and characterizing ocean WECs. This requirement created unique demands for both the electrical loading and data acquisition systems.

2.2.1 Electrical Loading System

A 30 kW power rating was chosen to support small-scale WECs. Due to the possible variation in the electrical output configuration of these devices, a universal loading system capable of accepting a variety of inputs was desired. WECs may be single- or three-phase configurations with the possibility of producing dc, ac, or variable frequency ac output, and may have variable amplitudes. The PADA

system had to be capable of accommodating these input configurations at a range of voltage and current ratings.

2.2.2 Data Acquisition System

For characterization of wave energy devices, it is desired to measure output voltage and current waveforms with respect to time at high sampling rates. From these waveforms, post processing of the data can provide RMS voltage and current, frequency, real and reactive power, power factor, harmonic content, and other quantitative analyses [17].

2.3 Converter Topologies

Loading systems utilizing active converters are often used in power laboratory environments. In the case of four-quadrant converters, most of the load power may be regenerated onto the utility grid with the only system losses attributed to efficiency of the power conversion process. A typical three-phase, four-quadrant converter is realized in the form of two back-to-back three-phase converters as shown in Fig. 2.1. In this configuration, the input converter controls power flow from the device under test while the output converter controls regeneration of power to the utility grid and maintains stability of the dc bus [18].

In addition to being highly efficient with excellent power density, active converters also have the advantage of flexibility. A three-phase active converter may be used to load single-phase ac or dc systems using two of the three available switching legs, provided the control strategy is properly altered [18]. An example of this connection is shown in Fig. 2.2. Also, active converters may be used to represent a resistive, reactive, or nonlinear load.

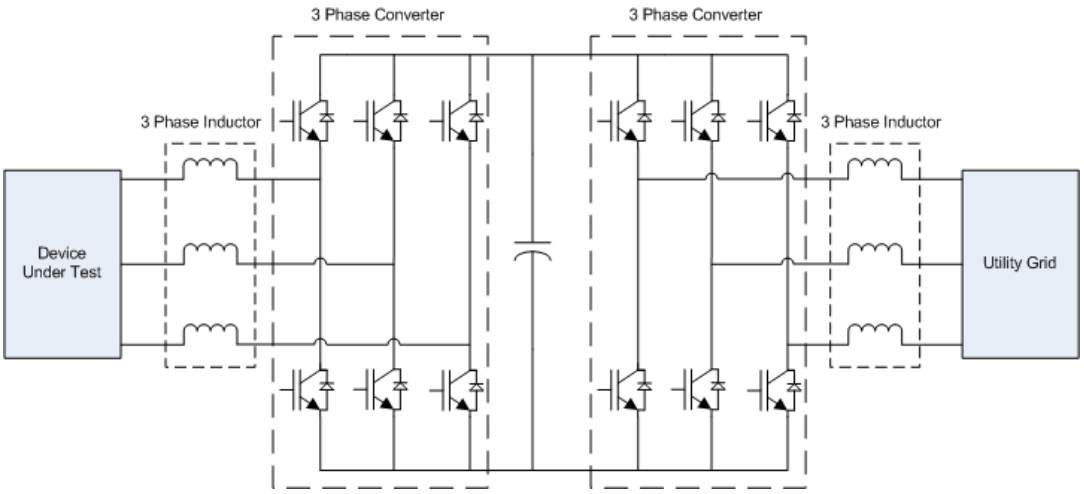

Fig. 2.1. Three-phase, four-quadrant converter.

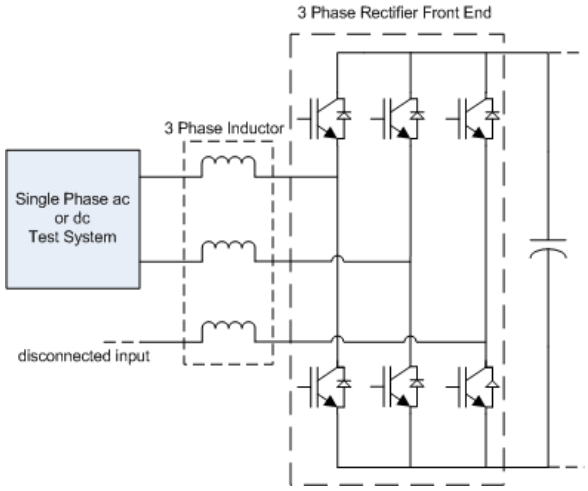

Fig. 2.2. Single-phase ac or dc loading with a three-phase converter.

As an alternative to the four-quadrant topology, the output three-phase converter could be replaced with a dc-dc converter to allow power dissipation in a fixed resistive load. In this configuration, shown in Fig. 2.3, the dc-dc buck converter controls power flow from the dc bus to a low impedance resistive load.

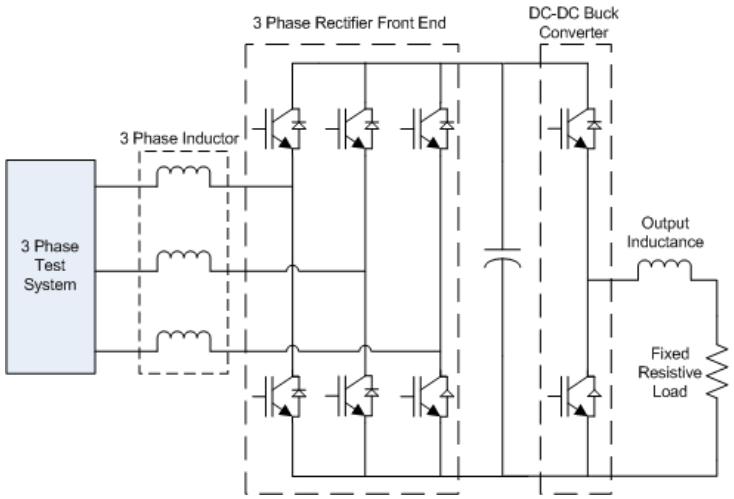

Fig. 2.3. Active three-phase converter with a controlled resistive load.

2.4 System Design and Components

To accommodate the variety of electrical inputs which may exist in WECs, the system developed in this work was designed utilizing the converter topology shown in Fig. 2.3. The major system components are discussed below, including those related to system protection, power processing, data acquisition, and control. A full system schematic is provided in Fig. 2.4. The complete PADA system is shown in Fig. 2.5 with internal components shown in Fig. 2.6 and Fig. 2.7.

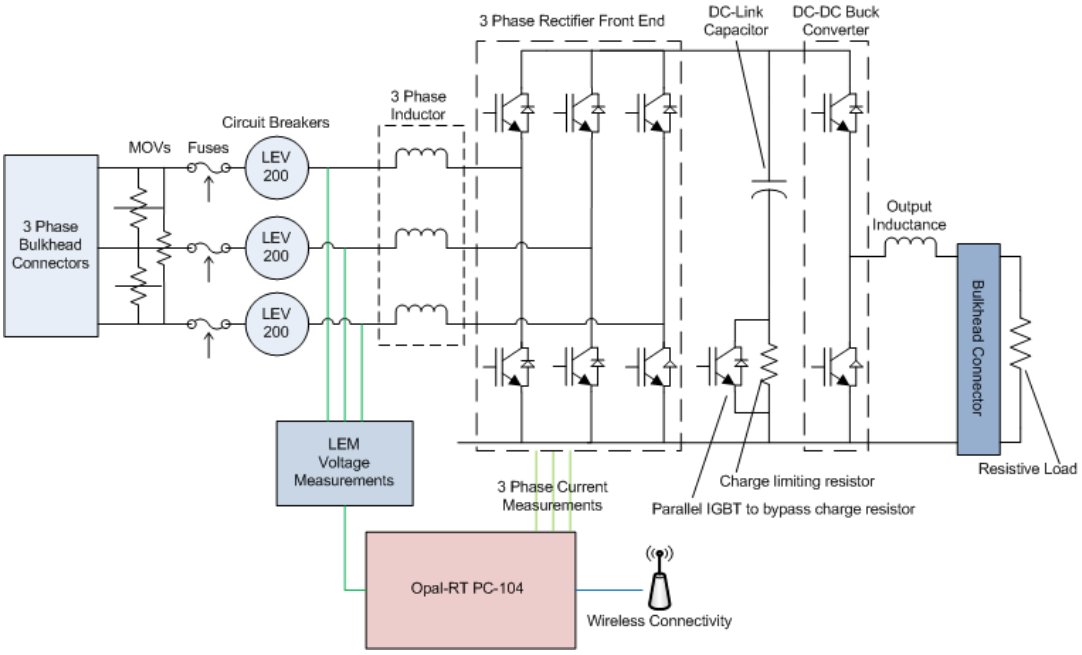

Fig. 2.4. PADA system schematic.

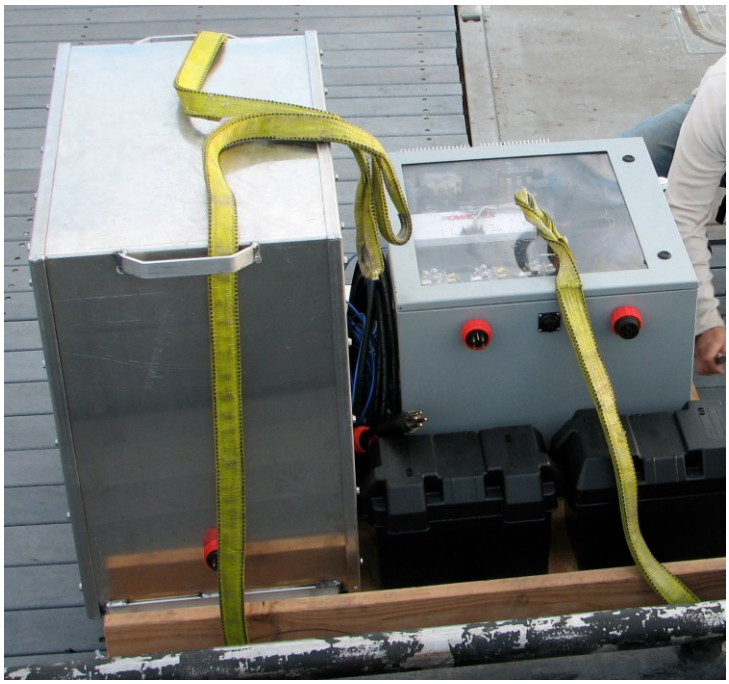

Fig. 2.5. PADA system with resistive load bank during ocean testing.

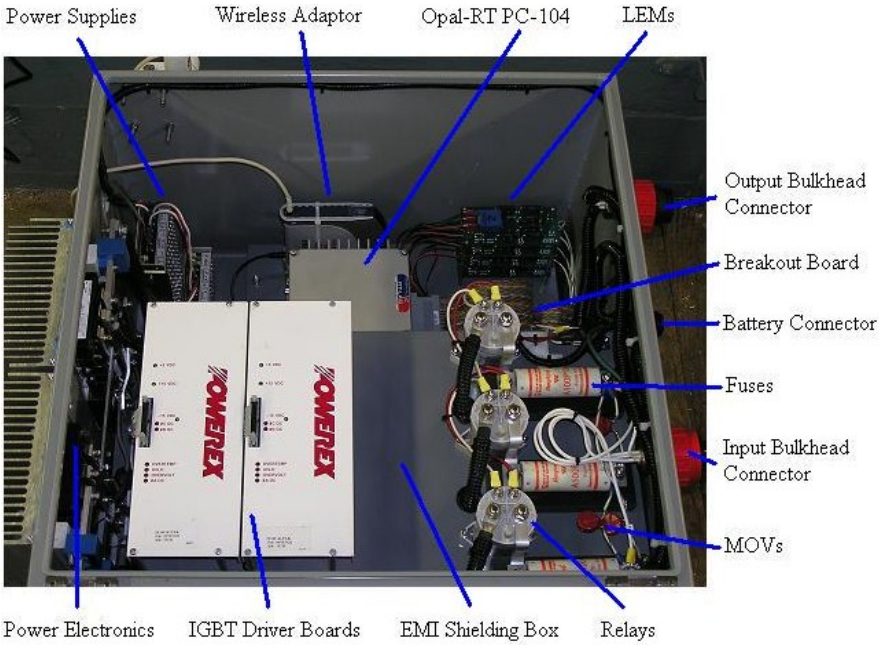

Fig. 2.6. PADA system internal components.

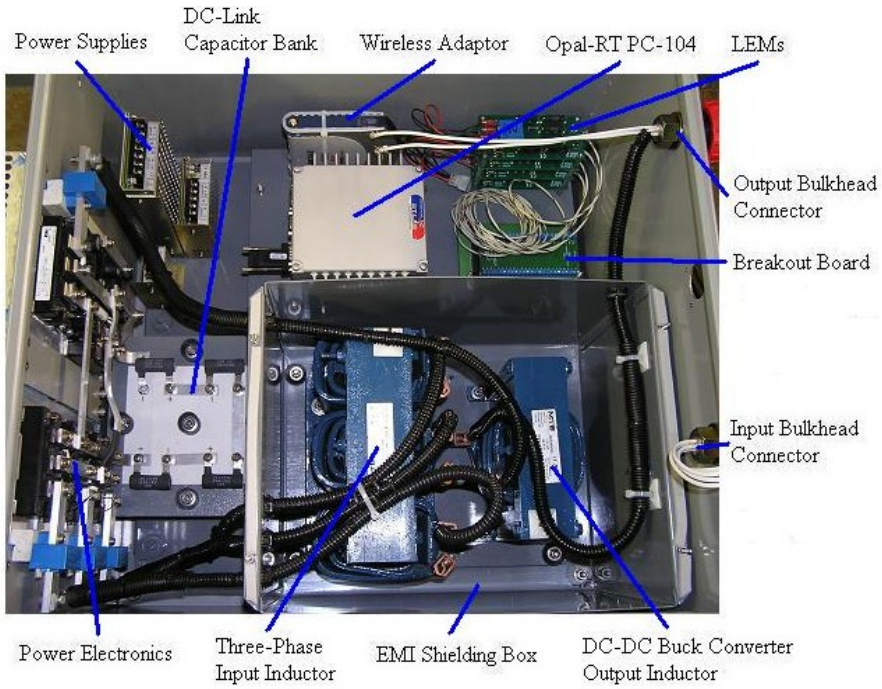

Fig. 2.7. PADA system internal components.

2.4.1 Power Electronics

The power electronic components of the PADA are comprised of two Powerex Pow-R-Pak IGBT (Insulated-Gate Bipolar Transistor) assemblies. These pre-configured assemblies are arranged in a two-leg, H-bridge configuration with an integrated IGBT gate driver board by Applied Power Systems. The driver board has built-in protection against dc bus overvoltage and input phase overcurrent. The boards also contain built in dead-time circuitry. Dead time is the period of time between the gating of complimentary switches, which is necessary to prevent shorting of the dc bus. One H-bridge assembly and one leg from the second assembly create the three-phase active rectifier front-end, while the remaining leg of the second assembly becomes the dc-dc buck converter for controlling power dissipation in the fixed resistive load. The IGBTs utilized in these assemblies are rated for 1200 volts with a 75 amp continuous current rating and are capable of switching frequencies up to 15 kHz. Each IGBT and reverse-connected diode pair have been fitted with a resistor-capacitor-diode (RCD) snubber circuit to control voltage spikes at IGBT turn-off which could exceed their rated voltage.

2.4.2 Opal-RT PC/104 Rapid Prototyper

The PC/104 Rapid Prototyper by Opal-RT is a real-time hardware-in-loop simulator which performs the data acquisition and control of the PADA. When utilizing eight analog inputs, this system is capable of 250 μs data sampling and closed loop control intervals. A user can control operation of the PADA while monitoring performance data in real-time from a host computer. Signals of interest can be recorded as time-stamped data to the internal flash memory storage for post-processing at a later time, while packets of data can be sent to the host computer for observation. A screenshot from the host computer, providing an example of the data feedback, is shown in Fig. 2.8. The ability to store data allows extended periods of testing to be conducted without constant input or observation by the

user. The duration of testing will be limited only by storage capacity and is directly affected by sampling rates and the number of signals being recorded.

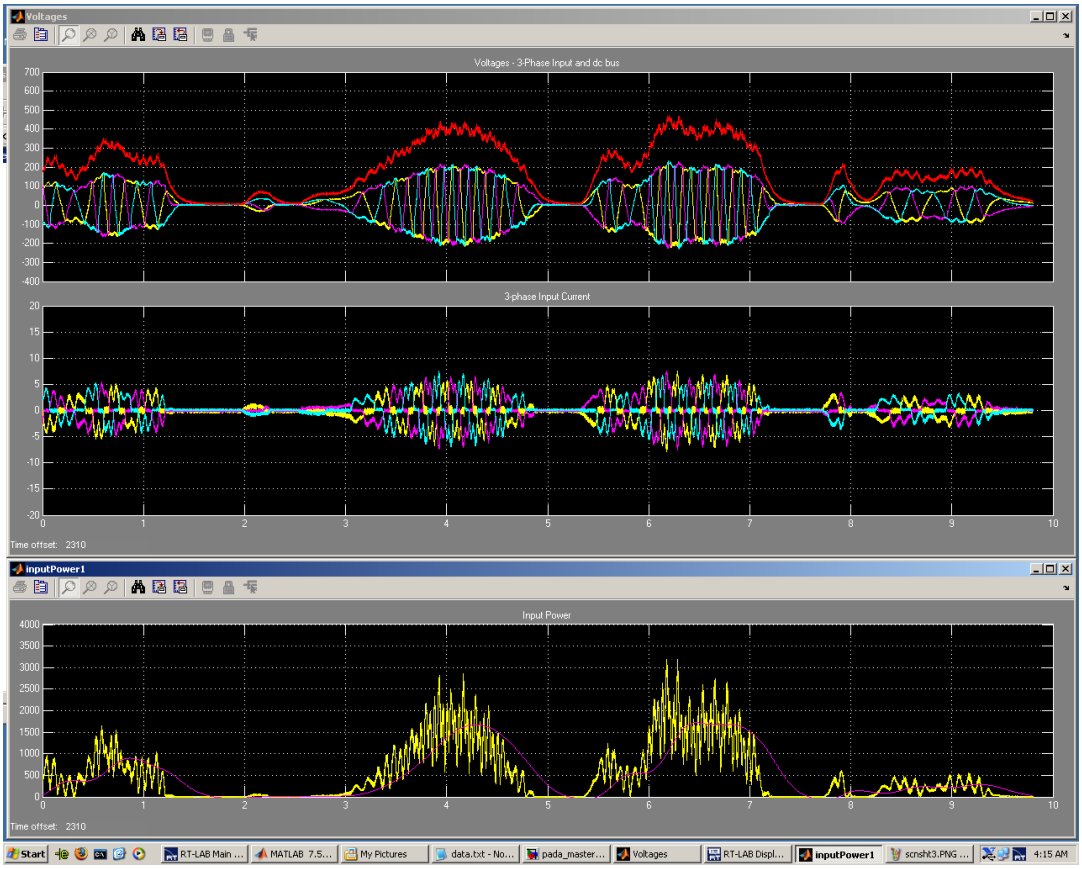

Fig. 2.8. Screenshot from host computer; upper plot showing three-phase and dc bus voltage, middle plot showing three-phase current, and lower plot showing instantaneous and filtered input power.

2.4.3 System Protection

At the input to the PADA are three metal oxide varistors (MOVs) with a 1 kV clamping voltage rating connected line-to-line. The purpose of the MOVs is to limit overvoltage at the input of the PADA which could be caused by open-circuit wave energy generator voltages when the input circuit breakers are not closed.

Located after the MOVs are input fuses rated to protect the three-phase line reactor and semiconductor devices used in the three-phase active rectifier. These fuses are not sized to protect the wave energy device under test, but rather are sized for the full rated current capacity of the system components.

Following the input fuses is a set of Tyco Electronics LEV200 mechanical relays controlled by digital I/O of the controller through a solid state relay. The use of a solid state relay as an intermediate stage was needed as the input current requirement of the mechanical relays exceeds that which can be sourced by the controller's digital I/O. Additionally, system protection can be enhanced as the control scheme may be configured to open the input relays in the event of an overcurrent condition or if another type of fault occurs.

2.4.4 System Input and Output Inductance

At the input to the three-phase active rectifier front-end is a three-phase inductor or line reactor. The purpose of this element is to limit current ripple and provide some isolation between the pulsed voltage waveforms produced by the pulse-width-modulated (PWM) rectifier bridge and the wave energy device under test. A single-phase reactor is located at the output of the dc-dc buck converter to reduce current ripple in the low impedance resistive load.

2.4.5 Voltage and Current Transducers

LEM voltage transducers provide isolation for measurement of the three-phase input and dc bus voltages. These voltage transducers source a current proportional to their input voltage. At the analog input to the controller, a properly scaled resistor is connected in series with this current source, across which an analog voltage proportional to the input voltage is measured.

Current transducers are integrated with the Powerex bridge assemblies, providing current measurement at each leg of the three-phase converter and the dc-

dc buck converter. These signals are isolated in the Applied Power Systems driver boards and a voltage proportional to current is provided as an output for interface with the control system.

2.4.6 Inrush Current Limitation

In series with the dc bus capacitor bank are two series-connected 10 ohm thick film semiconductor resistors. The purpose of these resistors is to limit the inrush current from the device under test to the dc bus at the instant the input circuit breakers are closed. This adds a level of protection against overcurrent of low-power WECs during initial closing of the input relays and capacitor charging. Connected in parallel with these resistors is an IGBT which can be gated to short the resistors after the initial inrush current occurs. These charge-limiting resistors have not yet been implemented and are currently bypassed.

2.4.7 System Enclosure

Operation in the ocean environment requires careful consideration be taken with respect to component enclosures, as the electronics should not be exposed to the corrosive sea water. It was expected that the PADA could be exposed to wave splash and occasional submersion. To ensure the data acquisition and control systems do not get exposed to the corrosive sea water, a waterproof enclosure was utilized. For connections through the enclosure, waterproof bulkhead connectors are used for all power- and signal-level connections to maintain the integrity of the enclosure.

2.5 Ocean Testing of a Wave Energy Converter

In September of 2008, Oregon State University tested a point absorber WEC in the ocean [19]. This WEC, called the L10, is a point absorber system containing a 10 kW linear generator. The system design includes a central spar

which is motion-restricted by a submerged damper plate, surrounded by a float which is actuated by the ocean waves. The central spar contains armature coils with the outer float housing an array of permanent magnets. The relative motion between the coils in the spar and magnets in the float produces electricity. Details on the construction of buoy and generator can be found in [20, 21, 22].

Electrical loading of the WEC and data acquisition were carried out utilizing the PADA system developed in this work. At the time when this testing was scheduled, active control of the PADA input rectifier was not yet possible. For that reason, the three-phase input rectifier was left uncontrolled and operated passively as a three-phase diode bridge rectifier.

2.5.1 Passive Rectifier Operation

With the input rectifier operating passively, electrical loading of the device under test was controlled by the output dc-dc buck converter. Two methods of control were utilized during this testing, a fixed duty ratio method and a form of constant current control. The first method simply applies a user-defined fixed duty ratio to the buck converter. In this control, the buck converter essentially represents a variable resistive load connected to the dc bus. By varying the buck converter duty ratio, the effective load resistance on the dc bus is given by equation (2.1).

$$R_{var} = {R_L}/{d^2} \tag{2.1}$$

The effective variable load resistance is R_{var}, where R_L is the fixed resistive load at the output of the dc-dc buck converter in Fig. 3 and d is the buck converter duty ratio.

The second method of control implemented was a form of constant current control. By manipulating the duty ratio of the buck converter, the dc bus voltage was controlled to maintain a fixed input current space vector magnitude. If the actual magnitude was less than the desired magnitude, the buck converter duty ratio

was increased to reduce the impedance of the effective load and draw more current from the generator. As the input current increased beyond the desired value, the duty ratio decreased to raise the effective load impedance and reduce the current drawn from the generator. The buck converter duty ratio in this method was limited between 0 and 0.8 and controlled by a proportional-integral controller on the error in the input current space vector magnitude.

2.5.2 Hardware Results

Recording durations during ocean testing included both twenty minute and one hour time intervals. During the twenty minute data acquisition sessions, signals recorded included three-phase voltage and current, dc bus voltage, and duty ratio of the dc-dc buck converter. Data sampling during the twenty minute sessions was slowed to a 1 ms sampling interval to conserve storage space. Electrical frequencies expected from the WEC were below 30 Hz, providing good resolution with the reduced sampling rate. A sample of data recorded during these twenty minute sessions using the fixed duty ratio control is shown in Fig. 2.9 and using the constant current reference control in Fig. 2.10. It should be noted that current is referenced positive out of the PADA rectifier front-end.

The one hour acquisition sessions were conducted to record power output of the WEC over an extended period of time. To conserve data storage space, the sampling interval was reduced to 10 ms and the power was calculated in the acquisition model to allow the single power value to be recorded as opposed to three-phase voltage and current signals. A sample of data recorded during these one hour sessions using the constant current reference control is shown in Fig. 2.11.

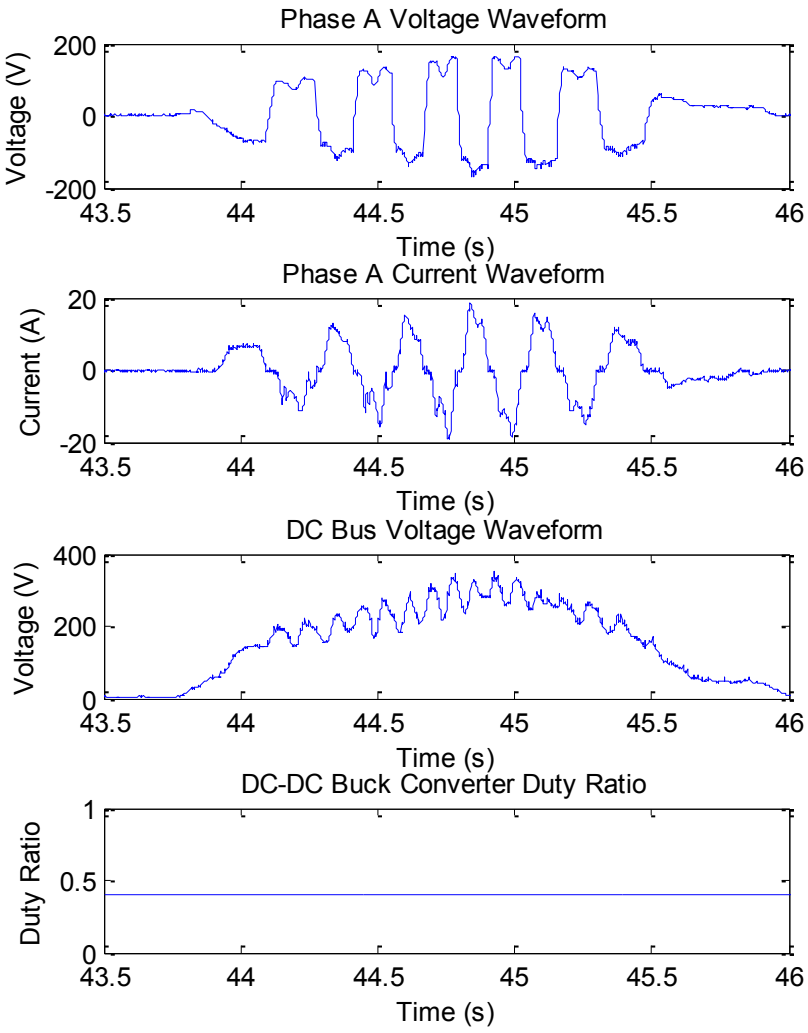

Fig. 2.9. Recorded waveforms with a fixed duty ratio of 0.4.

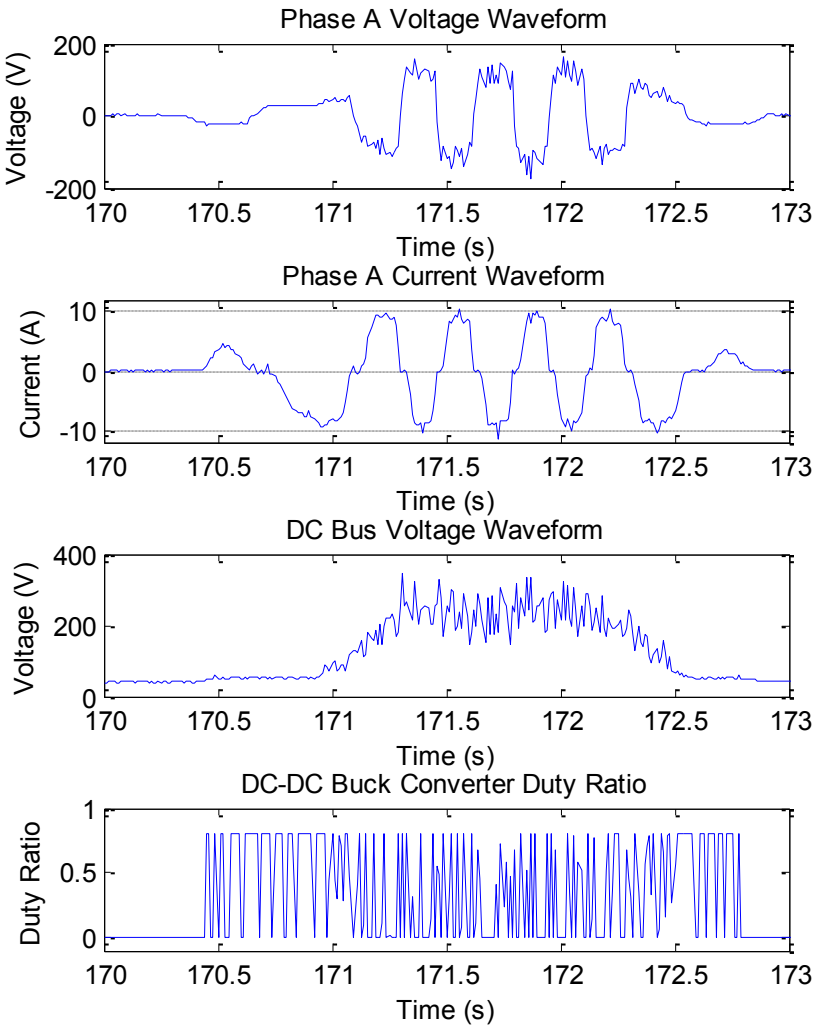

Fig. 2.10. Recorded waveforms with a 10 amp current reference.

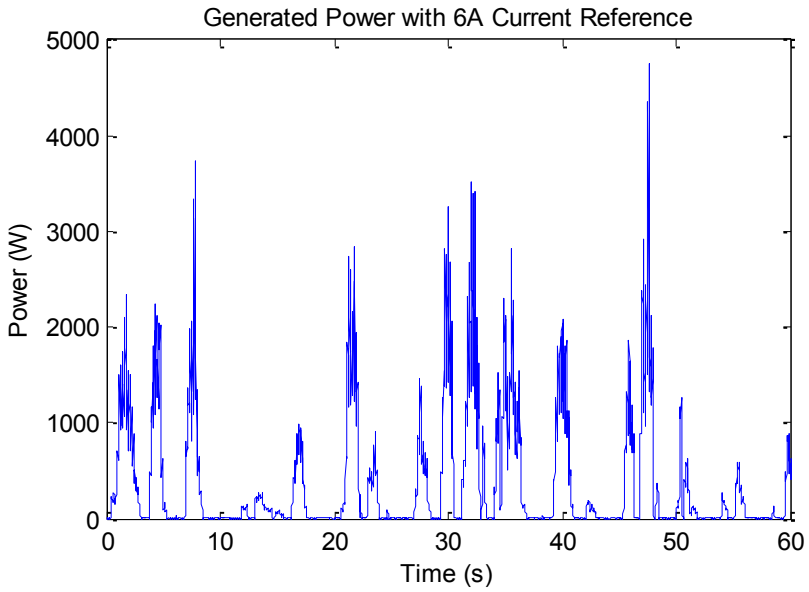

Fig. 2.11. Recorded power waveform with a 6 amp current reference.

3. EXPERIMENTAL SETUP

3.1 Experimental Setup Overview

For laboratory testing of MPPT in WECs, a novel test setup was utilized. This test setup was comprised of three main components: a wave energy linear test bed, the 30 kW PADA developed in this work, and the active components of the L10 WEC, previously mentioned in section 2.5. The active components of the L10 WEC included the central spar containing the armature coils and the outer section containing the permanent magnets, absent the float. The active components of the L10 WEC are mounted in the LTB, which moves the WEC through an ocean wave motion profile. The output of the WEC is connected to the PADA to provide electrical loading and data acquisition.

3.2 Wave Energy Linear Test Bed

The Wave Energy Linear Test Bed (LTB) is a unique test bed designed for testing vertically-oriented ocean wave energy systems and is located in the Wallace Energy Systems and Renewables Facility (WESRF) at Oregon State University [23]. The active components of the L10 WEC were mounted in the LTB, shown in Fig. 3.1. The LTB can be programmed with position vs. time motion profiles, including those of actual wave data, and moves the device under test through this profile while performing data acquisition including position, speed, acceleration, and force.

Fig. 3.1. L10 active components mounted in the Wave Energy Linear Test Bed at Oregon State University.

3.3 Position vs. Time Profile

For these experiments, the position vs. time profile programmed into the LTB is representative of the motion a point absorber WEC would experience in the ocean. This motion profile was developed in previous work performed at Oregon State University and is representative of a sea state with a significant wave height of 1.25 meters and dominant period of 7.5 seconds [24, 25, 26]. This fifteen-minute motion profile is shown in Fig. 3.2 with a shorter duration example shown in Fig. 3.3.

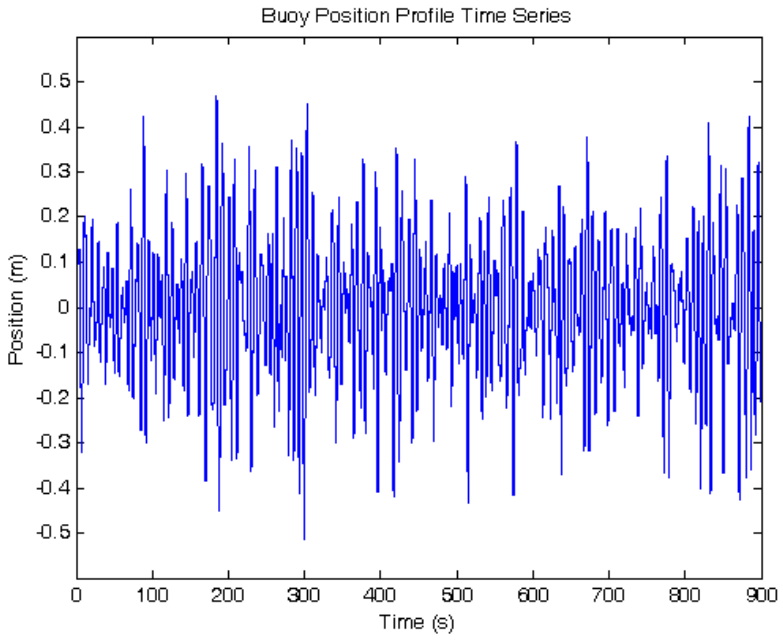

Fig. 3.2. Fifteen-minute buoy position profile.

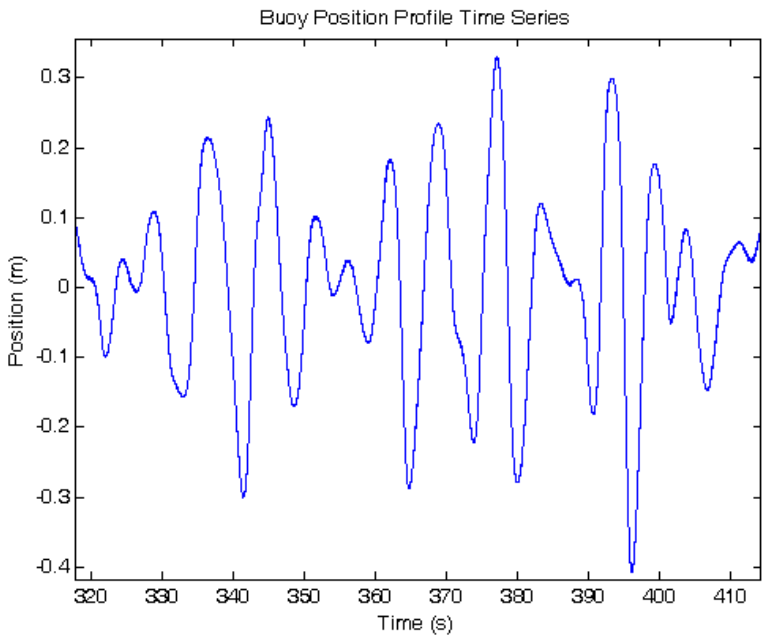

Fig. 3.3. Short-duration example of buoy position profile.

4. SYSTEM SIMULATION

4.1 Simulation Overview

A detailed system model was developed in MATLAB Simulink to allow for evaluation of control strategies in a simulated environment. The full system model includes all components utilized in the experimental setup; the L10 linear generator driven with the LTB, with loading and control performed by the PADA. The top level of the full system schematic in MATLAB Simulink is shown in Fig. 4.1. This top level contains LTB and PADA blocks; the L10 linear generator is represented by the PMLTG_Coils block modeling the back-EMF (electromotive force) of the generator and three phase blocks modeling the per-phase resistance and inductance.

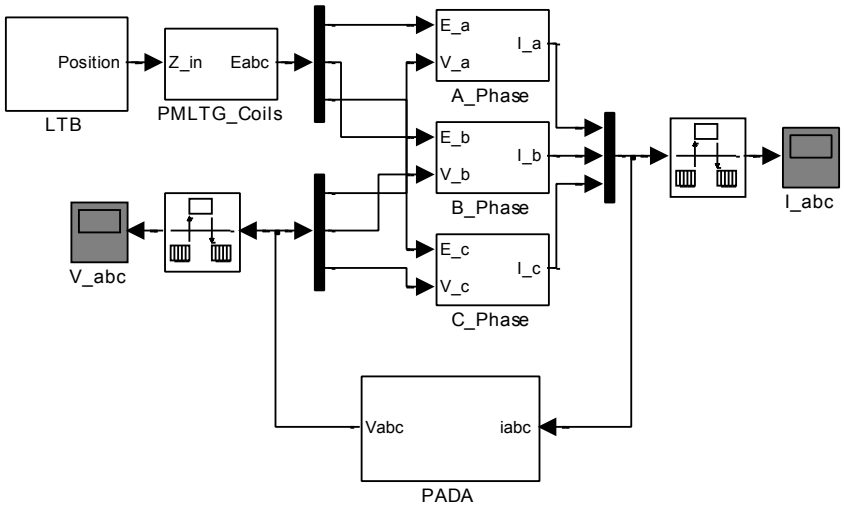

Fig. 4.1. Full system simulation model in MATLAB Simulink.

4.2 LTB / L10 Simulation Model

The L10 simulation model was produced in previous work at Oregon State University [20, 21] and was modified in this work to represent the L10 generator being driven by the LTB. The LTB block uses the same position vs. time profile used in experimental testing to produce the position of the L10 armature coils in relation to the magnet section. This position signal goes to the PMLTG_Coils (Permanent Magnet Linear Tubular Generator coils) block, contents shown in Fig. 4.2, which creates the back-EMF voltage induced in each armature coil and sums coils of each phase together to produce the three-phase back-EMF signal. The contents of one coil block from the PMLTG_Coils model is shown in Fig. 4.3. In this work, the physical coil spacing and per-phase back-EMF gains were tuned to more closely match the experimental results. The three-phase back-EMF produced is then sent to the phase blocks, contents shown in Fig. 4.4, which use the per-phase back-EMF and the terminal voltage produced by the PADA block to create the current produced by each generator phase.

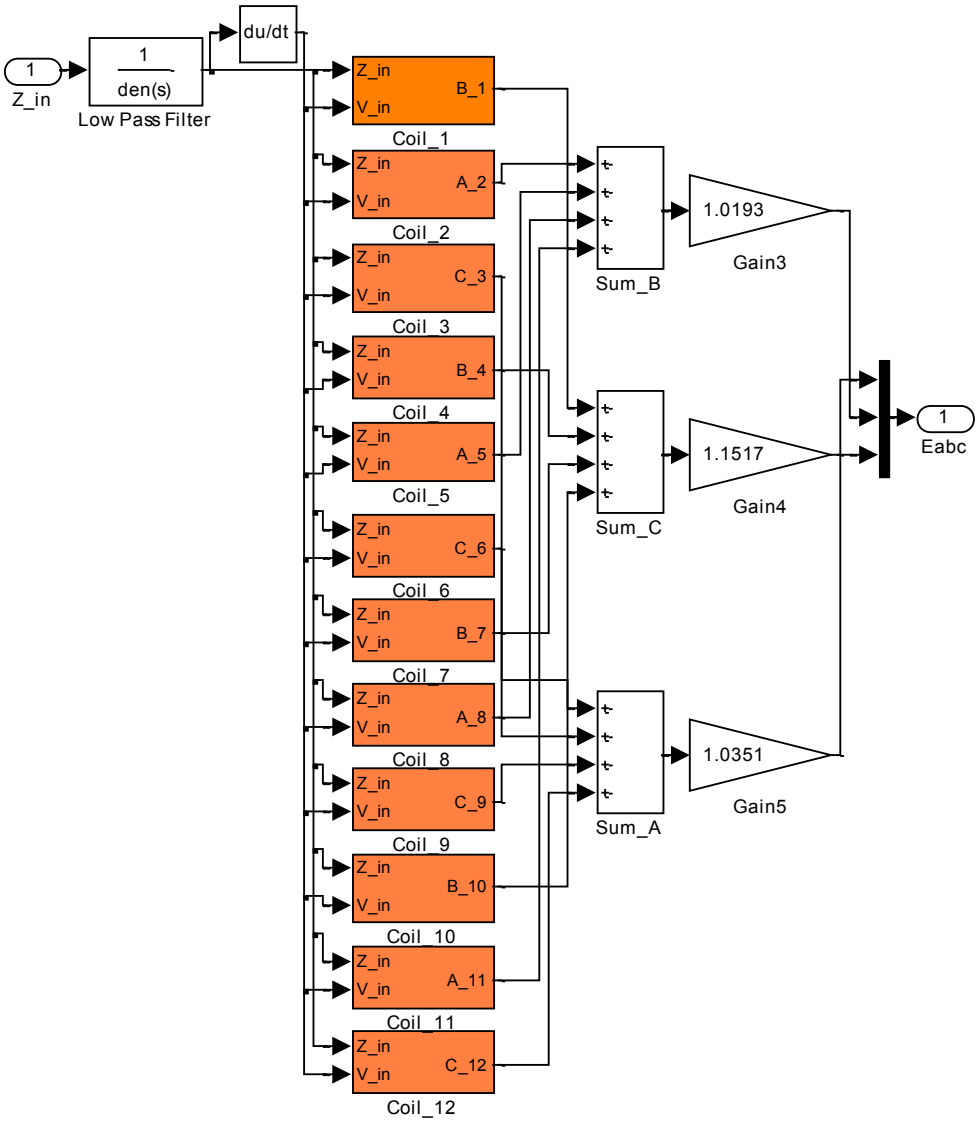

Fig. 4.2. Contents of PMLTG_Coils block.

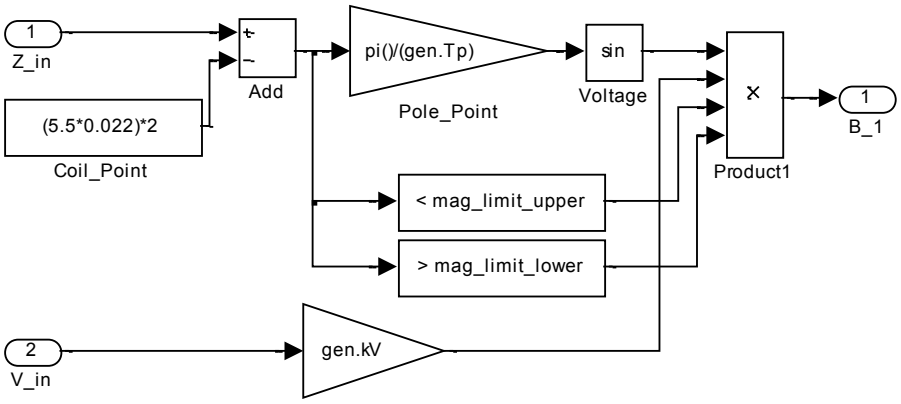

Fig. 4.3. Contents of one coil block in PMLTG_Coils.

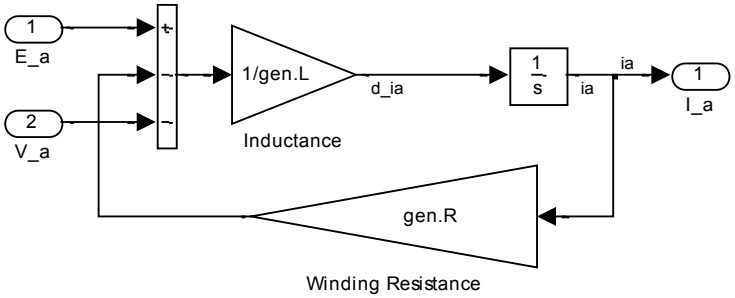

Fig. 4.4. Contents of the phase blocks.

4.3 Power Analysis and Data Acquisition System Model

In the full system simulation, two PADA models were implemented; a passive rectifier model and an active rectifier model. The purpose of these models was to accurately reproduce the terminal voltages at the input of the three-phase rectifier. Because the terminal voltage produced is largely dependent upon the dc bus voltage, the dc bus capacitance and output buck converter with load resistor were included in the PADA model.

4.3.1 Passive Rectifier Model

The passive rectifier PADA model in MATLAB Simulink is shown in Fig. 4.5. This model contains a simplified diode model for each leg of the rectifier, contents of which are shown in Fig. 4.6. The simplified diode model determines if the input phase current is positive or negative and applies the correct voltage for each case to the rectifier terminal. If the current is positive, the sum of the positive half of the dc bus voltage and the voltage across the input inductance is applied to the PADA input terminal. Similarly, if the current is negative, the sum of the negative half of the dc bus voltage and the voltage across the input inductance is applied to the PADA input terminal.

The dc bus of the passive rectifier model finds the total current in the dc bus capacitance using the sum of the input current from the three-phase rectifier and the output current to the load. The dc bus voltage is controlled by the duty ratio provided by the control scheme being simulated. The product of this duty ratio and the dc bus voltage produces the load voltage applied to the fixed resistive load. The impedance of this load is used to calculate the load current, which is then multiplied with the duty ratio to find the load current out of the dc bus capacitance.

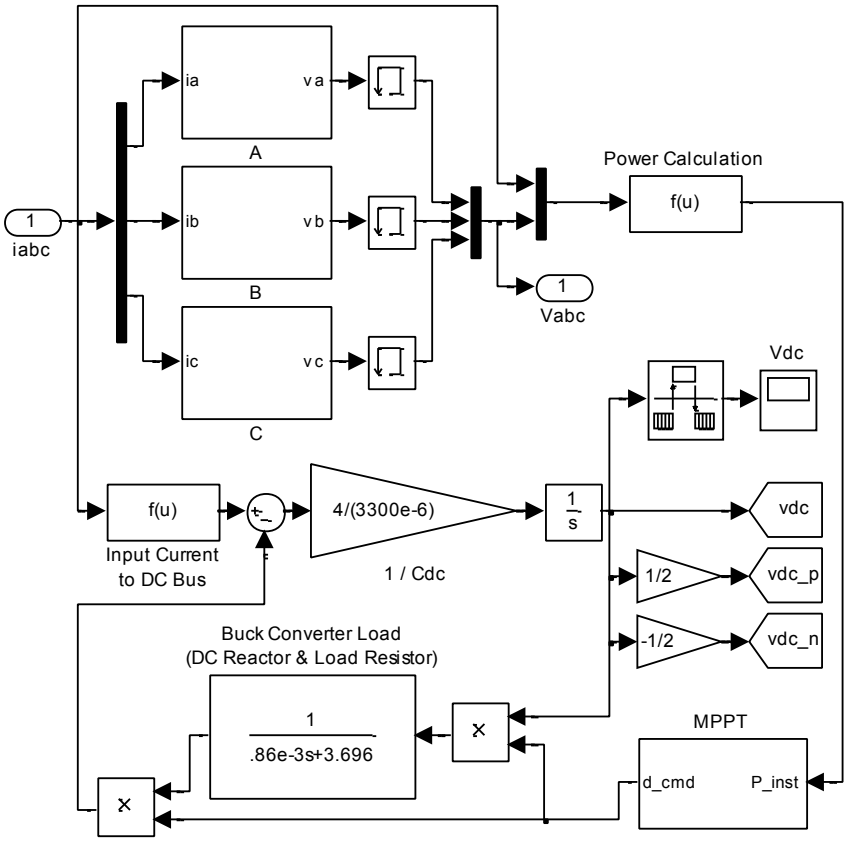

Fig. 4.5. Passive rectifier PADA model.

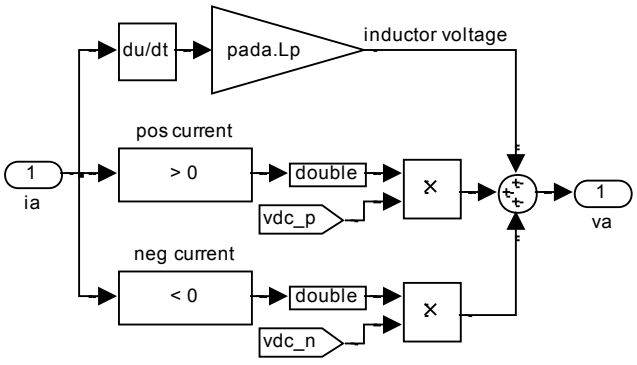

Fig. 4.6. Passive rectifier simplified diode model.

4.3.2 Active Rectifier Average Model

The active rectifier PADA model is an “average” model, producing the average voltages applied to the rectifier terminals as opposed to the pulse-width-modulated (PWM) voltage a switching model would produce. An “average” model is used to increase simulation speed by allowing a larger simulation time step to be used than could be implemented with a switching model. In this model, the PADA terminal voltage is the product of the input current and a commanded resistance, emulating a three-phase resistive load. The commanded voltage is scaled by the dc bus voltage to produce a commanded duty ratio for each leg of the inverter. This duty ratio is limited from 0.05 to 0.95, and then scaled by the dc bus voltage back to a commanded terminal voltage.

The dc bus voltage is modeled as in the passive model, with the exception of the buck converter operation. The buck converter duty ratio is now controlled by a simple proportional controller with a reference of 600V and a maximum of 650V. Within this 50V range, the duty ratio is scaled linearly from 0 to 1. The MATLAB Simulink model for the PADA active rectifier is shown in Fig. 4.7.

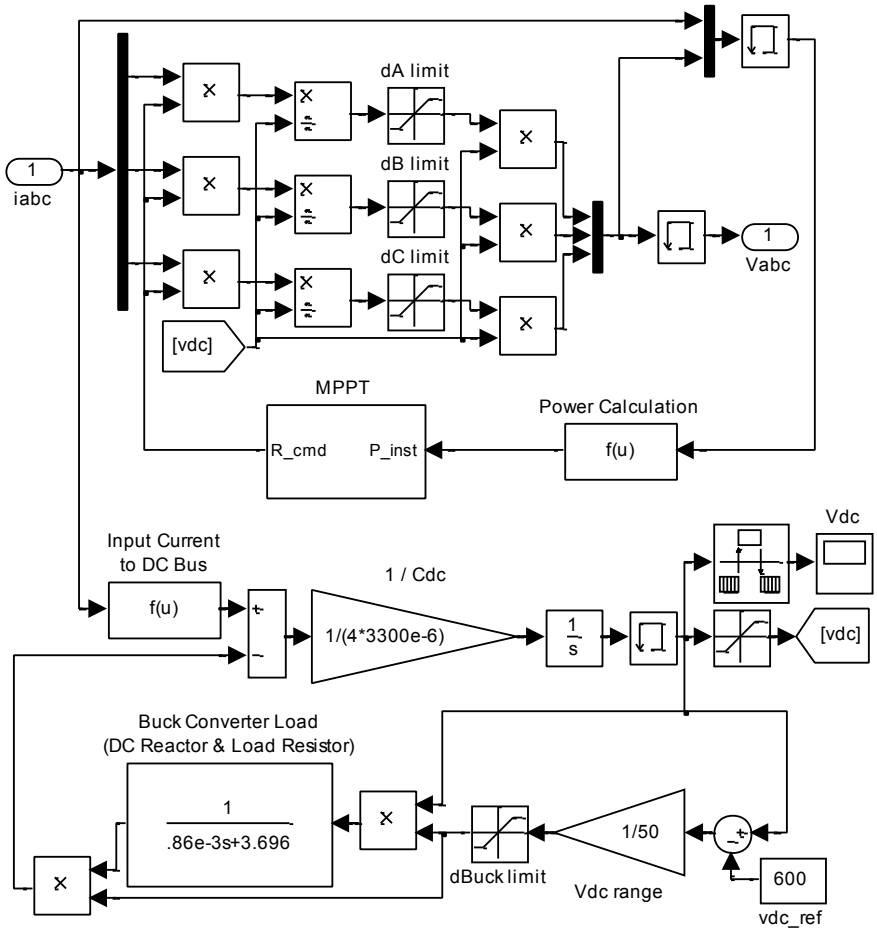

Fig. 4.7. Active rectifier PADA model.

4.4 Model Tuning and Verification

The full system simulation was tuned to match the experimental setup to ensure good correlation between simulation and experimental results. In matching the L10 model with hardware, the first step was matching the back-EMF produced in simulation with the open-circuit voltage produced by the L10 driven by the LTB. Following back-EMF tuning, the L10 simulation model phase resistance and

inductance were tuned so RMS voltage and current measurements in simulation matched those in the experimental setup.

4.4.1 L10 Back-EMF Tuning

To compare simulation back-EMF with experimental open-circuit voltage, the position profile described in section 3.3 was run on both platforms and the average RMS voltages over the 15 minute period were compared, then the phase back-EMF gains in the model were adjusted until the results were in agreement.

Upon comparison of the voltage waveforms produced by each platform, even though the RMS values were in agreement, there was significant mismatch between the experimental and simulation phase voltage waveforms. This mismatch is shown in Fig. 4.8. As shown, the phase voltage from simulation matches the average experimental phase voltage, however the experimental voltage waveform contains significant ripple. This voltage ripple is due to cogging forces in the generator. Combined with flex in the LTB carriage, these cogging forces create a mismatch between the position profile and the actual position of the generator, resulting in a significant ripple in generator velocity. Since the voltage produced by the generator is proportional to velocity, this effect must be accounted for in the simulation.

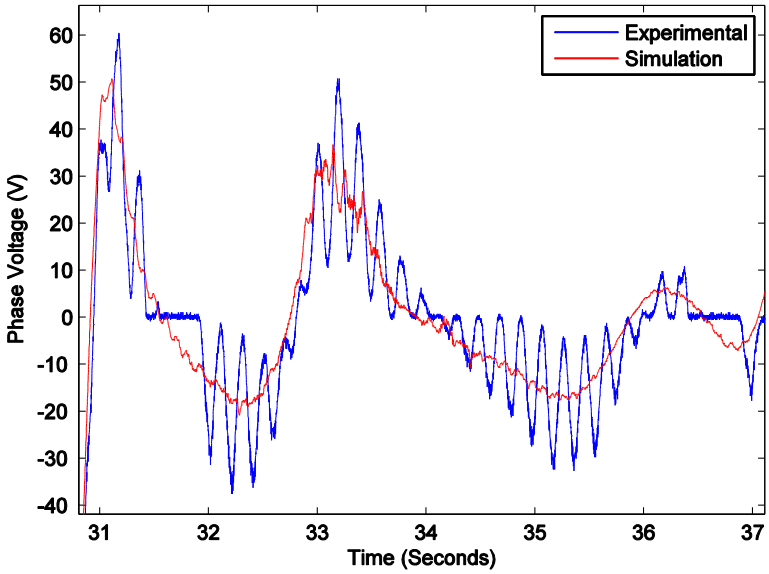

Fig. 4.8. Phase voltage waveform mismatch.

Since force can be measured by the LTB in addition to the commanded position, it was desired to determine the spring constant of the LTB carriage. With this spring constant and the force measurements, the position profile from section 3.3 could be compensated to include the velocity ripple in the experimental setup. To determine this spring constant, the L10 generator components were held in place while the LTB was commanded a sine wave in position with amplitude of 5 mm and frequency of 0.1 Hz. Because the L10 components were held stationary, the spring constant of the carriage can be found by dividing the measured force amplitude by the commanded position amplitude. The spring constant, k_s, was found to be 1.36×10^6 Newtons per meter. The commanded position and recorded force scaled by the spring constant are shown in Fig. 4.9.

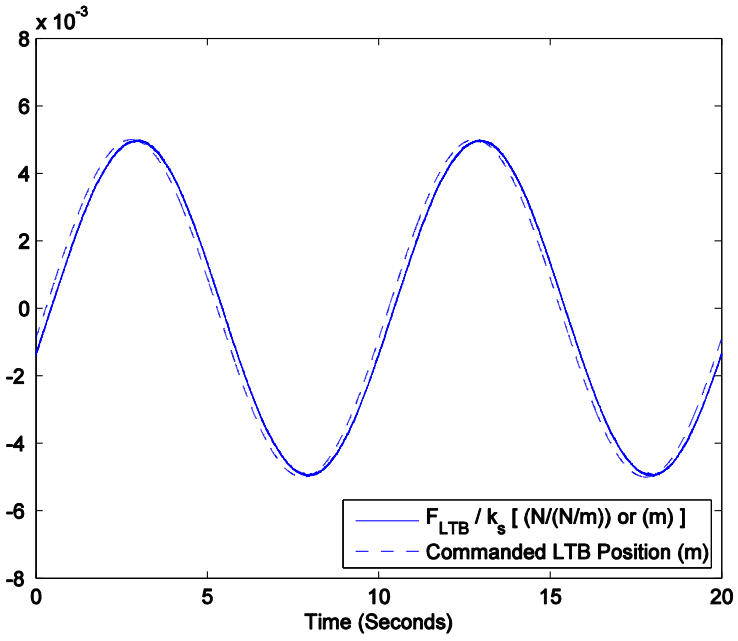

Fig. 4.9. Commanded LTB position and commanded force scaled by the LTB carriage spring constant.

To compensate the position profile in section 3.3 with the spring constant of the LTB carriage, the applied force was recorded while running the LTB through the position profile. The position profile now used in simulation, $position_{sim}$, is equal to the position profile from section 3.3 used in experimental testing, $position_{exp}$, added to the experimental force profile, F_{LTB}, scaled by the LTB carriage spring constant, k_s, as in equation (4.1).

$$position_{sim} = position_{exp} + {}^{F_{LTB}}/_{k_s} \tag{4.1}$$

The compensated position for simulation is shown with the original position for experimental testing in Fig. 4.10. Using this compensated position profile, the simulation phase voltage now closely matches the experimental, as shown in Fig. 4.11.

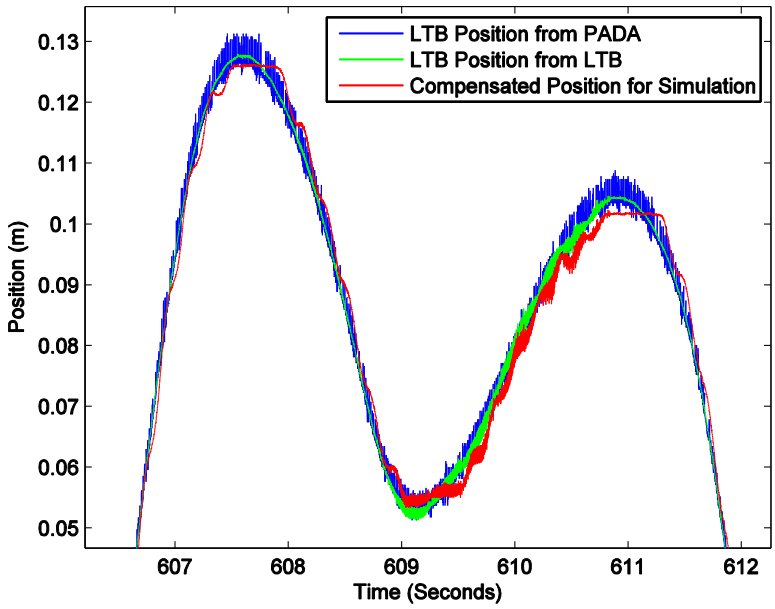

Fig. 4.10. Compensated position for simulation shown with original position for experimental testing recorded by both the PADA and LTB.

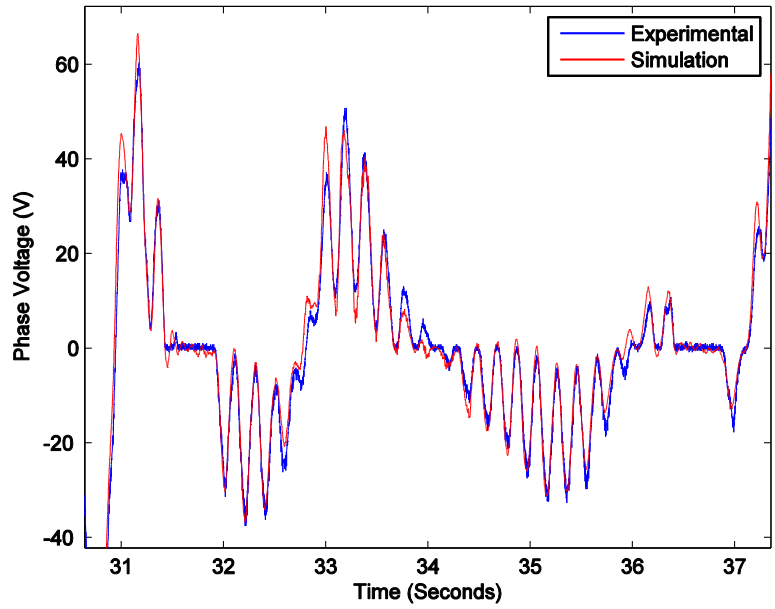

Fig. 4.11. Experimental and simulation phase voltage waveforms using the compensated position profile in simulation.

4.4.2 L10 Phase Resistance and Inductance Tuning

Following tuning the back-EMF in simulation, the phase resistance and inductance of the L10 model were adjusted to match the actual values for the L10 generator. By comparing the RMS voltage and current values for experimental and simulation results with identical loading, the error in the simulation model phase resistance was determined. The resistance was lowered in simulation by approximately 18%, resulting in RMS voltage and current values with less than 0.1% error between experimental and simulation results. With the excellent correlation between experimental and simulation results following tuning of the phase resistance, tuning the phase inductance was found to be unnecessary.

4.4.3 PADA Model Verification

For verification of the passive and active rectifier models following tuning of the L10 model, simulation and experimental results were compared for each. For the passive model, results were compared with a buck converter duty ratio of 0.8 to maximize the current drawn from the generator. The phase voltage and current waveforms are shown for both experimental and simulation in Fig. 4.12. Similarly, experimental and simulation results were compared for the active model. Phase voltage and current for both are shown in Fig. 4.13. As shown, the simulation results closely match the experimental results for both the passive and active rectifier models.

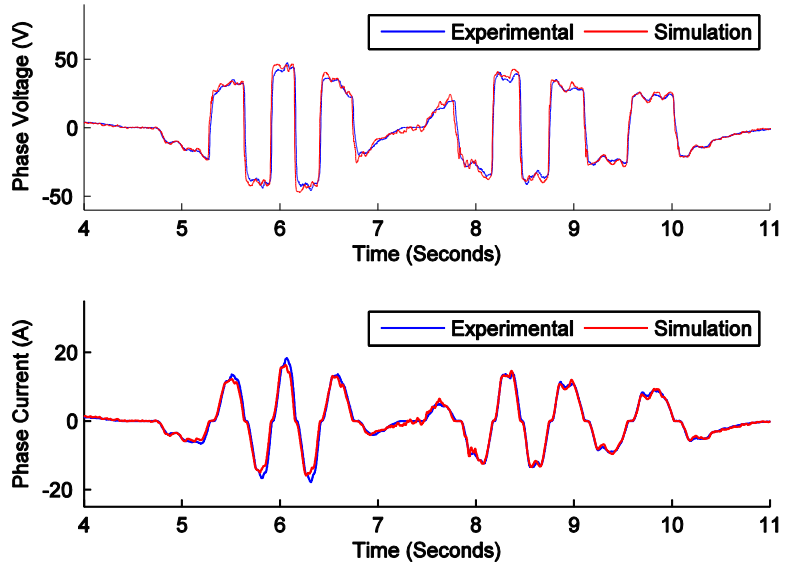

Fig. 4.12. Phase voltage and current comparison for experimental and simulation passive rectifier results.

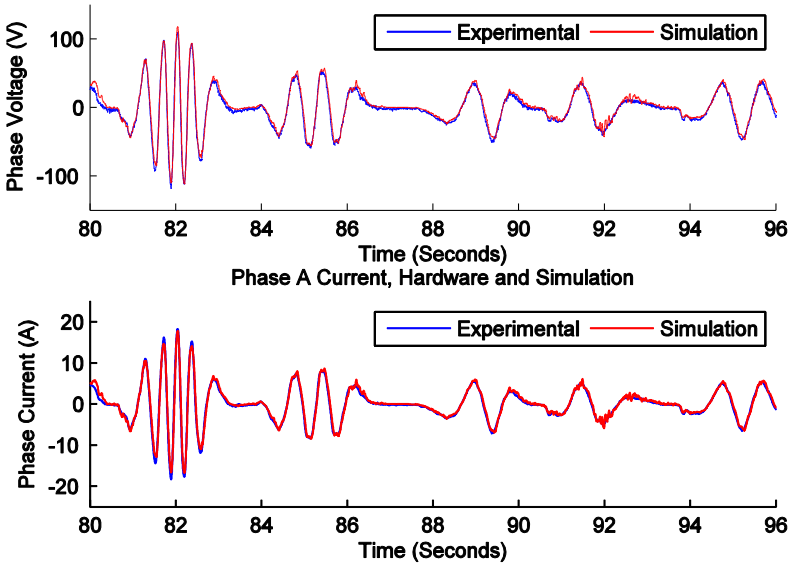

Fig. 4.13. Phase voltage and current comparison for experimental and simulation active rectifier results.

5. SINGLE-VARIABLE MAXIMUM POWER POINT TRACKING

5.1 Introduction

MPPT control was investigated for ocean WECs as a method of optimizing energy extraction in a real wave environment. Nonlinearities in hydrodynamics and WEC operation, as well as the stochastic nature of ocean waves, make this a promising solution for ocean wave energy. The first implementation of this control involved the application of a simple "perturb and observe" MPPT algorithm to a single control variable in the PADA used in electrically loading the WEC.

Since the experimental setup and full system simulation are both realized without hydrodynamics, maximum energy extraction will occur when the load impedance provided by the PADA matches that of the generator in the WEC. This realization of the system provides an optimal operating point for the algorithm to seek, however an alternate operating point may be optimal with hydrodynamics considered. Matching the generator impedance in a hydrodynamic wave environment may lead to over damping of the WEC and thus, reduced power extraction.

5.2 Control Implementation

A MATLAB Simulink model of the MPPT algorithm is shown in Fig. 5.1. This algorithm compares the current average input power to the PADA (i.e., output power of the WEC), *pavgCur*, with the average input power from the previous time interval *pavgPrev*. If the average input power has increased, the power direction, *pavgDir*, is positive and set to +1. If the average power increases, the assumption is that the previous direction of change in the MPPT control action, *cDir*, has caused the increase and so this control direction is left unchanged. Alternately, if the average input power decreases, *pavgDir* is set to -1, and it is assumed the previous control action has decreased power, so *cDir* will change sign. The product of the

current power direction, *pavgDir*, and the previous control direction, *cDirPrev*, produces the new direction of change in the MPPT control action. The output control action is then increased or decreased by a pre-determined value, *cStep*. The time interval over which average power is measured and at which control changes are made is the MPPT time constant, τ_mppt.

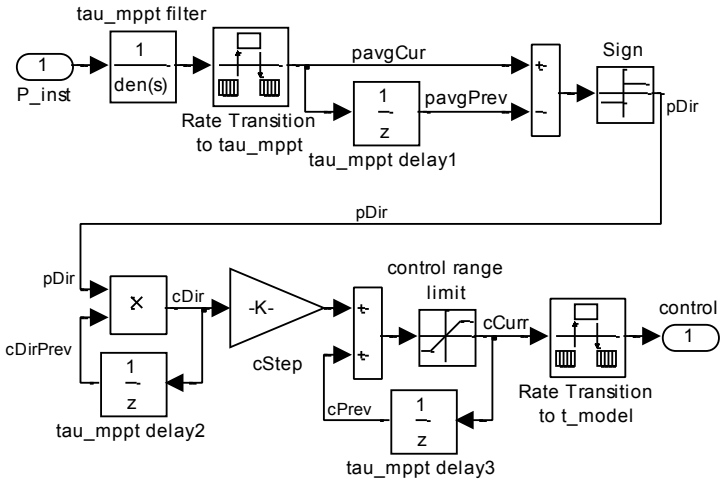

Fig. 5.1. MATLAB Simulink model of the single-variable MPPT algorithm.

5.2.1 Degrees of Freedom

The algorithm design has two degrees of freedom. First, is the step size in the control action, *cStep*. Larger steps allow the control to close more quickly on the optimal operating point; however this can cause excessive dithering and overshoot of the control variable if they are too large. Second, is the duration of the MPPT time constant, τ_mppt. This time constant represents the loop speed of the MPPT control algorithm and is the period of the corner frequency of a second-order Butterworth filter used in obtaining the average input power. The rate transition block samples this average input power at τ_mppt and is compared with the previous step's value from the unit delay block.

In solar energy applications, where MPPT is commonly implemented, the time constant can be very short as power is delivered almost at a constant steady state over short time intervals. For wave energy applications, the power is delivered to the WEC in time-varying sinusoids by the ocean waves, at relatively longer duration steady state. Because of this, there are several candidate ranges of τ_mppt for maximizing power output from the WEC. First, on a sub-second scale, the algorithm will rapidly change the control output within a wave period, trying to maximize power output at every point throughout the WEC's motion profile. Second, on a scale equivalent to the average wave period, the algorithm will tune the control output for the incoming waves, assuming they will be equivalent to the previous waves. Third, on a scale sufficiently long enough, that the system is tuned to the slowly changing sea state. As the sea state may change over the course of several hours, the control would change only a few times per day at this scale.

5.2.2 Control Implementation Objectives

The single-variable MPPT algorithm was investigated to verify the effectiveness of MPPT control on a WEC. The impact of *cStep* and τ_mppt on performance of the MPPT algorithm was evaluated to determine their optimal scales in this application.

5.3 Passive Rectifier Operation

The MPPT algorithm was evaluated both experimentally and in simulation with the PADA operating in passive mode, as described in section 2.5.1. In the passive PADA mode, the MPPT algorithm control is applied to the buck converter duty ratio, and thus *cStep* corresponds to the step size changes in this duty ratio. To minimize initial MPPT settling time, the initial buck converter duty ratio was set to the optimal value of 0.7 for each test. This optimal value was obtained by

performing a sweep of fixed duty ratios, both experimentally and in simulation. The results of these sweeps are shown in Fig. 5.2.

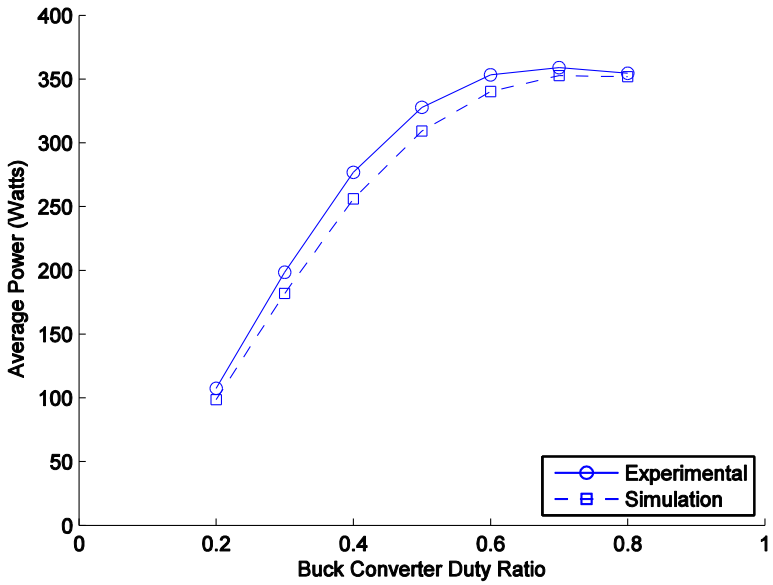

Fig. 5.2. Average power produced for fixed duty ratio sweep for experimental and simulation.

5.3.1 Experimental Results

Experimental results were obtained by driving the L10 WEC with the LTB, through the motion profile described in section 3.3, for each combination of τ_mppt and *cStep*. Values tested for *cStep* were 0.1, 0.05, 0.01 and 0.001; the step size made in duty ratio control. For each value of *cStep*, τ_mppt was varied from 0.01 to 180 seconds. Additionally, the smallest *cStep* case, 0.001, was tested with faster τ_mppt values of 0.001 and 0.005 seconds. Electrical loading and control of the WEC, as well as data acquisition, were carried out with the PADA system. Fig. 5.3 shows the average power produced at each operating point, normalized by the power obtained with the optimal fixed buck converter duty ratio of 0.7.

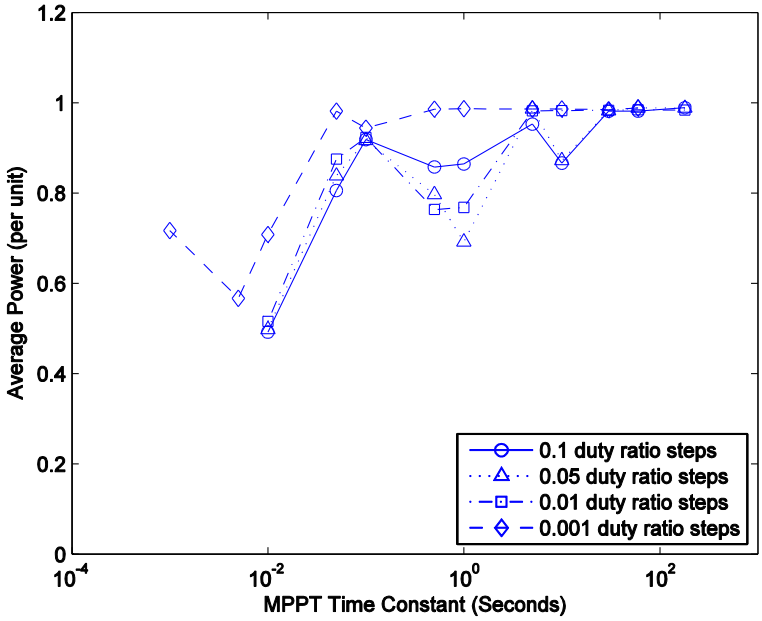

Fig. 5.3. Experimental passive rectifier results: normalized average power as a function of τ_mppt and *cStep*.

5.3.2 Simulation Results

For verification of experimental results, each case tested experimentally was also simulated in MATLAB Simulink using the models described in section 4. Additionally, the faster τ_mppt values of 0.001 and 0.005 seconds were simulated for each value of *cStep*, rather than only the 0.001 *cStep* as in the experimental results. Fig. 5.4 shows the normalized average power produced at each operating point.

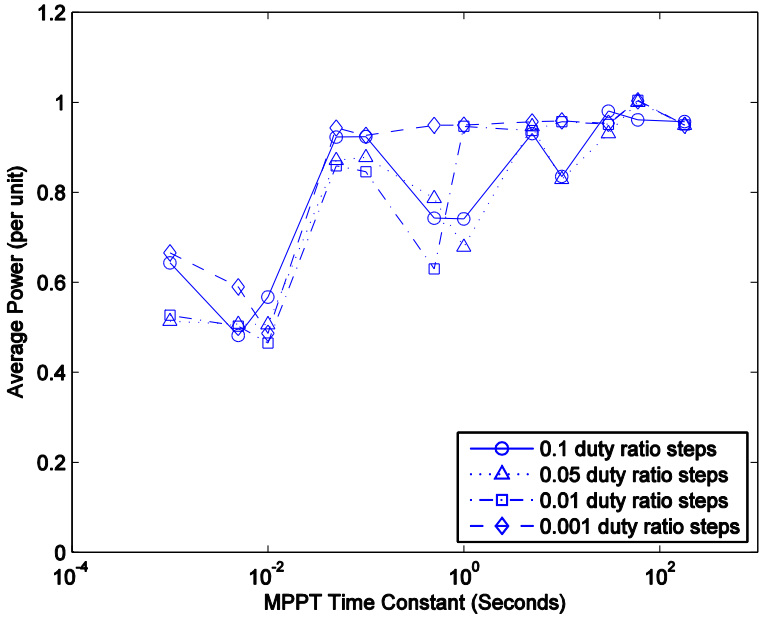

Fig. 5.4. Simulated passive rectifier results: normalized average power as a function of τ_mppt and *cStep*.

5.3.3 Experimental and Simulation Results Comparison

The experimental and simulation results compare favorably for most operating points. Direct comparisons of experimental and simulation results for each value of *cStep* are shown in Figs. 5.5-5.8. As can be seen, the overall trend of the experimental and simulation results are predominantly in agreement, with small variations most likely due to control decision differences early in the simulation propagating through to the end. An example of this can be seen in a comparison of experimental and simulation control output, shown in Fig. 5.9.

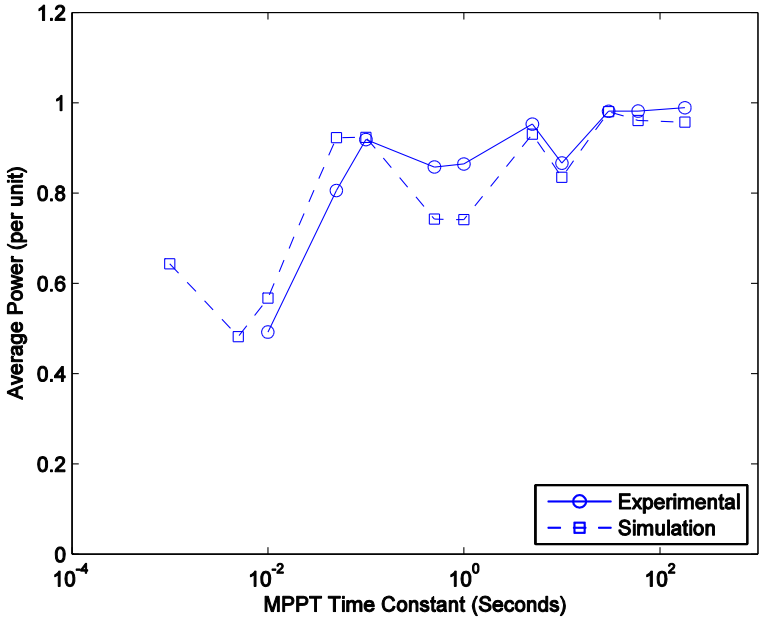

Fig. 5.5. Experimental and simulation normalized average power as a function of *τ_mppt* and *cStep* with a buck converter duty ratio step size of 0.1.

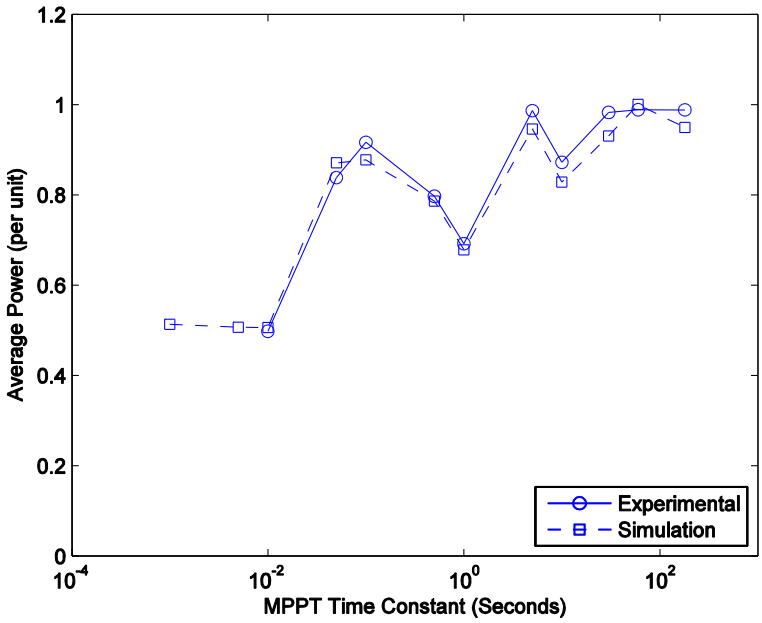

Fig. 5.6. Experimental and simulation normalized average power as a function of *τ_mppt* and *cStep* with a buck converter duty ratio step size of 0.05.

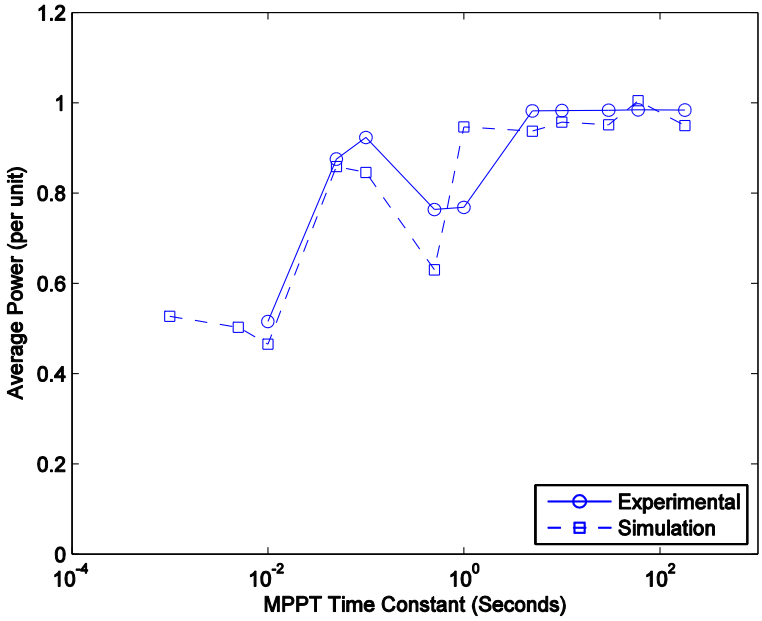

Fig. 5.7. Experimental and simulation normalized average power as a function of *τ_mppt* and *cStep* with a buck converter duty ratio step size of 0.01.

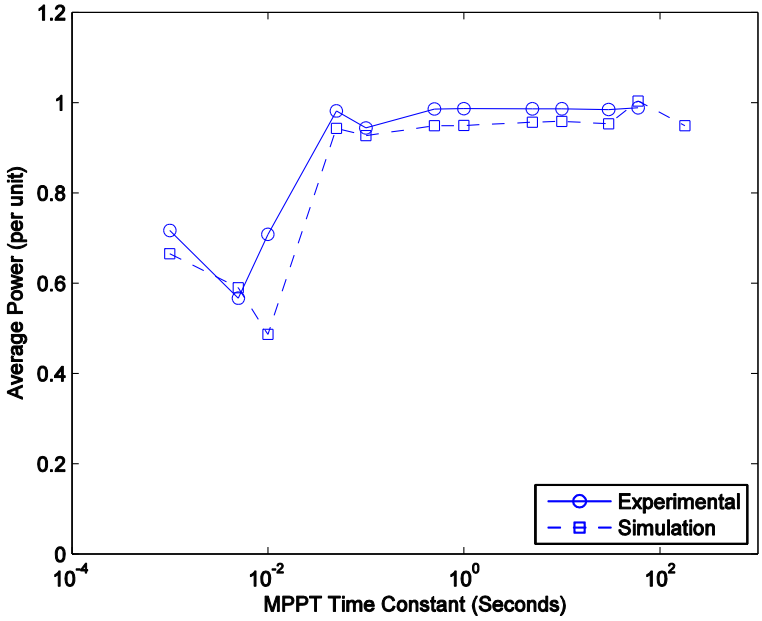

Fig. 5.8. Experimental and simulation normalized average power as a function of *τ_mppt* and *cStep* with a buck converter duty ratio step size of 0.001.

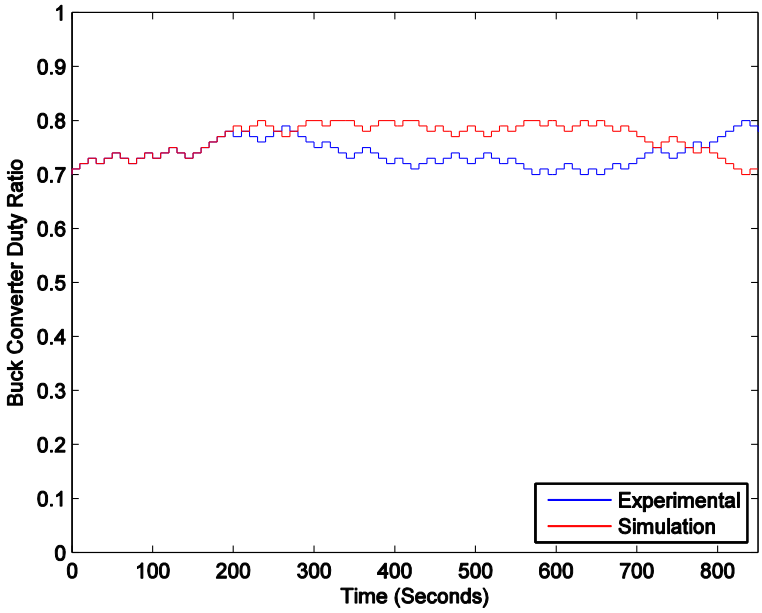

Fig. 5.9. Decision differences in experimental and simulation results; *cStep* of 0.1 and *τ_mppt* of 10 seconds.

5.4 Active Rectifier Operation

Following completion of the passive rectifier MPPT testing, the same MPPT algorithm was implemented in active rectifier mode. The active rectifier was controlled with the resistive control shown in section 4.3.2, with the MPPT control loop providing the commanded phase resistance; *cStep* now being the step size of this commanded resistance.

5.4.1 Experimental Results

In these tests, the initial commanded phase resistance was set to 10 ohms; chosen arbitrarily near the midpoint of the allowed range between 2 and 20 ohms. Due to time constraints, only four operating points were tested in active rectifier mode; MPPT time constants of 30 and 5 seconds with *cStep* of 1 ohm, and MPPT

time constants of 0.1 and 0.01 seconds with *cStep* of 0.1 ohms. The normalized average power of these operating points is shown in Fig. 5.10.

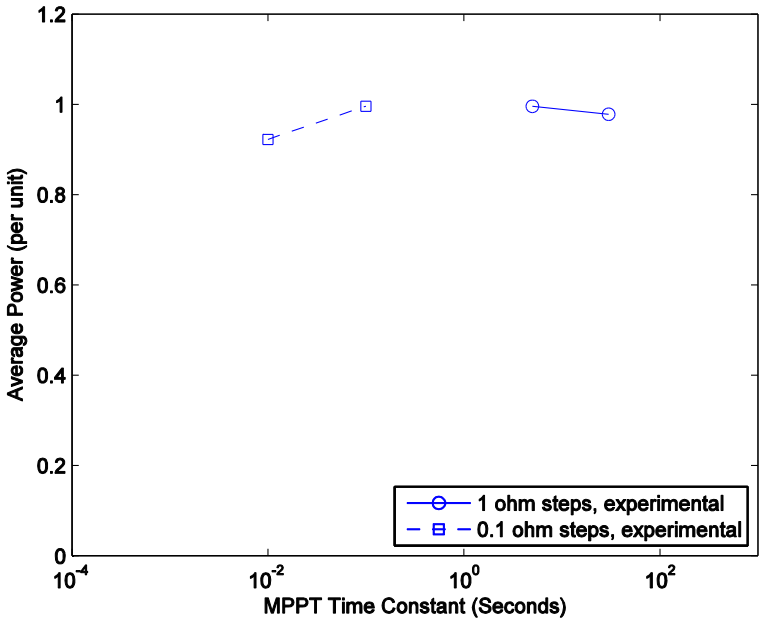

Fig. 5.10. Experimental active rectifier results: normalized average power as a function of τ_mppt and *cStep*.

5.4.2 Simulation Results

Simulation of the MPPT algorithm controlling the active rectifier was performed for validation and expansion of the experimental results. Utilizing the same initial resistance command as in the experimental testing, the MPPT control was simulated for the same *cStep* values of 1 and 0.1 ohms. Expanding upon the experimental results, each *cStep* was tested for MPPT time constants from 0.001 to 180 seconds as in the passive rectifier tests. Fig. 5.11 shows the normalized average power produced at each operating point.

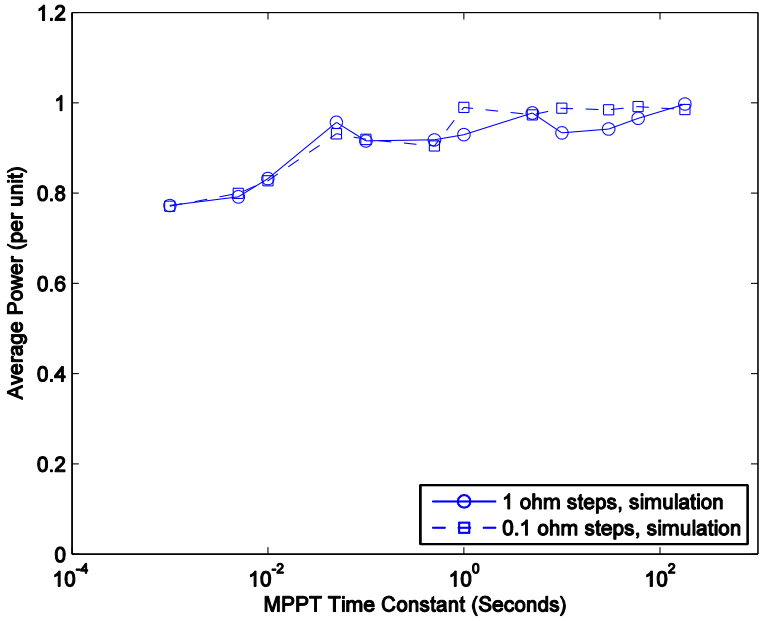

Fig. 5.11. Simulated active rectifier results: normalized average power as a function of τ_mppt and *cStep*.

5.4.3 Experimental and Simulation Results Comparison

Similar to the passive rectifier results, the active rectifier experimental and simulated results are in in close agreement. Direct comparisons of experimental and simulation results for each value of *cStep* are shown in Fig. 5.12 and Fig. 5.13.

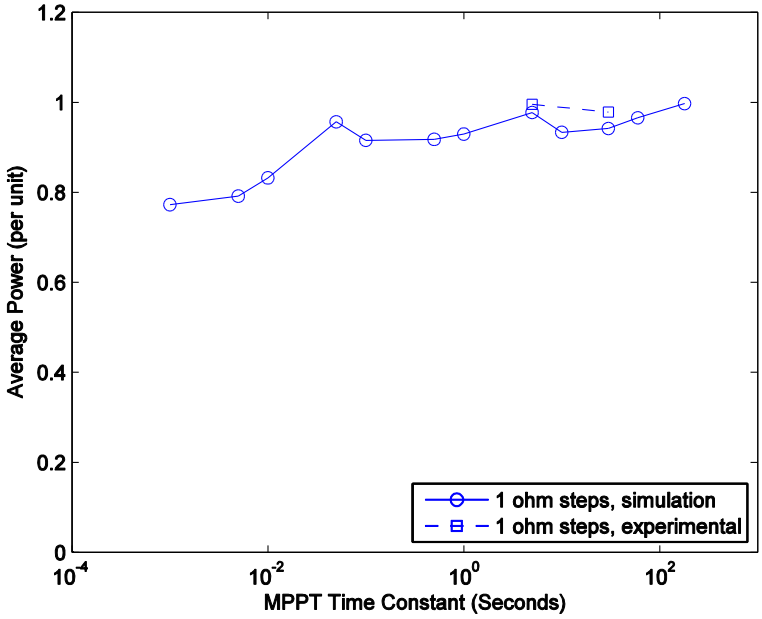

Fig. 5.12. Experimental and simulation normalized average power as a function of *τ_mppt* and *cStep* with 1 ohm step size.

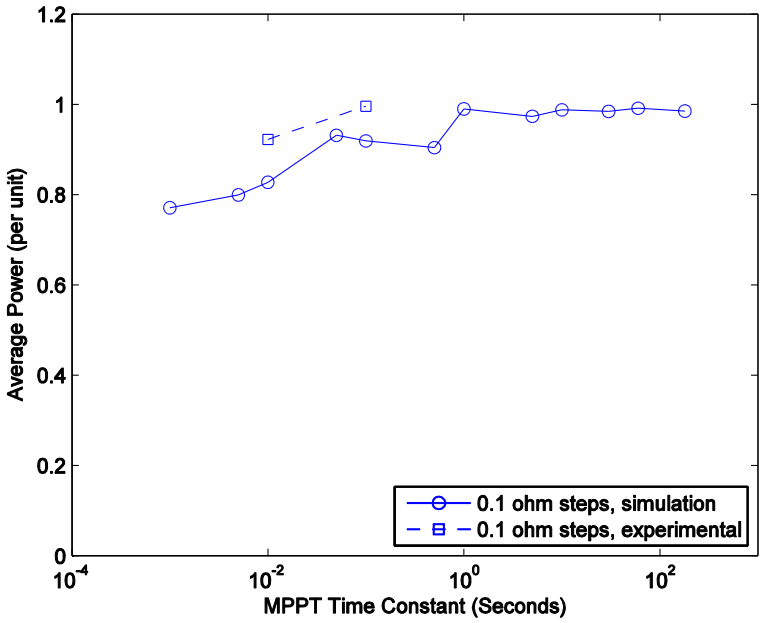

Fig. 5.13. Experimental and simulation normalized average power as a function of *τ_mppt* and *cStep* with 0.1 ohm step size.

5.5 Observations

From the results, it is shown that MPPT control can effectively be applied to ocean wave energy conversion. Both passive and active rectifier mode show promising results, indicating that MPPT may be universally applied to different control variables. There also was good correlation between experimental and simulation results, allowing further investigations to largely be performed via simulation to simplify control evaluation.

5.5.1 Passive vs. Active Rectifier Mode

The passive rectifier mode has the advantages of being simple to construct and requiring no active control. With this simplicity, however, comes lower power quality from the generator, with harmonic distortion in the generator current and no control over the displacement power factor. Active rectification requires increased complexity in both hardware and control, but has advantages of improved power factor and efficiency. An active rectifier interface also provides the ability to selectively back-drive the generator to further increase energy extraction.

In both the passive and active rectifier tests, the highest average power approached 1 per unit, showing little improvement in power production with the increased power factor of the active rectifier. It should be recognized, however, that the power production with active control could be increased with reactive loading. The simple resistive control utilized does not improve the displacement power factor of the generator current with respect to the back-EMF, leading to power reduction due to the generator's inductance.

5.5.2 MPPT Time Constant, τ_mppt

The relationship between power production and the time constant of the MPPT algorithm produces some interesting observations. What was expected is for short time constants of less than 0.1 seconds to allow the algorithm to hunt quickly,

reacting to power pulsations within a single wave. For medium time constants of 0.5 to 10 seconds, the algorithm was expected to maximize power on a wave-by-wave basis. For long time constants of greater than 30 seconds, the algorithm would tune to the overall changing sea state.

What was observed is the fastest time constants performed poorly as they react too strongly to measurement noise, resulting in rapid and directionless dithering. Time constants near one second performed poorly in the passive rectifier tests; it appears the algorithm achieves a detrimental resonance with the power waveform. With this resonance, decisions made by the MPPT algorithm are dominated by the inherent pulsating nature of the generator output with a passive rectifier. This reduction of power at time constants near one second appears to be greatly reduced in the active rectifier mode of operation, leading to the conclusion that the sinusoidal currents and improved power factor of the active rectifier mode of operation greatly reduce the mid-wave power pulsations. The consistently highest levels of performance were observed with longer time constants, greater than several wave periods. In this case, the algorithm responds slowly to the overall changes in the sea state.

In all tests, the average power produced tends to decrease with the faster MPPT time constants. A possible cause of this is excessive dithering and the ability for the control variable to venture away from its optimal value too quickly without correction. Excessive dithering with large control steps and fast MPPT time constants is demonstrated by Fig. 5.14, with the buck converter duty ratio command for a time constant of 10 ms compared with a time constant of one second. It is observed that smaller values of *cStep* perform more favorably at shorter MPPT time constants, giving an indication that it is the rate of control change, $cStep/\tau\_mppt$, that has greater influence on the stability of the control loop, rather than *cStep* and τ_mppt individually.

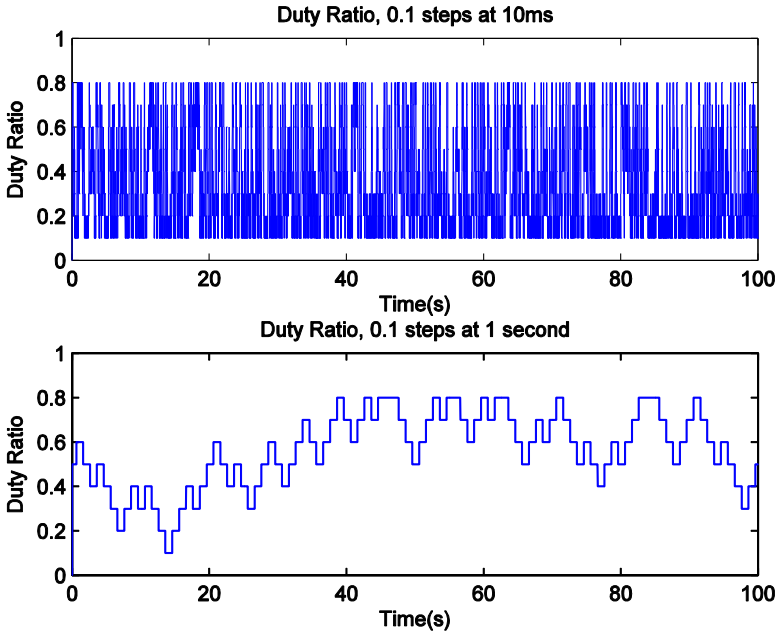

Fig. 5.14. Excessive dithering of the buck converter duty ratio.

6. TWO-VARIABLE MAXIMUM POWER POINT TRACKING

6.1 Introduction

Two-variable MPPT control was investigated as a means of improving the capabilities of MPPT control in a wave energy application. By applying MPPT to more than a single control variable, the potential exists to increase power production beyond that capable with single-variable MPPT.

Considering the L10 WEC operation in the LTB, absent hydrodynamics, optimal loading occurs through impedance matching of the generator. Previous single-variable MPPT investigations with active rectifier operation controlled only resistive loading of the generator. With two-variable MPPT, a reactive term may be added to the controlled load; the two control variables now being the effective resistance and reactance of the load emulated by the PADA. Optimal power extraction will occur when the load resistance matches the generator resistance and the load reactance cancels that of the generator.

In fixed-frequency machine applications, reactance of the machine can be canceled with properly sized power factor correction capacitors connected at the machine's terminals. With the variable-frequency output of a WEC, however, capacitance would only cancel the generator's inductance at one frequency. This is because reactance of inductors is proportional to frequency, whereas reactance of capacitors is inversely proportional to frequency. Since the phase of a generator can be represented by a series resistance and inductance, the emulated load by the PADA for maximum power extraction is a series resistance and negative inductance.

6.2 Control Implementation

Several methods of implementing two-variable MPPT have been investigated and can be grouped into two categories; two-variable independent and

two-dimensional. These investigations include one variant of two-variable independent MPPT control and three variants of two-dimensional MPPT control.

For the two-variable MPPT investigations, the method of quantifying performance for control decisions was altered. In the single-variable MPPT investigations, a 2nd-order Butterworth filter with a corner frequency of 1/ τ_mppt performed the power-averaging. To make the measurement more discrete between the intervals, a resettable integrator was placed on the instantaneous power to sum the total energy during each period of τ_mppt. The control now compares this total energy over previous periods of τ_mppt, as opposed to the average power over each period.

6.2.1 Degrees of Freedom

The degrees of freedom in two-variable MPPT are the same as with single-variable MPPT; the control variable step size, *cStep*, and the MPPT time constant, τ_mppt. A change has been made to the implementation of *cStep* to apply it universally to both control variables. In single-variable MPPT, *cStep* was directly the commanded step size of the control variable. For application to two control variables, the commanded step size is now the product of *cStep* and the control variable's optimal value. For instance, in the L10 model, the phase resistance is 3.84 ohms and phase inductance is 0.120 henries. Optimal values of the load emulated by the PADA for maximum power extraction would be a resistance of 3.84 ohms and negative inductance of 0.120 henries. With a *cStep* value of 0.1, the control variable step size for resistance and negative inductance would be ten percent of the optimal values, or 0.384 ohms and 0.012 henries respectively.

6.2.2 Control Implementation Objectives

The two-variable MPPT algorithms were investigated to verify the effectiveness of applying MPPT to multiple control variables in one system. The

impact of *cStep* and *τ_mppt* on performance of the MPPT algorithms was evaluated to determine their optimal scales for application in wave energy. Comparison of the different two-variable MPPT control algorithms is presented to quantify performance differences between two-variable and two-dimensional control and to determine the optimal algorithm for wave energy applications.

6.3 Two-Variable Independent MPPT

Two-variable independent MPPT is built upon the MPPT control algorithm described in section 5.2, with separate control loops applied to two different control variables. With the L10, this maintains the original control loop on the resistance command and adds a second control loop for negative inductance. Separation between the control loops is realized by offsetting the loop timing and energy summing by a half period of *τ_mppt*. This separation allows each control loop to see the full effect of its previous control change while minimizing influence of the other control loop.

Fig. 6.1 shows the implementation of the two-variable independent control in MATLAB Simulink. Each MPPT control loop is contained within an enabled subsystem, eliminating the rate transition blocks previously implemented. Each block is triggered by an edge of the pulse generator at *τ_mppt*. This pulse is inverted for the second loop, to offset the rising edge trigger by *τ_mppt/2*. The same trigger signals are used to reset the integrators summing energy and a memory block holds the energy value when the integrator is reset. Where previously the commanded voltage was the product of the input current to the PADA and the commanded resistance, the commanded voltage is now the product of the input currents and the complex load impedance; implementation shown in Fig. 6.2. An example of the control signals with this control period offset is shown in Fig. 6.3.

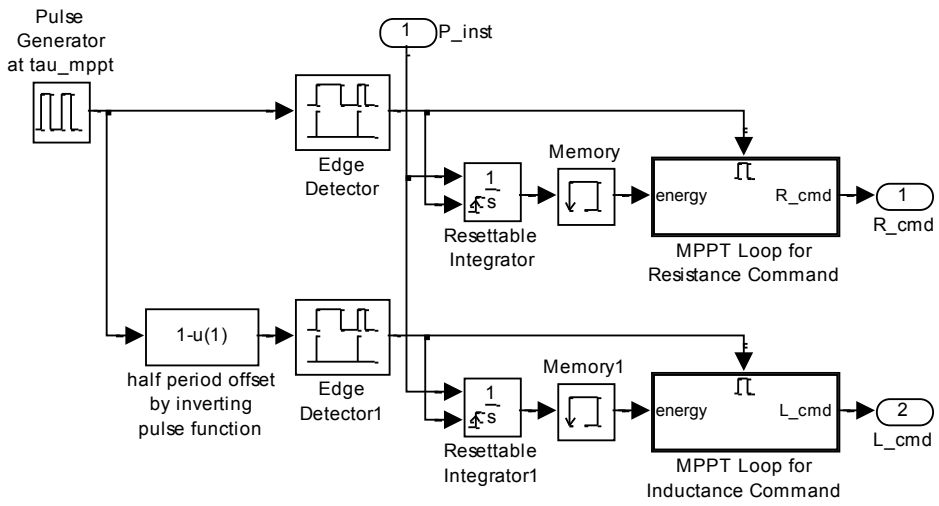

Fig. 6.1. MATLAB Simulink model of two-variable independent control.

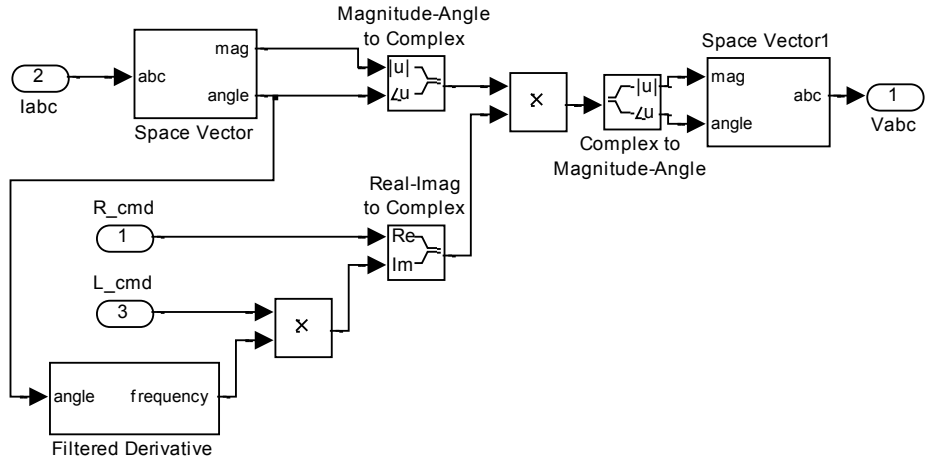

Fig. 6.2. Implementation of complex load impedance command.

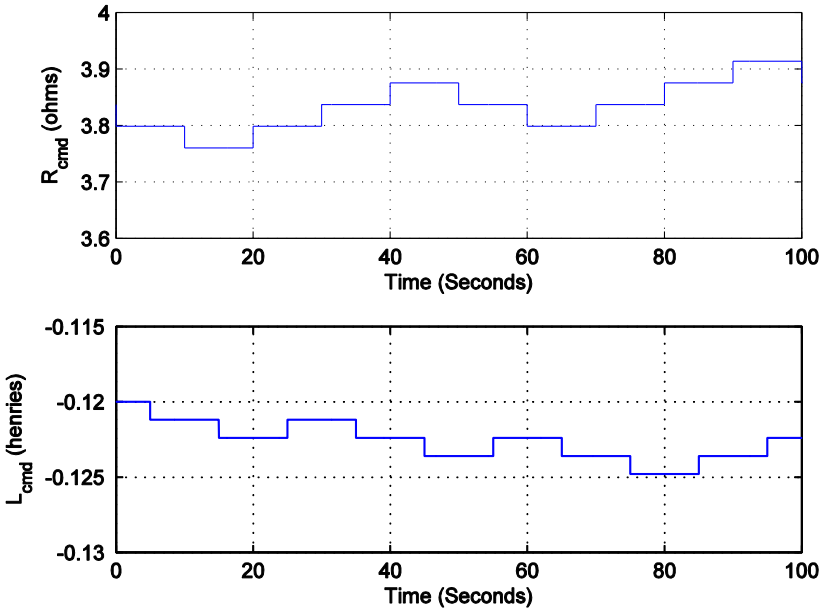

Fig. 6.3. Control signals showing timing offset in MPPT loops.

6.3.1 Simulation Results

The two-variable independent MPPT control was simulated utilizing the same model and compensated position profile used in the single-variable simulations, with implementation of the new control blocks presented in Figs. 6.1 and 6.2. Values tested for *cStep* were 0.1, 0.05, 0.01, 0.005 and 0.001. For each value of *cStep*, τ_mppt was varied from 0.001 to 60 seconds. Fig. 6.4 shows the average power produced at each operating point, normalized in the same means as the single-variable MPPT tests.

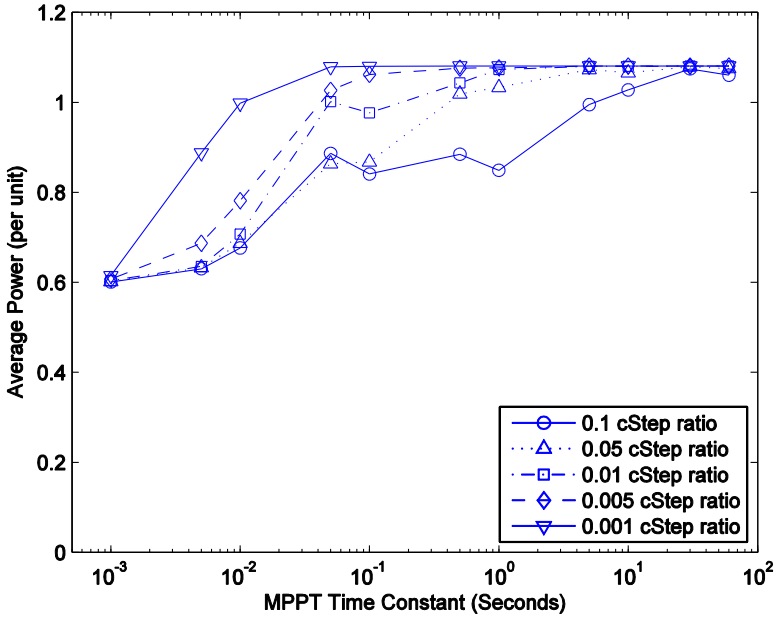

Fig. 6.4. Two-variable independent MPPT simulation results: normalized average power as a function of τ_mppt and *cStep*.

As shown, the maximum power has increased by approximately ten percent, compared with the single-variable results, due to the increased efficiency in the generator with reactive loading improving the power factor. The only data set showing the decreased power near a MPPT time constant of one second is the case with the largest control step. This indicates again that the power decrease observed in the single-variable passive rectifier tests was attributed to the pulsed power in passive rectifier mode. Also noted is the strong correlation between average power and the ratio between *cStep* and τ_mppt that was observed in the single-variable MP0PT results. This ratio will be denoted as the control rate, *cRate*, as in equation (6.1), and is the rate at which the control algorithm can change the control variable.

$$cRate = {cStep}/{\tau\_mppt} \tag{6.1}$$

The relationship between average power and the control rate is shown in Fig. 6.5 with all points from the two-variable independent MPPT simulation results from Fig. 6.4 plotted by their control rate. As shown, there is a strong relationship between average power and the MPPT control rate, *cRate*.

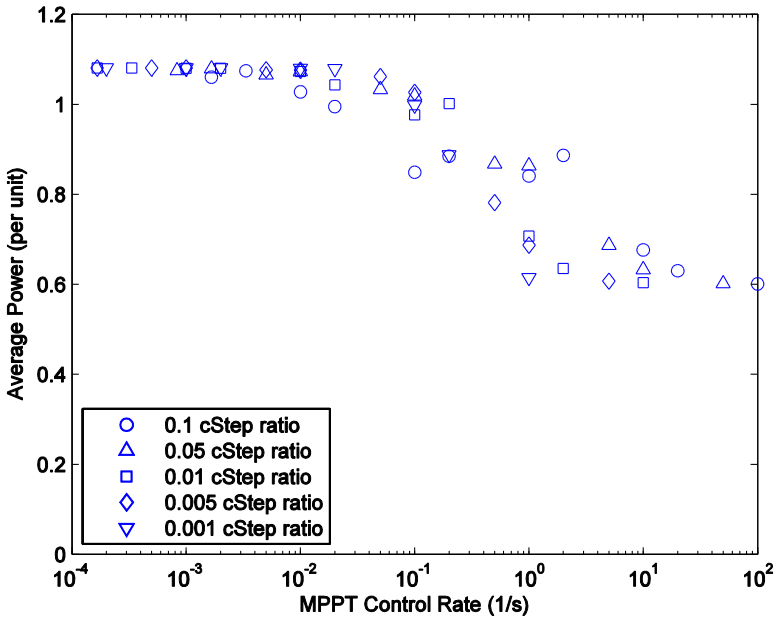

Fig. 6.5. Two-variable independent MPPT simulation results: normalized average power as a function *cRate*.

To quantify these results for comparison with experimental results and other control algorithms, it was desired to fit a curve to the data. A least-squares fit was performed on the data in Fig 6.5 using the equation for a Butterworth filter, as the data trend resembles the frequency response of a low-pass filter. The gain was normalized between the maximum and minimum average power levels in the dataset, resulting in equation (6.2) for average power.

$$P_{avg} = P_{min} + \frac{(P_{max} - P_{min})}{\sqrt{1 + \left(\omega/\omega_c\right)^{2n}}} \tag{6.2}$$

Here, the Butterworth filter fitting the data has corner frequency ω_c and order n. The gain of the filter is normalized between the maximum and minimum average power levels in the dataset, P_{max} *and* P_{min} respectively, resulting in the curve for average power P_{avg} by frequency ω. Fig. 6.6 shows the dataset plotted with the least-squares fit with equation (6.2). The optimal values for ω_c and n were obtained iteratively in MATLAB, resulting in a corner frequency of 0.156 radians per second and a filter order of 0.572.

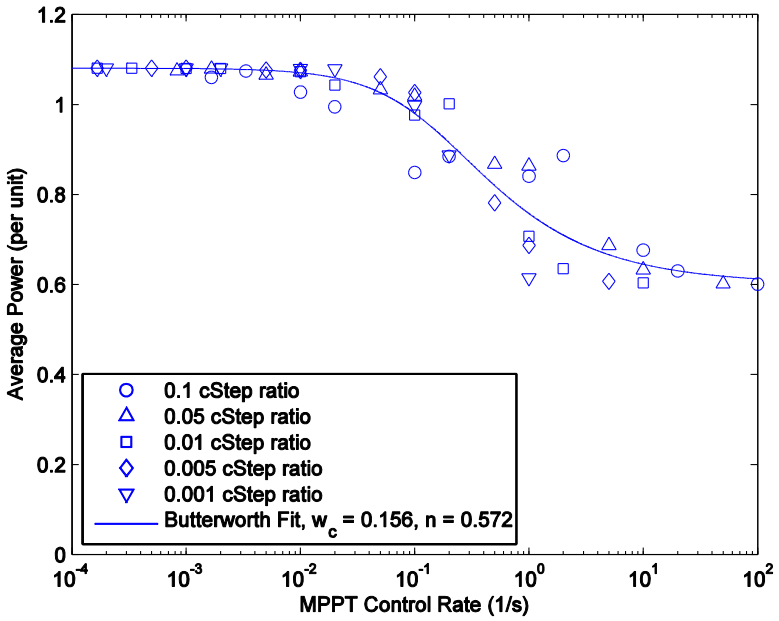

Fig. 6.6. Two-variable independent MPPT simulation results: normalized average power as a function *cRate* with Butterworth least-squares fit.

6.3.2 Experimental Results

Experimental results were obtained in the same manner as with the single-variable MPPT tests. For verification purposes, only a *cStep* of 0.01 was tested with τ_mppt values of 0.001 to 10 seconds. It should be noted that the generator winding configuration in the experimental setup had changed since the single-variable MPPT tests were performed. A winding fault had caused unbalance in the output voltage. Since the damaged coil could not be accessed to repair, it was removed from the phase circuit by bypassing it at the coil junction block. To balance the output voltage, one coil was removed from each of the other two phases. Removing one of four windings per phase resulted in current and voltage being reduced by approximately twenty five percent each. For comparison purposes, the experimental results have been normalized by their new maximum value. However, this normalization does not affect the relationship between average power and control rate, which is the primary concern in evaluating and validating the MPPT results. The normalized experimental average power by control rate *cRate* along with the least-squares fit Butterworth curve from simulation is shown in Fig. 6.7. The experimental results match the shape of the simulation least-squares-fit well, showing agreement in the relationship between average power and control rate.

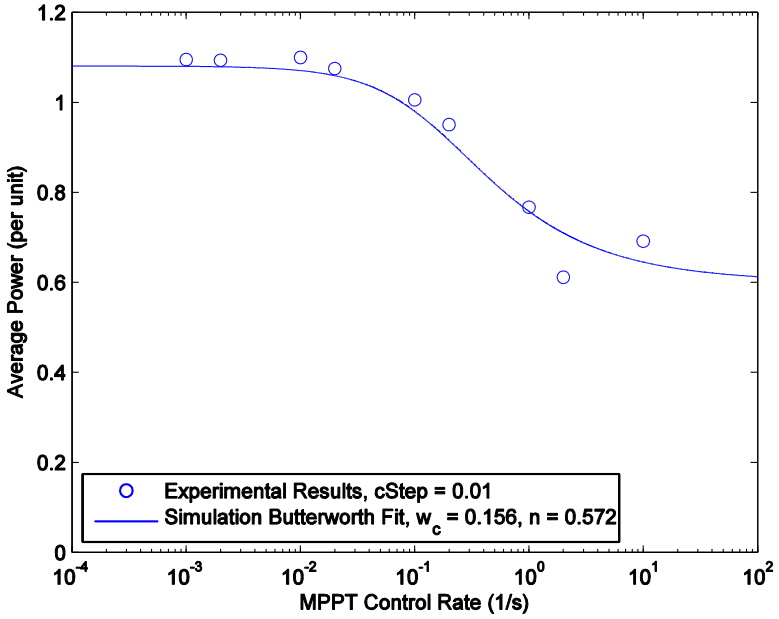

Fig. 6.7. Two-variable independent MPPT experimental results: normalized average power as a function of *cRate* with simulation Butterworth least-squares fit.

6.4 Two-Dimensional Four-Step MPPT

Two-dimensional MPPT is an application of "perturb and observe" MPPT in which the control movements are made on a two-dimensional plane rather than one-dimensionally on a single control axis. In this application, the two axes of the plane are the resistance and negative inductance of the emulated load by the PADA. The two-dimensional four-step MPPT variant operates on the same concept as the previous algorithm; it makes control changes and tracks how they affect the generator's energy production. The difference with the four-step variant, however, is that it tests four operating points around the current operating point before comparing the energy during each period. After completing the four test steps, the algorithm moves from the original position to the operating point of the four which had the highest energy production.

A diagram showing this process is shown in Fig. 6.8. Step 1 increases the resistance, step 2 returns the resistance and increases the negative inductance, step 3 returns the inductance and decreases the resistance, and step 4 returns the resistance and decreases the negative inductance. Starting at point 0 in Trial 1, the algorithm steps to operating points 1, 2, 3, and 4, each for a duration of τ_mppt. At the end of the period at point 4, the algorithm compares the total energy from each point and in the Decision state moves to point 3; the highest energy operating point. Point 3 now becomes point 0 and after one period of τ_mppt, the trial starts over as shown in Trial 2. Following this pattern, after Trial 2 the algorithm will move to point 2. With each step, 0-4 lasting for one period of τ_mppt, the algorithm takes five periods of τ_mppt to make a permanent control change. In MATLAB Simulink, this algorithm is performed in a Level-2 M-File S-Function, the code of which can be found in Appendix A.

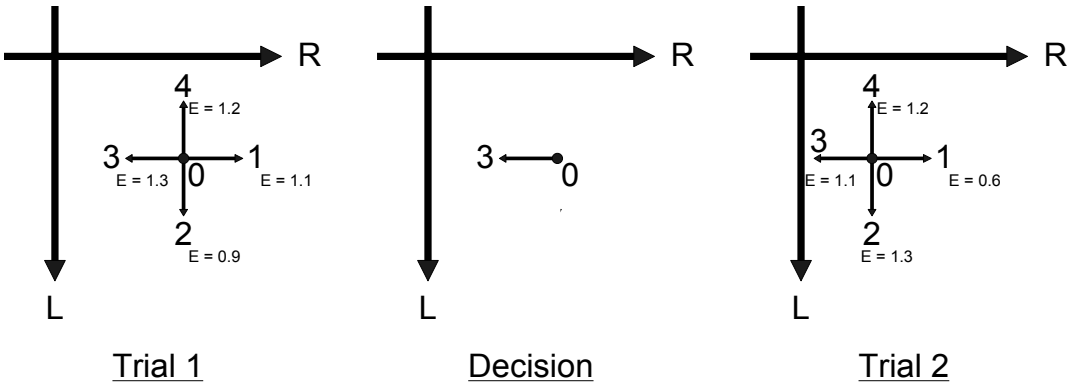

Fig. 6.8. Operation of the two-dimensional four-step MPPT algorithm.

6.4.1 Simulation Results

The two-dimensional four-step MPPT control was simulated for *cStep* values of 0.1, 0.05, 0.01, 0.005, and 0.001. For each value of *cStep*, τ_mppt was

varied from 0.001 to 60 seconds. Fig. 6.9 shows the normalized average power produced at each operating point.

As shown, the highest power cases approach the same magnitude as the two-variable independent MPPT control. At MPPT time constants of one second and greater, this algorithm performs noticeably better than the independent control, especially with the largest control step size. At time constants of less than one second, however, the average power appears to drop much more rapidly in all cases. This was not expected, as the ability to perform a trial in all four directions before committing to a change intuitively would result in fewer incorrect decisions. To understand this behavior, the control signals for resistance and inductance of a low power case ($cStep$ = 0.01, τ_mppt = 0.01) are examined, shown in Fig. 6.10. As this figure shows, both control signals climb to their upper limit quickly, indicating the first and last step of the algorithm are being heavily favored. The conclusion is that the faster time constants, combined with the long duration of the overall algorithm ($5 \times \tau\_mppt$), results in the decision favoring the first and last step due to the input power ramping up and down.

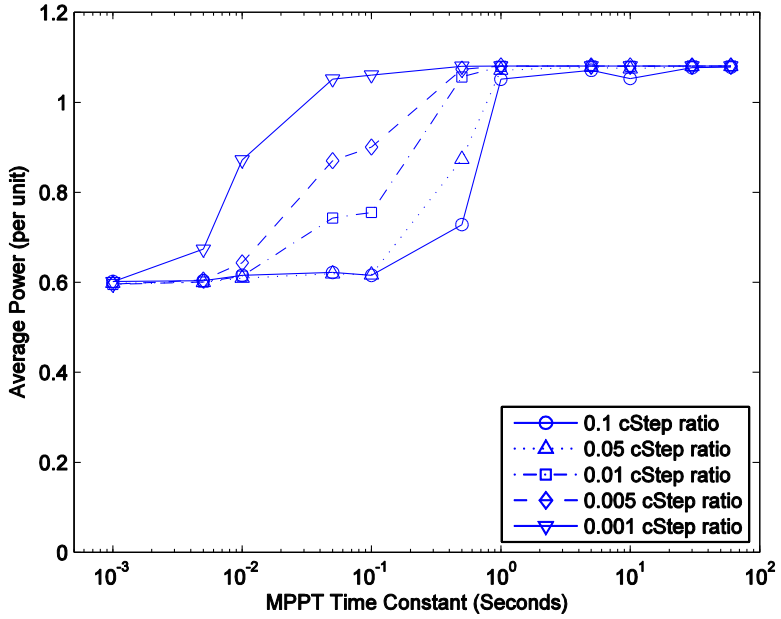

Fig. 6.9. Two-dimensional four-step MPPT simulation results: normalized average power as a function of *τ_mppt* and *cStep*.

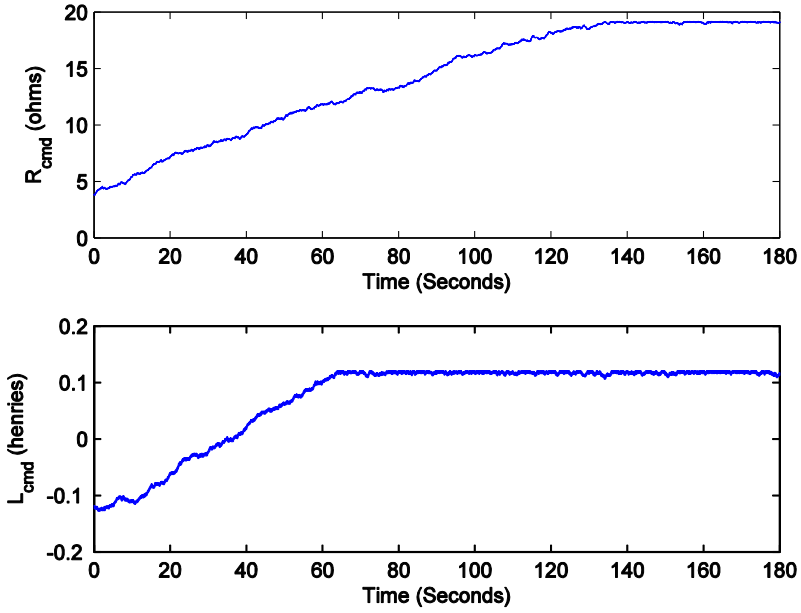

Fig. 6.10. Control signals for two-dimensional four-step MPPT; *cStep* of 0.01 and *τ_mppt* of 0.01.

To quantify these results, as with the two-variable independent MPPT, the average power for each simulation case is again plotted by the MPPT control rate, *cRate*. Since this algorithm takes five periods of τ_mppt to make a permanent control change, the control rate is given as in equation (6.3).

$$cRate = {cStep}/{(5 \times \tau\_mppt)} \tag{6.3}$$

The relationship between average power and the control rate is shown in Fig. 6.11 along with the least-squares Butterworth curve fit from equation (6.2) for this algorithm. As shown, the average power drops much more sharply than the two-variable independent MPPT control, at a corner frequency of 0.014 radians per second with a higher order of 1.175. Comparing with the two-variable independent MPPT control, the two-dimensional four-step MPPT suffers greatly due to taking five periods of τ_mppt to make a permanent control change; with the corner frequency being an order of magnitude less and having a much sharper drop in average power.

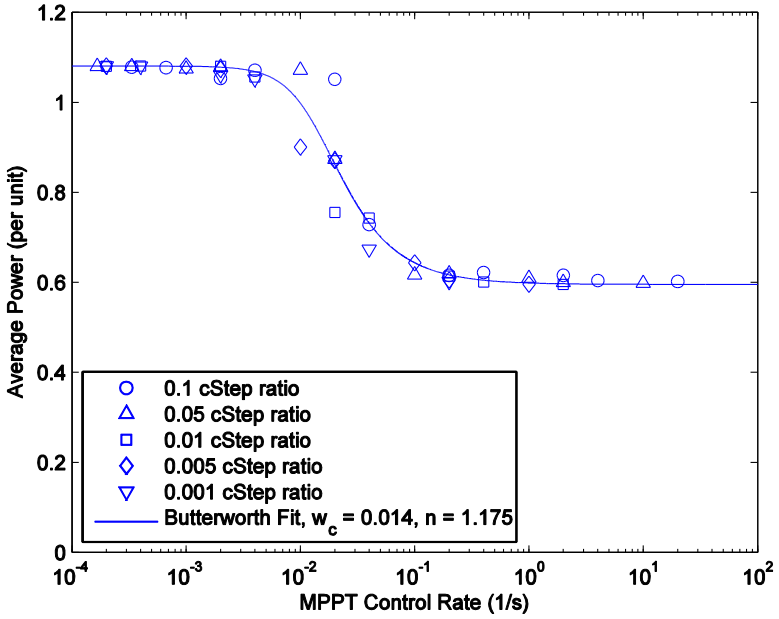

Fig. 6.11. Two-dimensional four-step MPPT simulation results: normalized average power as a function *cRate* with Butterworth least-squares fit.

6.4.2 Experimental Results

Experimental results were obtained for a *cStep* of 0.1 with τ_*mppt* values of 0.01 to 60 seconds. The normalized experimental average power by *cRate,* along with the least-squares fit Butterworth curve from simulation is shown in Fig. 6.12. The experimental results match the shape of the simulation least-squares-fit well. The only outlying point occurs near the corner frequency, but as shown in Fig. 6.13, the experimental results match simulation well.

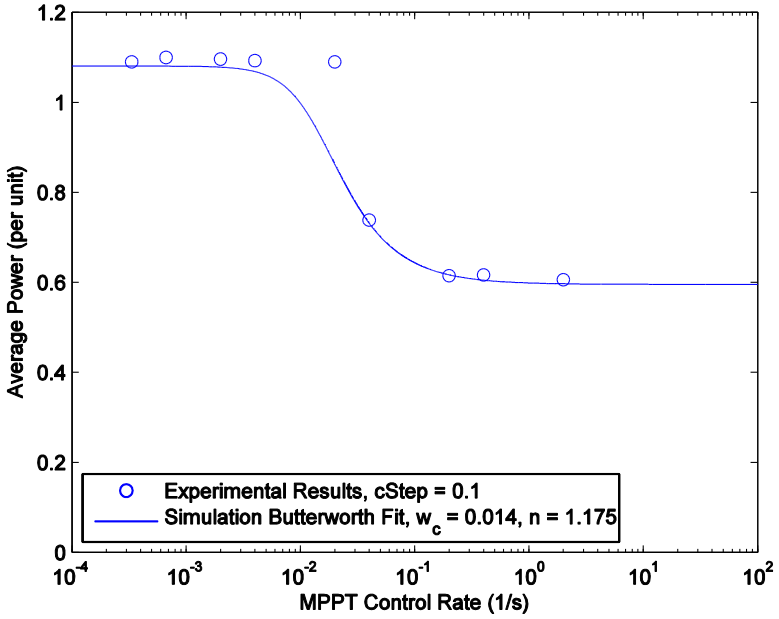

Fig. 6.12. Two-dimensional four-step MPPT experimental results: normalized average power as a function of *cRate* with simulation Butterworth least-squares fit.

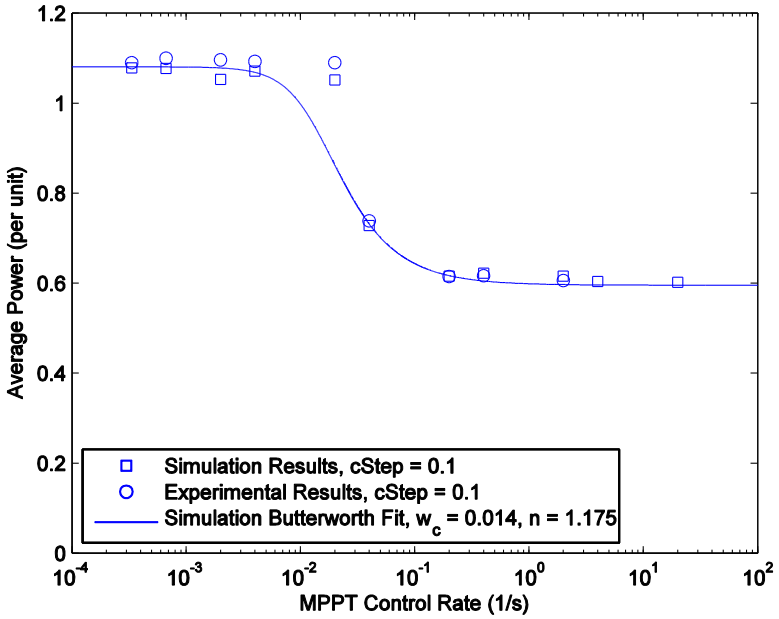

Fig. 6.13. Two-dimensional four-step MPPT experimental and simulation results for *cStep* of 0.1: normalized average power as a function of *cRate* with simulation Butterworth least-squares fit.

6.5 Two-Dimensional Two-Step MPPT

With the observation that the two-dimensional four-step MPPT algorithm performed poorly at faster control rates, a two-step variant was investigated to reduce the number of τ_mppt periods required to make a permanent control change. Instead of testing the operation in all four directions, this variant tests the operation in only two directions. The control steps the resistance command in one direction, then the inductance command in one direction and compares these with the original operating point. By assuming the opposite direction in both the resistance and inductance commands will have the opposite effect on power, the algorithm has knowledge of all four operating points and moves each variable in the direction that should increase power. An individual direction history is kept for each control variable.

A diagram showing this operation is given in Fig. 6.14. Starting with Trial 1 at position 0, the algorithm waits one period of τ_mppt, and then moves to position 1 for one period, and on to position 2 for one period. At this time the energy of positions 1 and 2 is compared with that from position 0. Since both steps result in an increase in energy, both changes are kept and Decision 1 moves from position 0 diagonally to keep the changes from both 1 and 2. Now, since the previous steps both increased energy, the steps in Trial 2 are in the same directions. This time, step 1 decreased the energy and step 2 increased the energy. Decision 3 moves in the opposite direction of step 1 and in the direction of step 2. Trial 3 now steps both variables in the direction of the last change with both causing a decrease in energy. The result is a move in the opposite direction for both variables as shown in Decision 3. As shown, the algorithm always makes trial steps in only the R or L direction, but always makes the permanent control change diagonally. With each step, 0-2, lasting for one period of τ_mppt, the algorithm takes three periods of τ_mppt to make a permanent control change. In MATLAB Simulink, this algorithm

is performed in a Level-2 M-File S-Function, the code of which can be found in Appendix B.

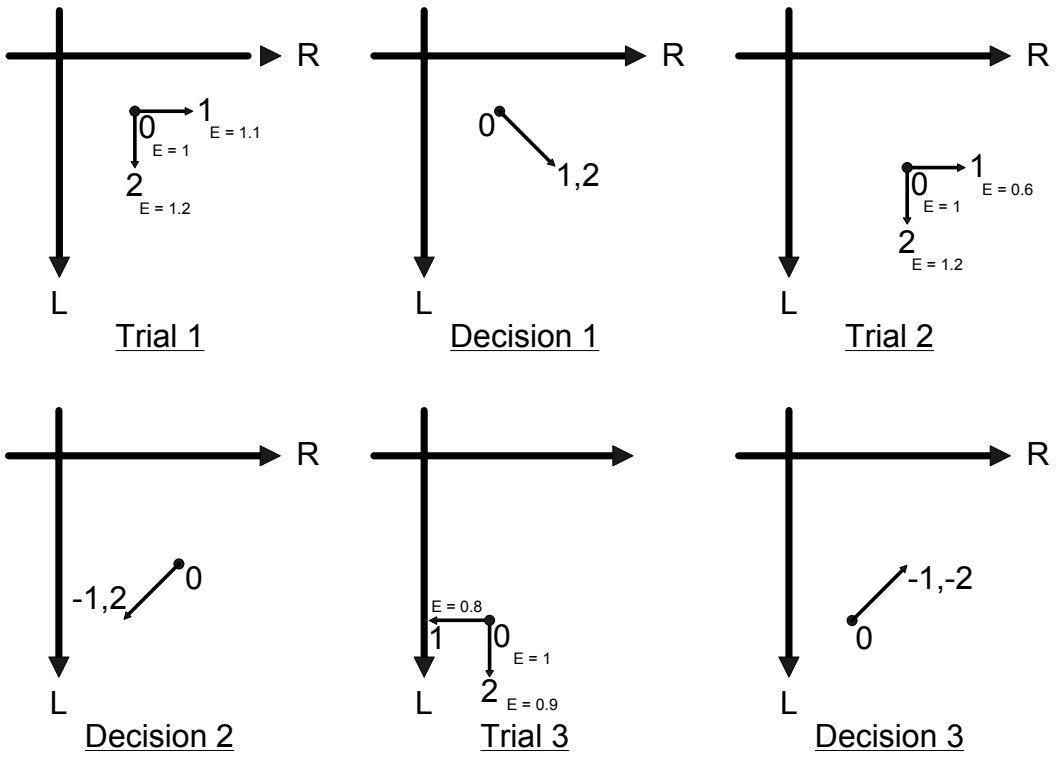

Fig. 6.14. Operation of the two-dimensional two-step MPPT algorithm.

6.5.1 Simulation Results

The two-dimensional two-step MPPT control was simulated for *cStep* values of 0.1, 0.05, 0.01, 0.005, and 0.001. For each value of *cStep*, τ_mppt was varied from 0.001 to 60 seconds. Fig. 6.15 shows the normalized average power produced at each operating point.

The highest power cases approach the same magnitude as the two-variable independent MPPT control and the two-dimensional four-step MPPT control. For the faster MPPT time constants, this algorithm performs noticeably better than both

of the previous two-variable control algorithms, with a very slow drop off in average power. Interestingly, the poor performance at τ_mppt of one second is observed again with the largest *cStep* of 0.1, indicating there is still a resonance occurring with the power waveform and that the larger control step sizes magnify the effect.

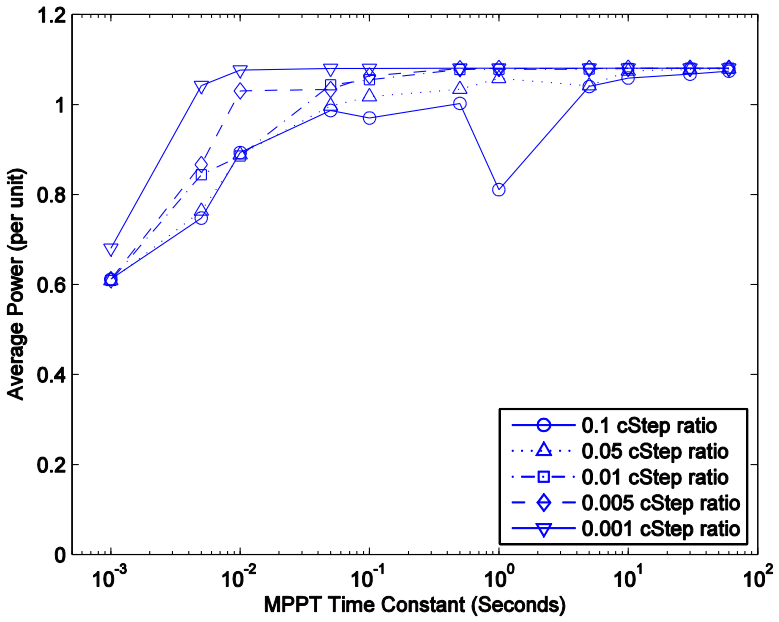

Fig. 6.15. Two-dimensional two-step MPPT simulation results: normalized average power as a function of τ_mppt and *cStep*.

To quantify these results, the average power for each simulation case is again plotted by the MPPT control rate, *cRate*. Since this algorithm takes three periods of τ_mppt to make a permanent control change, the control rate is given as in equation (6.4).

$$cRate = {cStep}/{(3 \times \tau\_mppt)} \tag{6.4}$$

The relationship between average power and the control rate is shown in Fig. 6.16 along with the least-squares Butterworth curve fit from equation (6.2) for this algorithm. As shown, the average power drops off at a much lower rate than in the four-step algorithm, indicating an improvement by taking fewer steps to make a permanent control change. The corner frequency of 0.210 radians per second is fifteen times that of the four-step control, showing the two-step variant is stable at significantly faster control rates. This is also a 35 percent improvement over the corner frequency of the individual control, even though the two-step takes three *τ_mppt* periods to make a permanent control change and the individual control only takes one period. This shows that the two-step control is taking longer to implement a permanent change, but makes fewer decision mistakes.

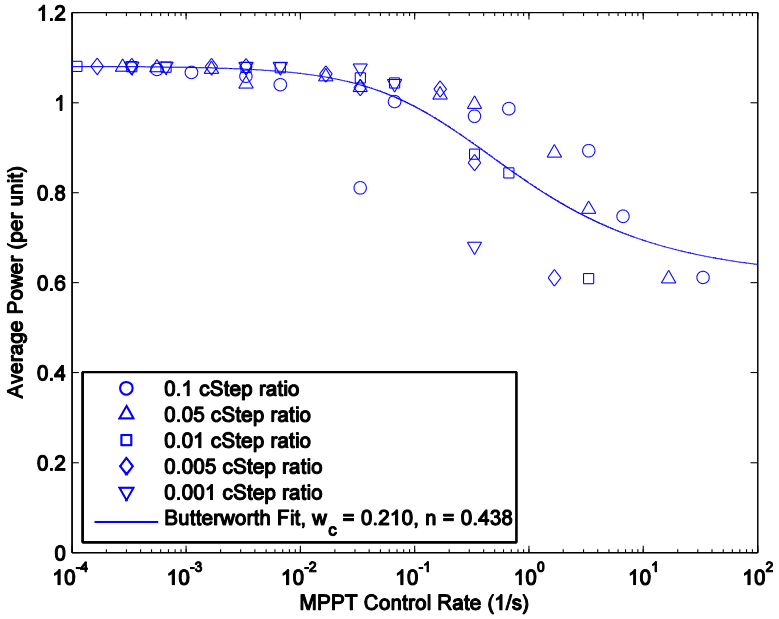

Fig. 6.16. Two-dimensional two-step MPPT simulation results: normalized average power as a function *cRate* with Butterworth least-squares fit.

6.5.2 Experimental Results

Experimental results were obtained for a *cStep* of 0.01 with τ_*mppt* values of 0.001 to 10 seconds. The normalized experimental average power by *cRate,* along with the least-squares fit Butterworth curve from simulation is shown in Fig. 6.17. The experimental results do not appear to match the least-squares Butterworth curve fit from simulation as well as with the previous control algorithms. When comparing the experimental results in Fig. 6.17 with the simulation results from the same value of *cStep*, most points match well; the exception being the second fastest point. This indicates there were different decisions made between the experimental and simulation results. This is to be expected as the system simulation is not an exact representation of the experimental system. Experimental and simulation results, plotted with the least-squares Butterworth curve fit, are shown in Fig. 6.18 for *cStep* of 0.01.

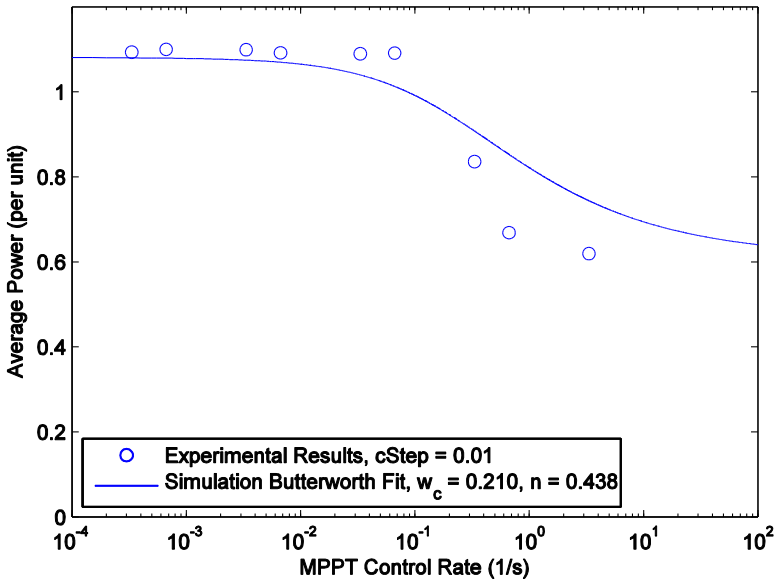

Fig. 6.17. Two-dimensional two-step MPPT experimental results: normalized average power as a function of *cRate* with simulation Butterworth least-squares fit.

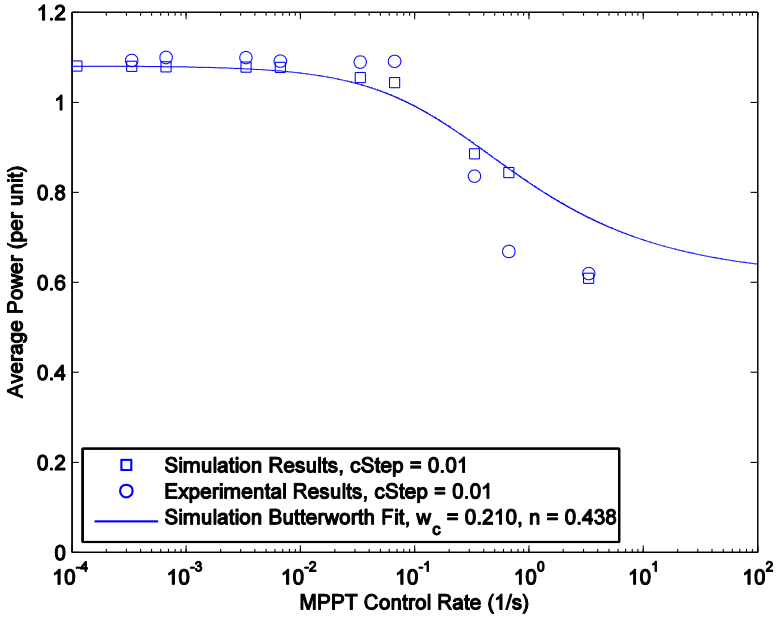

Fig. 6.18. Two-dimensional two-step MPPT experimental and simulation results for *cStep* of 0.01: normalized average power as a function of *cRate* with simulation Butterworth least-squares fit.

6.6 Two-Dimensional Two-Step Radial MPPT

The two-dimensional two-step radial MPPT is a variation on the two-step algorithm previously implemented. The two-step radial variant is identical to the two-step algorithm with the exception of the control step following two trial steps. Instead of stepping diagonally, with a full step size for each variable, the control step is placed on the arc formed by the test steps. The position on this arc is determined by the ratio of energy during steps 1 and 2, weighting the control step more heavily in the direction producing more energy. This effectively weights the A diagram showing this operation is given in Fig. 6.19. As shown, the trial steps are the same as with the two-step variant, with the decision steps showing the change in control.

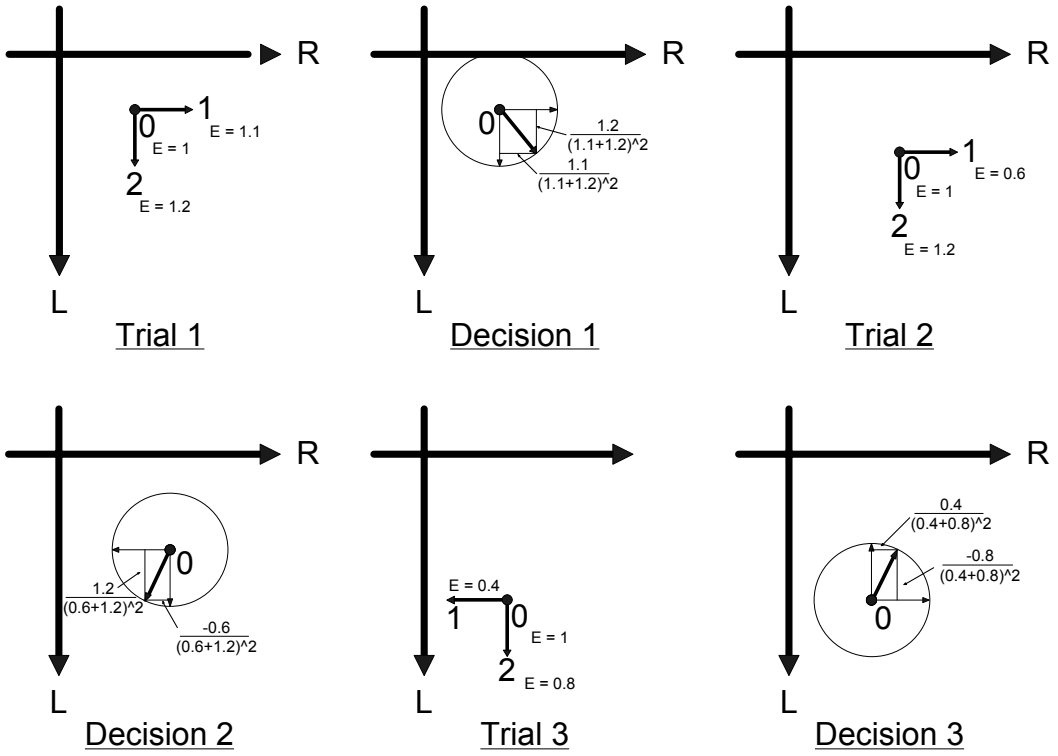

Fig. 6.19. Operation of the two-dimensional two-step MPPT algorithm.

Similar to the two-dimensional two-variable MPPT control, this control loop takes three periods of τ_mppt to make a permanent control change. In MATLAB Simulink, this algorithm is performed in a Level-2 M-File S-Function, the code of which can be found in Appendix C.

6.6.1 Simulation Results

The two-dimensional two-step radial MPPT control was simulated for *cStep* values of 0.1, 0.05, 0.01, 0.005, and 0.001. For each value of *cStep*, τ_*mppt* was varied from 0.001 to 60 seconds. Fig. 6.20 shows the normalized average power produced at each operating point.

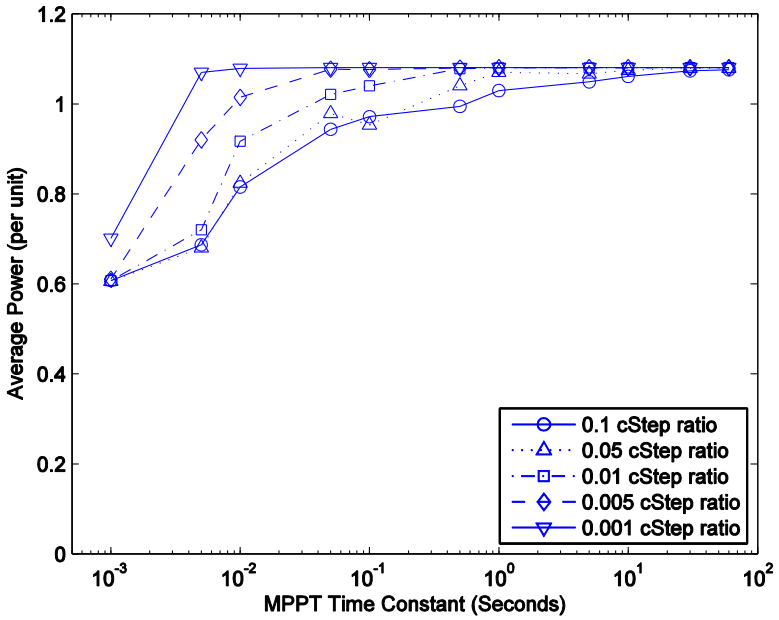

Fig. 6.20. Two-dimensional two-step radial MPPT simulation results: normalized average power as a function of *τ_mppt* and *cStep*.

This control appears to have the highest average output power across the range of τ_*mppt* and does not exhibit the reduction in average power near τ_*mppt* of one second as the two-step and individual algorithms showed. The highest power cases approach the same magnitude as the previous two-variable MPPT control.

The average power for each simulation case is again plotted by the MPPT control rate, *cRate*. Since this algorithm takes three periods of τ_mppt to make a permanent control change, the control rate was given previously in equation (6.4). The relationship between average power and the control rate is shown in Fig. 6.21 along with the least-squares Butterworth curve fit from equation (6.2) for this algorithm. As shown, the average power plotted by *cRate* is very similar to that of the previous two-step algorithm. The corner frequency of 0.225 radians per second is the highest corner frequency of the algorithms tested and 0.015 radians per second higher than the two-step control. The order, however, is almost 50% higher than that of the previous two-step control. The improvement over the two-variable independent MPPT control reiterates that the two-step control is taking longer to implement a permanent change, but makes fewer decision mistakes.

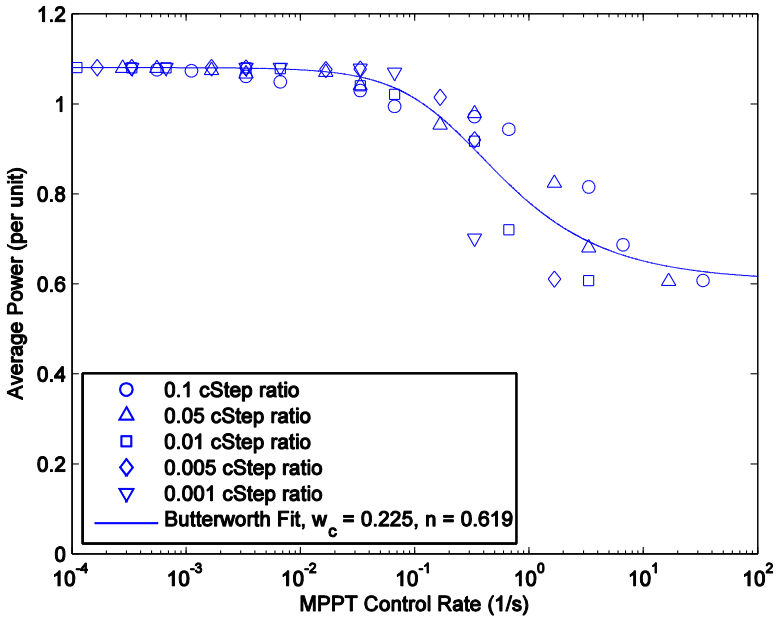

Fig. 6.21. Two-dimensional two-step radial MPPT simulation results: normalized average power as a function *cRate* with Butterworth least-squares fit.

6.6.2 Experimental Results

Experimental results were obtained for a *cStep* of 0.01 with τ_*mppt* values of 0.001 to 10 seconds. The normalized experimental average power by *cRate,* along with the least-squares fit Butterworth curve from simulation is shown in Fig. 6.22.

The experimental results compare with the least-squares Butterworth fit very similarly as they did in the previous two-step algorithm, but with slightly less variation. This is compared with the simulation results with the same value of *cStep* in Fig. 6.23, which shows good correlation between the experimental and simulation results.

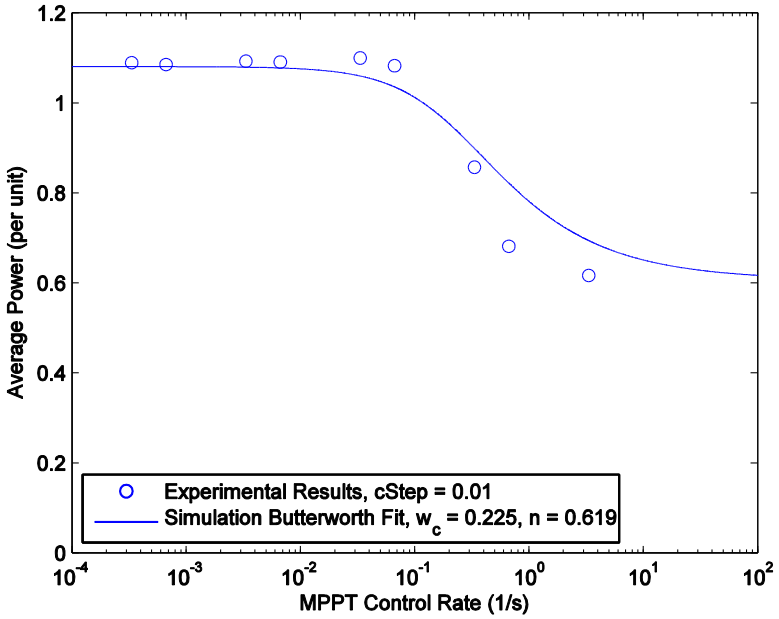

Fig. 6.22. Two-dimensional two-step radial MPPT experimental results: normalized average power as a function of *cRate* with simulation Butterworth least-squares fit.

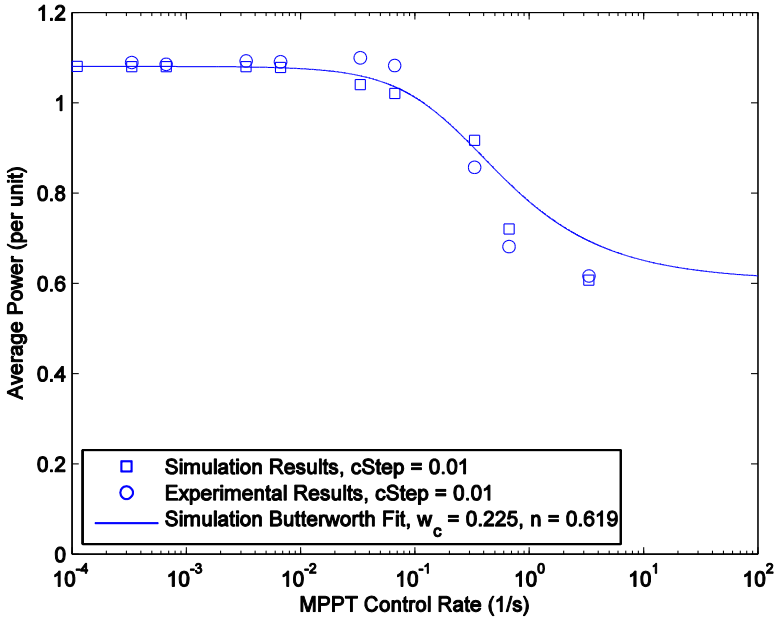

Fig. 6.23. Two-dimensional two-step radial MPPT experimental and simulation results for *cStep* of 0.01: normalized average power as a function of *cRate* with simulation Butterworth least-squares fit.

6.7 Observations

6.7.1 Comparison of Two-Variable Control Algorithms

Comparing the results obtained with each two-variable MPPT control, some commonalities are found. All control produced near the same maximum average power of 1.08 per unit when their control rates were slow and not having significant effect on the control variables during the fifteen minute position profile. Also of note is that the average power plotted by the control rate for each algorithm rolls off at faster control rates, resembling the frequency response of a Butterworth filter. The average power of all algorithms decreases to nearly the same level at high control rates; the result of excessive dithering of the control variables causing an average control value in the middle of the allowed range for both resistance and inductance. In some cases, such as with the faster time constants of the four-step

control, these control variables saturated to one extreme of their allowed range, producing the minimum average power levels shown in the results.

The least-squares Butterworth fit of the simulation results for each control scheme is compared in Fig. 6.24. Along with average power response of each control, a vertical marker at their respective corner frequencies is shown. The two-dimensional four-step MPPT shows poor performance with the corner frequency less than ten percent that of the other three control algorithms. This is partially due to the control requiring five periods of τ_mppt to implement a permanent control change, but mostly reflects the tendency of this control to favor the first and last control trials in the loop with faster MPPT time constants.

The two-variable independent, two-dimensional two-step, and two-dimensional radial MPPT control algorithms all performed favorably with corner frequencies on the same order of magnitude. The two-dimensional two-step radial MPPT algorithm performs most favorably up to this corner frequency as its average power curve had the highest order of the three. The two-dimensional two-step MPPT control had the lowest order, thus the shallowest roll off in power, resulting in lower performance below the corner frequency, but higher performance above. The two-variable independent MPPT control also performed well, though as its average power response is below that of the two-dimensional two-step radial MPPT control for all values of *cRate*, it holds no advantage other than in simplicity of control.

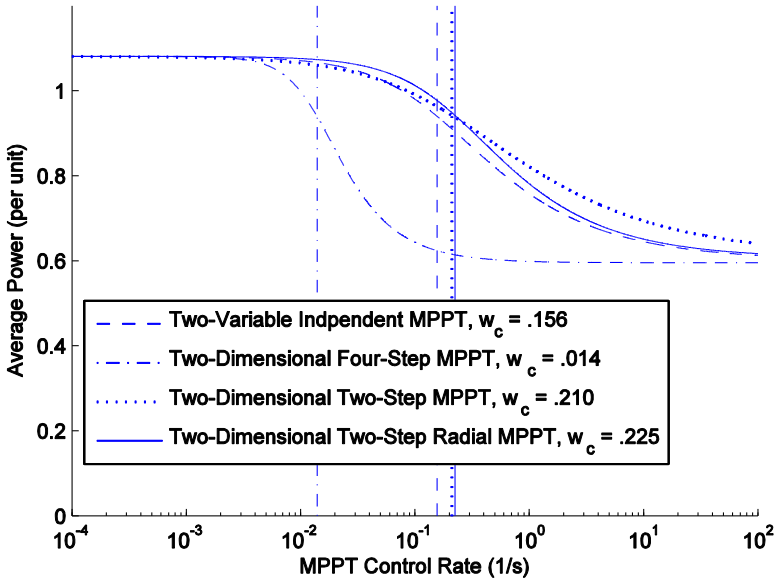

Fig. 6.24. Comparison of the least-squares Butterworth fit from simulation for each control algorithm with corner frequencies indicated.

6.7.2 MPPT Control Rate, *cRate*

Choosing the optimal values for *cRate* may be influenced by several factors. For optimal power production in a permanent installation in the ocean, a slow control rate seems favorable as this produces the maximum average power. A slow control rate would tune the device for the long-term changing sea state and would eliminate the reduction in power due to excessive dithering of the control variables. For the purposes of this investigation, optimal values selected would be closer to the corner frequency for each algorithm, as the faster control rates allow significant change to occur within the short, fifteen minute time period over which both simulation and experimental tests were performed. There is no apparent advantage of choosing a *cRate* beyond the corner frequency of the response curve as this results in poor performance for all algorithms.

To observe the optimal control rates for the fifteen minute testing period, the previous group of *cRate* and τ_*mppt* was simulated for each control scheme with non-optimal initial conditions. The resistance command was initialized at two times the optimal value, and the inductance command was initialized at zero. The expected result is reduced average power for the slowest values of *cRate*, increasing as *cRate* becomes large enough to impact the results during the fifteen minute testing period, then falling off for values above the corner frequency. As shown in Figs. 6.25-6.28, most algorithms performed as expected, with the average power beginning to increase near one decade below the corner frequency and falling off above. The two-dimensional four-step algorithm showed little average power increase near the corner frequency, indicating that its optimal value of *cRate* is too slow to perform well within the short fifteen minute test period.

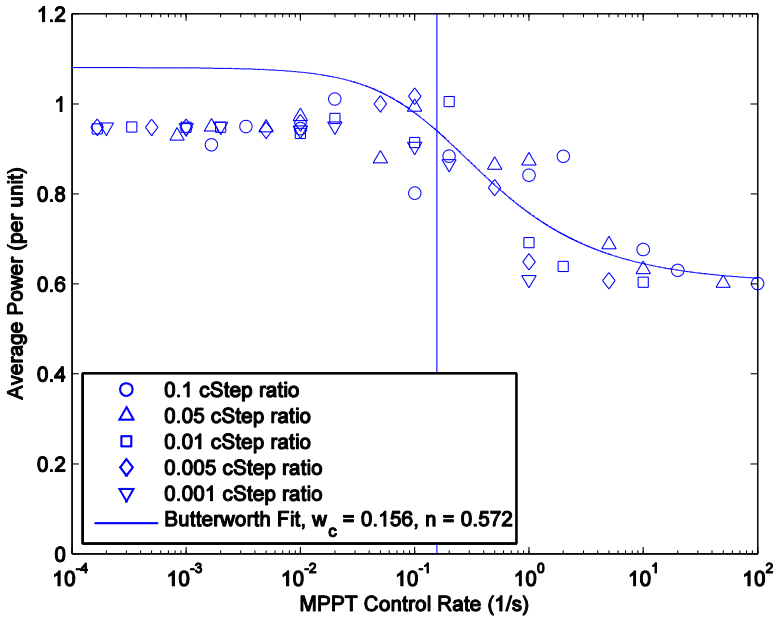

Fig. 6.25. Two-variable independent MPPT simulation results with non-optimal initial conditions.

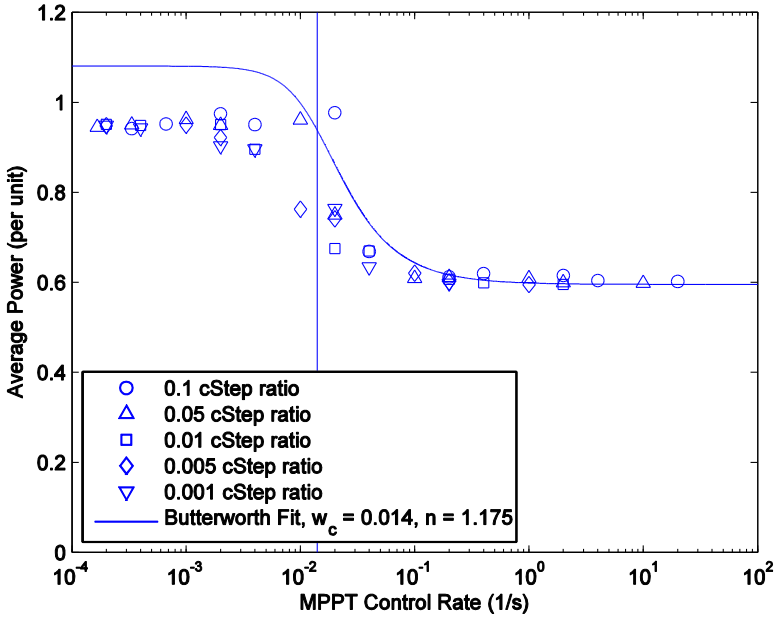

Fig. 6.26. Two-dimensional four-step MPPT simulation results with non-optimal initial conditions.

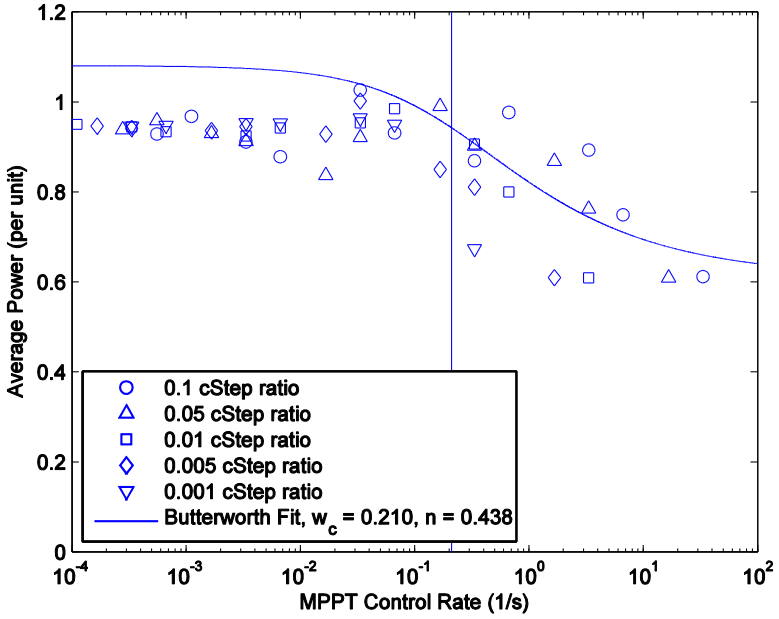

Fig. 6.27. Two-dimensional two-step MPPT simulation results with non-optimal initial conditions.

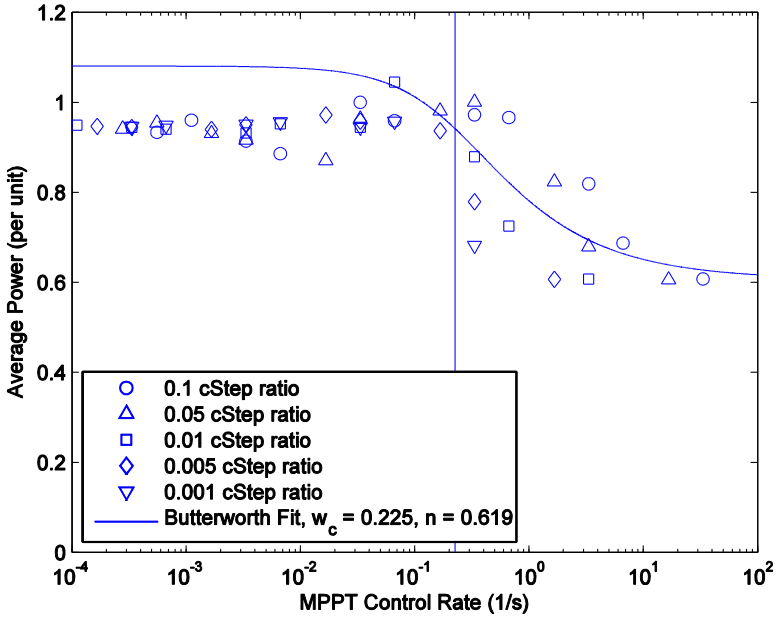

Fig. 6.28. Two-dimensional two-step radial MPPT simulation results with non-optimal initial conditions.

Following the selection of an optimal control rate for a specific application, the values of *cStep* and τ_mppt which make up this control rate must be chosen. From the results shown in Figs. 6.4, 6.9, 6.15, and 6.20, it is observed that the smaller values of *cStep* produce somewhat more consistent results. The largest value of *cStep* tested, 0.1, resulted in a significant loss of power for τ_mppt of one second with both the two-variable independent and two-dimensional two-step MPPT algorithms. This larger control step size also produced the most variation above the corner frequency in all algorithms. Compare this with a *cStep* of 0.01, which showed a very flat response with little variation out to the corner frequency of the average power response. Combining a *cStep* of 0.01 with the corner frequency of each control algorithm will yield the minimum value of τ_mppt to achieve optimal results. This results in τ_mppt of 0.0641 seconds from equation (6.1) for the two-variable independent MPPT control, τ_mppt of 0.143 seconds

from equation (6.3) for the two-dimensional four-step MPPT control, τ_mppt of 0.0159 seconds from equation (6.4) for the two-dimensional two-step MPPT control, and τ_mppt of 0.0148 seconds from equation (6.4) for the two-dimensional two-step radial MPPT control. Again, these would be the minimum recommended values for τ_mppt in each control given a *cStep* of 0.1, with values one decade larger providing more optimal results as the operating point approaches the maximum in the average power curve. The average power curve by τ_mppt with this *cStep* of 0.01 is given for each control algorithm in Fig. 6.29.

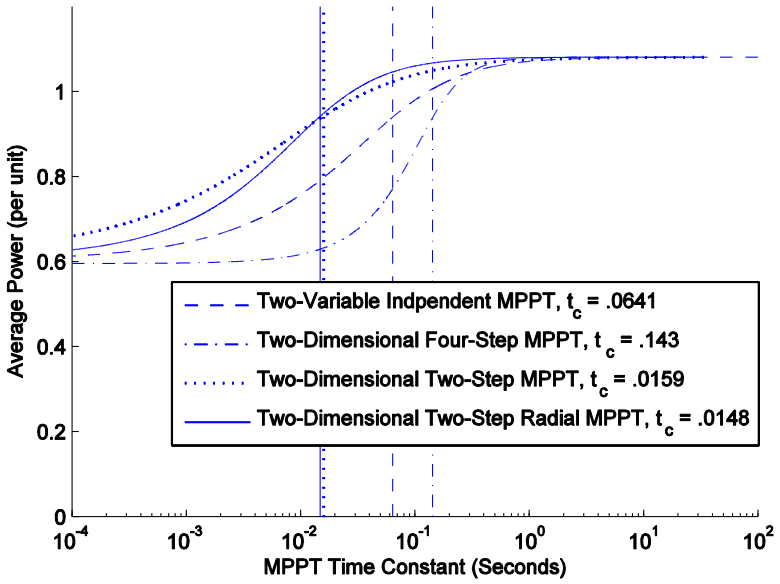

Fig. 6.29. Comparison of the least-squares Butterworth fit from simulation for each control algorithm, plotted by τ_mppt for *cStep* of 0.1.

7. CONCLUSION

7.1 Conclusions

7.1.1 Power Analysis and Data Acquisition System

An inclusive system for the testing and characterization of ocean wave energy devices has been presented. Capabilities of the system's electrical loading and data acquisition components were demonstrated using results from the ocean testing of a WEC prototype and in experimental testing in ocean wave energy control investigations.

A real-time, hardware-in-loop rapid prototyping system was utilized, allowing control system modifications to be made easily to ideally load and monitor a wave energy device under test. System control models are constructed with MATLAB Simulink, simplifying the integration of hardware following testing in simulation. The system topology allows interfacing with wave energy devices of various electrical output configurations, both single- and three-phase, in dc, ac, or variable-frequency ac. The system enclosure is water-tight, using waterproof bulkhead connectors for all power- and signal-level connections, making it ideal for characterizing wave energy device prototypes in the harsh ocean environment.

Development of this system is crucial to the evaluation of future wave energy device prototypes in a marine environment. The ability to test these prototypes in the ocean, under normal operating conditions, will allow optimal topologies to be identified and the simple control interface allows control optimization to be performed to maximize power extraction from ocean waves.

7.1.2 Maximum Power Point Tracking for Wave Energy Converters

MPPT was investigated for application to WECs. A single-variable "perturb and observe" algorithm was implemented, both experimentally and in simulation, to evaluate the effectiveness of MPPT in an ocean wave environment and to

determine optimal time-scales over which to perform MPPT. Application to both passive and active rectifier topologies demonstrated that the control may be universally applied to different control variables with favorable results.

Two-variable MPPT algorithms were presented, with both independent variable and two-dimensional control schemes. Evaluating the performance of these control algorithms revealed the relationship between average power and the control rate, which is a function of the control step size, MPPT time constant, and loop iteration count between permanent control changes. Two-dimensional control showed promising results, with the exception of the four-step approach, which suffered due to the extended duration over which it performed control alteration trials. The two-step variants both performed admirably, showing increased power production compared with single-variable and two-variable independent control. This indicated the reduction in decision errors with the implementation of trial steps, as opposed to making permanent control changes in every iteration. Recommendations were made for optimal control rates for each two-variable control presented and MPPT time constants were identified based on these control rates and the control step sizes yielding consistent average power production.

7.2 Recommendations for Future Work

Evaluation of these control schemes in a hydrodynamic environment would yield more accurate control rate and MPPT time constant recommendations for application in ocean wave energy. Hydrodynamic force control of the LTB is currently under development, which would allow experimental testing of such control schemes in the laboratory environment [27]. Linearized hydrodynamics could be implemented in the analytical models to allow control evaluation prior to performing experimental verification. Investigations in MPPT control of greater than two variables could be performed, yielding solutions for more complicated systems with more than two tunable performance variables. Additionally,

investigations could be performed into MPPT control utilizing tunable control rate or MPPT time constants and control step size as in [6, 12]; yielding algorithms which adapt not only their output, but also their operation to the system and operating environment.

BIBLIOGRAPHY

[1] L. Ran, P. Tavner, M. Mueller, N. Baker, S. McDonald, "Power conversion and control for a low speed, permanent magnet, direct-drive, wave energy converter," Power Electronics, Machines and Drives, 2006. The 3rd IET International Conference on, 2006, pp. 17-21.

[2] H. Polinder, B. Mecrow, A. Jack, P. Dickinson, M. Mueller, "Conventional and TFPM linear generators for direct-drive wave energy conversion," *IEEE Transactions on Energy Conversion*, vol. 20, no. 2, June 2005.

[3] P. Brooking, M. Mueller, "Power conditioning of the output from a linear vernier hybrid permanent magnet generator for use in direct drive wave energy converters," Generation, Transmission and Distribution, IEEE Proceedings- 152 (5) (2005) 673-681. Doi:10.1049/ip-gtd:20045134.

[4] J. Falnes, *Ocean Waves and Oscillating Systems.* Cambridge University Press, 2002.

[5] M. Patel, *Dynamics of Offshore Structures*. Butterworth-Heinemann, 1989.

[6] T. Esram, P. Chapman, "Comparison of photovoltaic array maximum power point tracking techniques," *IEEE Transactions on Energy Conversion*, vol. 22, no. 2, pp. 439-449, June 2007.

[7] N. Femia, G. Petrone, G. Spagnuolo, and M. Vitelli, "Optimization of perturb and observe maximum power point tracking method," *IEEE Transactions on Power Electronics*, vol. 20, no. 4, pp. 963-973, July 2005.

[8] Y. Da, A. Khaligh, "Hybrid offshore wind and tidal turbine energy harvesting system with independently controlled rectifiers," in *Industrial Electronics*, 2009, IECON '09. 35th Annual Conference of IEEE, 3-5 2009, pp. 4577-4582.

[9] S. Ben Elghali, M. Benbouzid, J. Charpentier, T. Ahmed-Ali, J. Gahery, A. Denis, "Modeling and mppt sensorless control of a dfig-based marine current turbine," in *Electrical Machines, 2008. ICEM 2008. 18th International Conference on*, 6-9 2008, pp. 1-6.

[10] J. S. Choi, R. G. Jeong, J. H. Shin, C. K. Kim, Y. S. Kim, "New control method of maximum power point tracking for tidal energy generation system," in *Electrical Machines and Systems, 2007. ICEMS. International Conference on*, 8-11 2007, pp.165-168.

[11] Y. Jiang, M. F. Rong, L. Y. Hua, "Variable speed constant frequency tidal current energy generation and control strategy for maximum power point tracking and grid connections," in *Sustainable Power Generation and Supply, 2009. SUPERGEN '09. International Conference on*, 6-7 2009, pp. 1-6.

[12] J. Elmes, V. Gaydarzhiev, A. Mensah, K. Rustom, J. Shen, I. Batarseh, "Maximum energy harvesting control for oscillating energy harvesting systems," in *Power Electronics Specialists Conference, 2007. PESC 2007. IEEE*, June 2007, pp. 2792-2798.

[13] H. Luan, O. Onar, A. Khaligh, "Dynamic modeling and optimum load control of a pm linear generator for ocean wave energy harvesting application," in *Applied Power Electronics Conference and Exposition, 2009. APEC 2009. Twenty-Fourth Annual IEEE*, 2009, pp. 739-743.

[14] R. Waters, M. Stalberg, O. Danielsson, O. Svensson, S. Gustafsson, E. Stromstedt, M. Eriksson, J. Sundberg, M. Leijon, "Experimental results from sea trials of an offshore wave energy system," *Applied Physics Letters*, vol. 90, no. 3, pp. 034 105-034 105-3, Jan 2007.

[15] C. Bostrom, E. Lejerskog, M. Stalberg, K. Thorburn, M. Leijon, "Experimental results of rectification and filtration from an offshore wave energy system," *Renewable Energy*, vol. 34, no. 5, pp. 1381-1387, 2009.

[16] C. Bostrom, R. Waters, E. Lejerskog, O. Svensson, M. Stalberg, E. Stromstedt, M. Leijon, "Study of a wave energy converter connected to a nonlinear load," *Oceanic Engineering, IEEE Journal of*, vol. 34, no. 2, pp. 123-127, April 2009.

[17] J.W. Baek, M.H. Ryoo, J.H. Kim, J.S. Lai, "50kVA Regenerative Active load for power test system," presented at the 2007 European Conference on Power Electronics and Applications, Sept. 2-5, 2007.

[18] I.Y. Chung, D.J. Won, J.M. Kim, S.J. Ahn, S.I. Moon, J.C. Seo, J.W. Choe, "Development of Power Quality Diagnosis Systems for Power Quality Improvement," IEEE Power Engineering Society General Meeting, Vol. 2, July 13-17, 2003.

[19] T.K.A. Brekken, A. von Jouanne, H.Y. Han, "Ocean Wave Energy Overview and Research at Oregon State University," invited paper, Symposium on Power Electronics and Machines in Wind Applications (PEMWA), Licoln, Nebraska, June 2009.

[20] T.K.A. Brekken, J. Prudell, A. von Jouanne, and M. Stoddard, "A novel permanent magnet tubular linear generator for ocean wave energy," in *Proceedings of Energy Conversion Congress and Exposition (ECCE)*, Sept. 2009.

[21] J. Prudell, M. Stoddard, E. Amon, T.K.A. Brekken, and A. von Jouanne, "A permanent magnet tubular linear generator for ocean wave energy conversion," *accepted for publication in IEEE Transactions on Industry Applications*, 2010.

[22] D. Elwood, S. Yim, J. Prudell, A. von Jouanne, T. Brekken, A. Brown, C. Stillinger, R. Paasch, "Design, Construction, and Ocean Testing of a Taut-Moored Dual-Body Wave Energy Converter With a Linear Generator Power Take-Off," Renewable Energy, An International Journal, accepted for publication.

[23] P.M. Hogan, "A Linear Test Bed for Characterizing the Performance of Ocean Wave Energy Converters," M.S. Thesis, Dept. of EECS, Oregon State University, Corvallis, OR, 2007.

[24] D. Elwood, S. Yim, E. Amon, A. von Jouanne, T. Brekken, "Estimating the Energy Production Capacity of a Taught Moored, Dual Body, Wave Energy Conversion System using Numerical Modeling and Physical Testing," Journal of Offshore Mechanics and Arctic Engineering, accepted for publication.

[25] D. Elwood, S. Yim, E. Amon, A. von Jouanne, T. Brekken, "Experimental Force Characterization and Numerical Modeling of a Taught Moored Dual Body Wave Energy Conversion System," Journal of Offshore Mechanics and Arctic Engineering, accepted for publication.

[26] D. Elwood, S. Yim, A. Schacher, K. Rhinefrank, J. Prudell, E. Amon, T. Brekken, A. von Jouanne, "Numerical Modeling and Ocean Testing of a Direct-Drive Wave Energy Device Utilizing a Permanent Magnet Linear Generator for Power Take-Off," International Conference on Offshore Mechanics and Arctic Engineering (OMAE), Honolulu, Hawaii, June 2009.

[27] N.R. Henshaw, “A Force Control Algorithm for a Wave Energy Linear Test Bed,” M.S. Thesis, Dept. of EECS, Oregon State University, Corvallis, OR 2009.

APPENDICES

A. Two-Dimensional Four-Step MPPT, Level-2 M-File S-Function Code

```
function two_dim_4step_l2sfun(block)

setup(block);

%endfunction

function setup(block)

  %% Register dialog parameter: LMS step size
  block.NumDialogPrms = 3;

  %% Regieste number of input and output ports
  block.NumInputPorts  = 1;
  block.NumOutputPorts = 5;

  %% Setup functional port properties to dynamically
  %% inherited.
  block.SetPreCompInpPortInfoToDynamic;
  block.SetPreCompOutPortInfoToDynamic;

  block.InputPort(1).Complexity   = 'Real';
  block.InputPort(1).DataTypeId   = 0;
  block.InputPort(1).SamplingMode = 'Sample';
  block.InputPort(1).Dimensions   = 1;

  block.OutputPort(1).Complexity   = 'Real';
  block.OutputPort(1).DataTypeId   = 0;
  block.OutputPort(1).SamplingMode = 'Sample';
  block.OutputPort(1).Dimensions   = 1;

  block.OutputPort(2).Complexity   = 'Real';
  block.OutputPort(2).DataTypeId   = 0;
  block.OutputPort(2).SamplingMode = 'Sample';
  block.OutputPort(2).Dimensions   = 4;

  block.OutputPort(3).Complexity   = 'Real';
  block.OutputPort(3).DataTypeId   = 0;
  block.OutputPort(3).SamplingMode = 'Sample';
  block.OutputPort(3).Dimensions   = 1;

  block.OutputPort(4).Complexity   = 'Real';
  block.OutputPort(4).DataTypeId   = 0;
  block.OutputPort(4).SamplingMode = 'Sample';
  block.OutputPort(4).Dimensions   = 1;

  block.OutputPort(5).Complexity   = 'Real';
  block.OutputPort(5).DataTypeId   = 0;
  block.OutputPort(5).SamplingMode = 'Sample';
  block.OutputPort(5).Dimensions   = 4;

  %% Set the block simStateCompliance to default (i.e., same as a built-in block)
  block.SimStateCompliance = 'DefaultSimState';

  %% Register methods
  block.RegBlockMethod('PostPropagationSetup',    @DoPostPropSetup);
  block.RegBlockMethod('Start',                   @Start);
  block.RegBlockMethod('Outputs',                 @Outputs);

  %% Block runs on TLC in accelerator mode.
  block.SetAccelRunOnTLC(true);
```

```
%endfunction

function DoPostPropSetup(block)

  %% Setup Dwork
  block.NumDworks = 5;

  block.Dwork(1).Name = 'state';
  block.Dwork(1).Dimensions      = 1;
  block.Dwork(1).DatatypeID      = 0;
  block.Dwork(1).Complexity      = 'Real';
  block.Dwork(1).UsedAsDiscState = true;

  block.Dwork(2).Name = 'P_avg';
  block.Dwork(2).Dimensions      = 4;
  block.Dwork(2).DatatypeID      = 0;
  block.Dwork(2).Complexity      = 'Real';
  block.Dwork(2).UsedAsDiscState = true;

  block.Dwork(3).Name = 'R_cmd';
  block.Dwork(3).Dimensions      = 4;
  block.Dwork(3).DatatypeID      = 0;
  block.Dwork(3).Complexity      = 'Real';
  block.Dwork(3).UsedAsDiscState = true;

  block.Dwork(4).Name = 'L_cmd';
  block.Dwork(4).Dimensions      = 4;
  block.Dwork(4).DatatypeID      = 0;
  block.Dwork(4).Complexity      = 'Real';
  block.Dwork(4).UsedAsDiscState = true;

  block.Dwork(5).Name = 'Decisions';
  block.Dwork(5).Dimensions      = 4;
  block.Dwork(5).DatatypeID      = 0;
  block.Dwork(5).Complexity      = 'Real';
  block.Dwork(5).UsedAsDiscState = true;

  %% Register all tunable parameters as runtime parameters.
  block.AutoRegRuntimePrms;

%endfunction

function Start(block)

  %% Initialize Dwork

  block.Dwork(1).Data = 5;
  block.Dwork(2).Data = [0 0 0 0];
  block.Dwork(3).Data = [block.DialogPrm(2).Data 0 0 0]; % initial R_cmd
  block.Dwork(4).Data = [block.DialogPrm(3).Data 0 0 0]; % initial L_cmd
  block.Dwork(5).Data = [0 0 0 0];

%endfunction

function Outputs(block)

  c_step = block.DialogPrm(1).Data; % initialize c_step from block parameters
  R_init = block.DialogPrm(2).Data; % initialize R_init from block parameters
  L_init = block.DialogPrm(3).Data; % initialize L_init from block parameters

  state=block.Dwork(1).Data;    % load state from memory
  decisions=block.Dwork(5).Data;    % load decisions from memory

  pavg(2:4) = block.Dwork(2).Data(1:3); % load power history
  pavg(1) = block.InputPort(1).Data;    % input new power
```

```
R_cmd(1:4) = block.Dwork(3).Data(1:4);     % load R_cmd history from memory
L_cmd(1:4) = block.Dwork(4).Data(1:4);     % load R_cmd history from memory

block.OutputPort(1).Data = state; % output current state before incrementing

if state==5   % initial startup, like state 0 with no control change
    state=1;  % go to state 1

elseif state==0   % control evaluation and change state
    [Y,I] = max(pavg);    % obtain index of highest power state

    if I==4       % restore state 1 control
        R_cmd(1)=R_cmd(1)+c_step*R_init;  % increment R_cmd
        L_cmd(1)=L_cmd(1)+c_step*L_init;  % increment L_cmd
        decisions(1)=decisions(1)+1;  % increment count of this decision

    elseif I==3   % restore state 2 control
        L_cmd(1)=L_cmd(1)+2*c_step*L_init;% increment L_cmd twice
        decisions(2)=decisions(2)+1;  % increment count of this decision

    elseif I==2   % restore state 3 control
        R_cmd(1)=R_cmd(1)-c_step*R_init;  % decrement R_cmd
        L_cmd(1)=L_cmd(1)+c_step*L_init;  % increment L_cmd
        decisions(3)=decisions(3)+1;  % increment count of this decision

    elseif I==1   % do nothing, maintain state 4 control from previous
        decisions(4)=decisions(4)+1;  % increment count of this decision
    end
    state=1;  % go to state 1

elseif state==1   % control trial 1: increase R_cmd
    R_cmd(2:4)=R_cmd(1:3);    % shift variable
    L_cmd(2:4)=L_cmd(1:3);    % shift variable
    R_cmd(1)=R_cmd(1)+c_step*R_init;  % increment R_cmd
    state=2;  % go to state 2

elseif state==2   % control trial 2: return R_cmd, increase neg L_cmd
    R_cmd(2:4)=R_cmd(1:3);    % shift variable
    L_cmd(2:4)=L_cmd(1:3);    % shift variable
    R_cmd(1)=R_cmd(1)-c_step*R_init;  % return R_cmd
    L_cmd(1)=L_cmd(1)+c_step*L_init;  % increment L_cmd
    state=3;  % go to state 3

elseif state==3   % control trial 3: return L_cmd, decrement R_cmd
    R_cmd(2:4)=R_cmd(1:3);    % shift variable
    L_cmd(2:4)=L_cmd(1:3);    % shift variable
    L_cmd(1)=L_cmd(1)-c_step*L_init;  % return L_cmd
    R_cmd(1)=R_cmd(1)-c_step*R_init;  % decrement R_cmd
    state=4;  % go to state 4

else              % control trial 4: return R_cmd, decrease neg L_cmd
    R_cmd(2:4)=R_cmd(1:3);    % shift variable
    L_cmd(2:4)=L_cmd(1:3);    % shift variable
    R_cmd(1)=R_cmd(1)+c_step*R_init;  % return R_cmd
    L_cmd(1)=L_cmd(1)-c_step*L_init;  % decrement L_cmd
    state=0;  % go to state 0
end

% set limits on R_cmd
if R_cmd(1) > 5*R_init
    R_cmd(1) = 5*R_init;
elseif R_cmd(1) < 0.5*R_init
    R_cmd(1) = 0.5*R_init;
end
```

```
  % set limits on L_cmd
  if L_cmd(1) > -1*L_init
      L_cmd(1) = -1*L_init;
  elseif L_cmd(1) < 3*L_init
      L_cmd(1) = 3*L_init;
  end

  % new outputs following control changes
  block.OutputPort(2).Data = pavg;
  block.OutputPort(3).Data = R_cmd(1);
  block.OutputPort(4).Data = L_cmd(1);
  block.OutputPort(5).Data = decisions;

  % save data to dwork memory
  block.Dwork(1).Data = state;
  block.Dwork(2).Data = pavg;
  block.Dwork(3).Data = R_cmd;
  block.Dwork(4).Data = L_cmd;
  block.Dwork(5).Data = decisions;

%endfunction
```

B. Two-Dimensional Two-Step MPPT, Level-2 M-File S-Function Code

```
function two_dim_2step_l2sfun(block)

setup(block);

%endfunction

function setup(block)

  %% Register dialog parameter: LMS step size
  block.NumDialogPrms = 3;

  %% Regieste number of input and output ports
  block.NumInputPorts  = 1;
  block.NumOutputPorts = 5;

  %% Setup functional port properties to dynamically
  %% inherited.
  block.SetPreCompInpPortInfoToDynamic;
  block.SetPreCompOutPortInfoToDynamic;

  block.InputPort(1).Complexity   = 'Real';
  block.InputPort(1).DataTypeId   = 0;
  block.InputPort(1).SamplingMode = 'Sample';
  block.InputPort(1).Dimensions   = 1;

  block.OutputPort(1).Complexity   = 'Real';
  block.OutputPort(1).DataTypeId   = 0;
  block.OutputPort(1).SamplingMode = 'Sample';
  block.OutputPort(1).Dimensions   = 1;

  block.OutputPort(2).Complexity   = 'Real';
  block.OutputPort(2).DataTypeId   = 0;
  block.OutputPort(2).SamplingMode = 'Sample';
  block.OutputPort(2).Dimensions   = 3;

  block.OutputPort(3).Complexity   = 'Real';
  block.OutputPort(3).DataTypeId   = 0;
  block.OutputPort(3).SamplingMode = 'Sample';
  block.OutputPort(3).Dimensions   = 1;

  block.OutputPort(4).Complexity   = 'Real';
  block.OutputPort(4).DataTypeId   = 0;
  block.OutputPort(4).SamplingMode = 'Sample';
  block.OutputPort(4).Dimensions   = 1;

  block.OutputPort(5).Complexity   = 'Real';
  block.OutputPort(5).DataTypeId   = 0;
  block.OutputPort(5).SamplingMode = 'Sample';
  block.OutputPort(5).Dimensions   = 4;

  %% Set the block simStateCompliance to default (i.e., same as a built-in block)
  %block.SimStateCompliance = 'DefaultSimState';

  %% Register methods
  block.RegBlockMethod('PostPropagationSetup',    @DoPostPropSetup);
  block.RegBlockMethod('Start',                   @Start);
  block.RegBlockMethod('Outputs',                 @Outputs);

  %% Block runs on TLC in accelerator mode.
  block.SetAccelRunOnTLC(true);
```

```
%endfunction

function DoPostPropSetup(block)

  %% Setup Dwork
  block.NumDworks = 6;

  block.Dwork(1).Name = 'state';
  block.Dwork(1).Dimensions      = 1;
  block.Dwork(1).DatatypeID      = 0;
  block.Dwork(1).Complexity      = 'Real';
  block.Dwork(1).UsedAsDiscState = true;

  block.Dwork(2).Name = 'P_avg';
  block.Dwork(2).Dimensions      = 3;
  block.Dwork(2).DatatypeID      = 0;
  block.Dwork(2).Complexity      = 'Real';
  block.Dwork(2).UsedAsDiscState = true;

  block.Dwork(3).Name = 'R_cmd';
  block.Dwork(3).Dimensions      = 4;
  block.Dwork(3).DatatypeID      = 0;
  block.Dwork(3).Complexity      = 'Real';
  block.Dwork(3).UsedAsDiscState = true;

  block.Dwork(4).Name = 'L_cmd';
  block.Dwork(4).Dimensions      = 4;
  block.Dwork(4).DatatypeID      = 0;
  block.Dwork(4).Complexity      = 'Real';
  block.Dwork(4).UsedAsDiscState = true;

  block.Dwork(5).Name = 'Decisions';
  block.Dwork(5).Dimensions      = 4;
  block.Dwork(5).DatatypeID      = 0;
  block.Dwork(5).Complexity      = 'Real';
  block.Dwork(5).UsedAsDiscState = true;

  block.Dwork(6).Name = 'direction';
  block.Dwork(6).Dimensions      = 2;
  block.Dwork(6).DatatypeID      = 0;
  block.Dwork(6).Complexity      = 'Real';
  block.Dwork(6).UsedAsDiscState = true;

  %% Register all tunable parameters as runtime parameters.
  block.AutoRegRuntimePrms;

%endfunction

function Start(block)

  %% Initialize Dwork

  block.Dwork(1).Data = 5;
  block.Dwork(2).Data = [0 0 0];
  block.Dwork(3).Data = [block.DialogPrm(2).Data 0 0 0]; % initial R_cmd
  block.Dwork(4).Data = [block.DialogPrm(3).Data 0 0 0]; % initial L_cmd
  block.Dwork(5).Data = [0 0 0 0];
  block.Dwork(6).Data = [1 1];

%endfunction

function Outputs(block)

  c_step = block.DialogPrm(1).Data; % initialize c_step from block parameters
  R_init = block.DialogPrm(2).Data; % initialize R_init from block parameters
```

```
L_init = block.DialogPrm(3).Data; % initialize L_init from block parameters

state=block.Dwork(1).Data;    % load state from memory
decisions=block.Dwork(5).Data;    % load decisions from memory
direction=block.Dwork(6).Data;    % load directions from memory

pavg(2:3) = block.Dwork(2).Data(1:2); % load power history
pavg(1) = block.InputPort(1).Data;    % input new power

R_cmd(1:4) = block.Dwork(3).Data(1:4);    % load R_cmd history from memory
L_cmd(1:4) = block.Dwork(4).Data(1:4);    % load R_cmd history from memory

block.OutputPort(1).Data = state; % output current state before incrementing

if state==5 % initial startup, like state 0 with no control change
    state=1;  % go to state 1

elseif state==0   % control evaluation and change state
    L_cmd(1)=L_cmd(1)-direction(2)*c_step*L_init; % return L_cmd

    if pavg(2)>pavg(3)    % change R_cmd in same direction
        R_cmd(1)=R_cmd(1)+direction(1)*c_step*R_init;
        decisions(1)=decisions(1)+1;  % increment count of this decision

    else
        R_cmd(1)=R_cmd(1)-direction(1)*c_step*R_init; % change R_cmd
        direction(1)=-1*direction(1);                 % and reverse direction
        decisions(2)=decisions(2)+1;  % increment count of this decision
    end

    if pavg(1)>pavg(3)    % change L_cmd in same direction
        L_cmd(1)=L_cmd(1)+direction(2)*c_step*L_init;
        decisions(3)=decisions(3)+1;  % increment count of this decision
    else
        L_cmd(1)=L_cmd(1)-direction(2)*c_step*L_init; % change L_cmd
        direction(2)=-1*direction(2);                 % and reverse direction
        decisions(4)=decisions(4)+1;  % increment count of this decision
    end
    state=1;  % go to state 1

elseif state==1   % control trial 1

    R_cmd(2:4)=R_cmd(1:3);    % shift variable
    L_cmd(2:4)=L_cmd(1:3);    % shift variable
    R_cmd(1)=R_cmd(1)+direction(1)*c_step*R_init; % increment R_cmd
    state=2;  % go to state 2

elseif state==2   % control trial 2

    R_cmd(2:4)=R_cmd(1:3);    % shift variable
    L_cmd(2:4)=L_cmd(1:3);    % shift variable
    R_cmd(1)=R_cmd(1)-direction(1)*c_step*R_init; % return R_cmd
    L_cmd(1)=L_cmd(1)+direction(2)*c_step*L_init; % increment L_cmd
    state=0;  % go to state 0
end

% set limits on R_cmd
if R_cmd(1) > 5*R_init
    R_cmd(1) = 5*R_init;
elseif R_cmd(1) < 0.5*R_init
    R_cmd(1) = 0.5*R_init;
end

% set limits on L_cmd
if L_cmd(1) > -1*L_init
```

```
        L_cmd(1) = -1*L_init;
    elseif L_cmd(1) < 3*L_init
        L_cmd(1) = 3*L_init;
    end

    % new outputs following control changes
    block.OutputPort(2).Data = pavg;
    block.OutputPort(3).Data = R_cmd(1);
    block.OutputPort(4).Data = L_cmd(1);
    block.OutputPort(5).Data = decisions;

    % save data to dwork
    block.Dwork(1).Data = state;
    block.Dwork(2).Data = pavg;
    block.Dwork(3).Data = R_cmd;
    block.Dwork(4).Data = L_cmd;
    block.Dwork(5).Data = decisions;
    block.Dwork(6).Data = direction;

%endfunction
```

C. Two-Dimensional Two-Step Radial MPPT, Level-2 M-File S-Function Code

```
function two_dim_2step_radial_l2sfun(block)

setup(block);

%endfunction

function setup(block)

  %% Register dialog parameter: LMS step size
  block.NumDialogPrms = 3;
  % block.DialogPrmsTunable = {'Tunable'};
  % block.DialogPrm(1).Name = 'StepSize';
  % block.DialogPrm(1).DataTypeId = 0;

  %% Regieste number of input and output ports
  block.NumInputPorts  = 1;
  block.NumOutputPorts = 5;

  %% Setup functional port properties to dynamically
  %% inherited.
  block.SetPreCompInpPortInfoToDynamic;
  block.SetPreCompOutPortInfoToDynamic;

  block.InputPort(1).Complexity   = 'Real';
  block.InputPort(1).DataTypeId   = 0;
  block.InputPort(1).SamplingMode = 'Sample';
  block.InputPort(1).Dimensions   = 1;

  block.OutputPort(1).Complexity   = 'Real';
  block.OutputPort(1).DataTypeId   = 0;
  block.OutputPort(1).SamplingMode = 'Sample';
  block.OutputPort(1).Dimensions   = 1;

  block.OutputPort(2).Complexity   = 'Real';
  block.OutputPort(2).DataTypeId   = 0;
  block.OutputPort(2).SamplingMode = 'Sample';
  block.OutputPort(2).Dimensions   = 3;

  block.OutputPort(3).Complexity   = 'Real';
  block.OutputPort(3).DataTypeId   = 0;
  block.OutputPort(3).SamplingMode = 'Sample';
  block.OutputPort(3).Dimensions   = 1;

  block.OutputPort(4).Complexity   = 'Real';
  block.OutputPort(4).DataTypeId   = 0;
  block.OutputPort(4).SamplingMode = 'Sample';
  block.OutputPort(4).Dimensions   = 1;

  block.OutputPort(5).Complexity   = 'Real';
  block.OutputPort(5).DataTypeId   = 0;
  block.OutputPort(5).SamplingMode = 'Sample';
  block.OutputPort(5).Dimensions   = 4;

  %% Set the block simStateCompliance to default (i.e., same as a built-in block)
  %block.SimStateCompliance = 'DefaultSimState';

  %% Register methods
  block.RegBlockMethod('PostPropagationSetup',    @DoPostPropSetup);
  block.RegBlockMethod('Start',                   @Start);
  block.RegBlockMethod('Outputs',                 @Outputs);
```

```
  %% Block runs on TLC in accelerator mode.
  block.SetAccelRunOnTLC(true);

%endfunction

function DoPostPropSetup(block)

  %% Setup Dwork
  block.NumDworks = 6;

  block.Dwork(1).Name = 'state';
  block.Dwork(1).Dimensions      = 1;
  block.Dwork(1).DatatypeID      = 0;
  block.Dwork(1).Complexity      = 'Real';
  block.Dwork(1).UsedAsDiscState = true;

  block.Dwork(2).Name = 'P_avg';
  block.Dwork(2).Dimensions      = 3;
  block.Dwork(2).DatatypeID      = 0;
  block.Dwork(2).Complexity      = 'Real';
  block.Dwork(2).UsedAsDiscState = true;

  block.Dwork(3).Name = 'R_cmd';
  block.Dwork(3).Dimensions      = 4;
  block.Dwork(3).DatatypeID      = 0;
  block.Dwork(3).Complexity      = 'Real';
  block.Dwork(3).UsedAsDiscState = true;

  block.Dwork(4).Name = 'L_cmd';
  block.Dwork(4).Dimensions      = 4;
  block.Dwork(4).DatatypeID      = 0;
  block.Dwork(4).Complexity      = 'Real';
  block.Dwork(4).UsedAsDiscState = true;

  block.Dwork(5).Name = 'Decisions';
  block.Dwork(5).Dimensions      = 4;
  block.Dwork(5).DatatypeID      = 0;
  block.Dwork(5).Complexity      = 'Real';
  block.Dwork(5).UsedAsDiscState = true;

  block.Dwork(6).Name = 'direction';
  block.Dwork(6).Dimensions      = 2;
  block.Dwork(6).DatatypeID      = 0;
  block.Dwork(6).Complexity      = 'Real';
  block.Dwork(6).UsedAsDiscState = true;

  %% Register all tunable parameters as runtime parameters.
  block.AutoRegRuntimePrms;

%endfunction

function Start(block)

  %% Initialize Dwork

  block.Dwork(1).Data = 5;
  block.Dwork(2).Data = [0 0 0];
  block.Dwork(3).Data = [block.DialogPrm(2).Data 0 0 0]; % initial R_cmd
  block.Dwork(4).Data = [block.DialogPrm(3).Data 0 0 0]; % initial L_cmd
  block.Dwork(5).Data = [0 0 0 0];
  block.Dwork(6).Data = [1 1];

%endfunction

function Outputs(block)
```

```
c_step = block.DialogPrm(1).Data; % initialize c_step from block parameters
R_init = block.DialogPrm(2).Data; % initialize R_init from block parameters
L_init = block.DialogPrm(3).Data; % initialize L_init from block parameters

state=block.Dwork(1).Data;    % load state from memory
decisions=block.Dwork(5).Data;    % load decisions from memory
direction=block.Dwork(6).Data;    % load directions from memory

pavg(2:3) = block.Dwork(2).Data(1:2); % load power history
pavg(1) = block.InputPort(1).Data;    % input new power

R_cmd(1:4) = block.Dwork(3).Data(1:4);    % load R_cmd history from memory
L_cmd(1:4) = block.Dwork(4).Data(1:4);    % load R_cmd history from memory

block.OutputPort(1).Data = state; % output current state before incrementing

if state==5 % initial startup, like state 0 with no control change
    state=1;  % go to state 1

elseif state==0   % control evaluation and change state

    L_cmd(1)=L_cmd(1)-direction(2)*c_step*L_init; % return L_cmd

    p_total=sqrt((pavg(1)^2)+(pavg(2)^2));    % total power magnitude

    p_x_ratio=(pavg(2)/p_total)*sign(pavg(2)-pavg(3));    % R power ratio
    p_y_ratio=(pavg(1)/p_total)*sign(pavg(1)-pavg(3));    % L power ratio

    % alter R_cmd by power ratio and direction
    R_cmd(1)=R_cmd(1)+direction(1)*c_step*R_init*p_x_ratio;
    % alter L_cmd by power ratio and direction
    L_cmd(1)=L_cmd(1)+direction(2)*c_step*L_init*p_y_ratio;

    direction(1)=direction(1)*sign(p_x_ratio);    % new R direction
    direction(2)=direction(2)*sign(p_y_ratio);    % new L direction

    state=1;  % go to state 1

elseif state==1   % control trial 1

    R_cmd(2:4)=R_cmd(1:3);    % shift variable
    L_cmd(2:4)=L_cmd(1:3);    % shift variable
    R_cmd(1)=R_cmd(1)+direction(1)*c_step*R_init; % increment R_cmd
    state=2;  % go to state 2

elseif state==2   % control trial 2

    R_cmd(2:4)=R_cmd(1:3);    % shift variable
    L_cmd(2:4)=L_cmd(1:3);    % shift variable
    R_cmd(1)=R_cmd(1)-direction(1)*c_step*R_init; % return R_cmd
    L_cmd(1)=L_cmd(1)+direction(2)*c_step*L_init; % increment L_cmd
    state=0;  % go to state 0
end

% set limits on R_cmd
if R_cmd(1) > 5*R_init
    R_cmd(1) = 5*R_init;
elseif R_cmd(1) < 0.5*R_init
    R_cmd(1) = 0.5*R_init;
end

% set limits on L_cmd
if L_cmd(1) > -1*L_init
    L_cmd(1) = -1*L_init;
```

```
  elseif L_cmd(1) < 3*L_init
      L_cmd(1) = 3*L_init;
  end

  % new outputs following control changes
  block.OutputPort(2).Data = pavg;
  block.OutputPort(3).Data = R_cmd(1);
  block.OutputPort(4).Data = L_cmd(1);
  block.OutputPort(5).Data = decisions;

  % save data to dwork
  block.Dwork(1).Data = state;
  block.Dwork(2).Data = pavg;
  block.Dwork(3).Data = R_cmd;
  block.Dwork(4).Data = L_cmd;
  block.Dwork(5).Data = decisions;
  block.Dwork(6).Data = direction;

%endfunction
```